Doctoral Dissertation
Doctoral Program in Management, Production and Design (37^{th}cycle)

Laser Finishing of Components by Directed Energy Deposition

Experimental Campaigns and Numerical Simulations

By

Giuseppe Vecchi

******

Supervisor(s):
Prof. Eleonora Atzeni, Supervisor
Prof. Alessandro Salmi, Co-Supervisor

Doctoral Examination Committee:
Prof. Panagiotis Stavropoulos, Referee, University of Patras
Prof. Silvio Genna, Referee, Università degli Studi di Roma Tor Vergata
Prof. Paolo Claudio Priarone, Politecnico di Torino
Dr. Alberta Aversa, Politecnico di Torino
Dr. Silvio Defanti, Università degli studi di Modena e Reggio Emilia

Politecnico di Torino
2025

Declaration

I hereby declare that, the contents and organization of this dissertation constitute my own original work and does not compromise in any way the rights of third parties, including those relating to the security of personal data.

Giuseppe Vecchi
2025

* This dissertation is presented in partial fulfillment of the requirements for **Ph.D. degree** in the Graduate School of Politecnico di Torino (ScuDo).

I see now that the circumstances of one's birth are irrelevant. It is what you do with the gift of life that determines who you are.

Acknowledgements

Since all the people I would like to acknowledge are Italian, I am sure everyone will comprehend if this small section is reported in Italian too. Apart from their origin, I do not even have the required mastery of the English language to really express all the shadowing of my thoughts here. Writing about experimental plans, numerical simulations and results cannot be elevated on the same level as depicting one's inner world.

Thus, grazie all'Ingegner Giuseppe Vecchi, al Professor Vincenzo Ressa, alla Professoressa Maria Teresa Vingiano ed alla Maestra Carmela Mastrocola. Avete creato per me, e per tutti noi, una realtà famigliare in cui la conoscenza e l'istruzione hanno sempre ricoperto un ruolo centrale.

Grazie all'Ingegner Raffaele Vecchi ed alla Dottoressa Gabriella Ressa, per avermi cresciuto da privilegiato, tanto sul piano materiale che su quello affettivo. Non ho mai sentito la mancanza di nulla, non ho mai dovuto chiedere nulla. Non tutti hanno, o hanno avuto, una simile fortuna durante la propria vita e non esserne consapevoli sarebbe una colpa gravissima.

Grazie a Valeria, studentessa di ferro che rispetto ogni giorno di più. Tradurre in parole il mio amore per te, e qui non ho neanche la scusante della barriera linguistica dalla mia parte, è per me troppo difficile. Spero tu lo sappia anche nei momenti in cui mi dimentico di ricordartelo.

Grazie a Francesca, per avermi regalato, giorno dopo giorno, la sua compagnia ed il suo tempo. Sei diventata il testimone della mia vita, la persona sotto il cui sguardo tutto prende luogo. Mi piacerebbe dire di essere io il creatore di questa immagine quando purtroppo ho dovuto prenderla in prestito per carenza di inventiva personale.

Abstract

Directed Energy Deposition is an emerging Additive Manufacturing technique, offering the potential to process metallic materials in large working volumes and with high flexibility. Therefore, Directed Energy Deposition is expected to assume a primary role in the repairing industry, restoring critical components to an as-good-as-new condition. However, as with all manufacturing processes, Directed Energy Deposition faces several limitations. Directed Energy Deposition is still characterised by low geometrical accuracy, it usually induces high residual stresses in deposited components, and does not ensure high surface quality; namely it usually results in severe surface roughness and waviness. The present work focuses mainly on the last aspect, as high surface roughness is detrimental for several reasons. It does not only negatively impact the appearance of the component, but it also impacts its corrosion resistance properties, wear resistance properties and fatigue life. Thus, components fabricated by Directed Energy Deposition are usually machined after their deposition, to achieve the required surface quality.

The present thesis examines alternative finishing processes that extend beyond the boundaries of simple multi-axis machining. In particular, Laser Polishing is a thermal finishing process that employs a laser beam to locally remelt the uppermost deposited material layer, redistributing the material under the combined action of gravity and surface tension. Laser Polishing is investigated due the possibility of exploiting the same laser used for deposition also for the finishing phase. The current work explores a single material, the 316L, which is one of the most widespread alloys in Directed Energy Deposition applications. The work is articulated on a first experimental campaign comprising a factor screening campaign, an optimum research phase and a final optimisation campaign. The experimental campaign resulted in significant surface quality improvements, with a reduction in the Ra parameter by a factor of ten and the Wa parameter by a factor of two compared to the as-built values. The Ra values exhibited by samples finished by laser polishing were found to be

similar to those of rough machined samples, which is a promising conclusion that paves the way for future investigations. Subsequently, additional investigations were conducted to assess the collateral effects induced by the Laser Polishing process, namely residual stress measurements and microindentation hardness measurements. It is noteworthy that the residual stress state observed in the samples following the Laser Polishing process did not significantly differ from the residual stress state of as-built components. It can therefore be conjectured that the same stress-relief heat treatments that are required for the as-built samples will also suffice for those that have been finished by Laser Polishing. Additionally, microindentation hardness measurements yielded results that did not significantly differ from the as-built ones. Conversely, microindentation hardness measurements highlighted the dependency of the hardness on the energy employed during Laser Polishing treatments. Finally, a conductive heat transfer numerical model was developed to describe the temperature distribution reached during the Laser Polishing process. The numerical model was then compared with the experimental results obtained using thermocouples, and its accuracy evaluated accordingly. It is worth recalling that the validity of the quantitative results yet described is framed to the single material tested through the investigation, namely the 316L. However, this same methodology could be easily applied to different materials to gradually expand the body of knowledge on the topic.

In conclusion, this investigation provided a holistic description of Laser Polishing applied to components obtained by Directed Energy Deposition. The results obtained thus far indicate the potential for a profitable utilisation of Laser Polishing for the finishing of all non-mating surfaces of a component, and of the mating surfaces where no relative motion is planned.

Future works should concentrate on further improving the quality of the resulting surfaces, introducing different sets of parameters for the initial roughing phase and the subsequent finishing phase, on considering additional collateral effects of laser polishing such as microstructural alterations, and on improving the accuracy of the developed numerical model.

Contents

List of Figures

List of Tables

Nomenclature

Surface quality parameters

l_e	Acquisition length, as per ISO 21920
l_n	Acquisition length, as per ISO 4287
l_r	Sampling length
l_{sc}	Section length
n_{sc}	Number of section length
Ra	Arithmetic mean height
Rku, Wku	Kurtosis of the profile
Rq, Wq	Root mean square height of the profile
Rsk, Wsk	Skewness of the profile
Rz, Wz	Maximum height of the profile

Acronyms

AFM	Abrasive Flow Machining
AM	Additive Manufacturing
AMed	Additively Manufactured
ANOVA	Analysis of Variance
ASTM	American Society for Testing and Materials

CCD	Central Composite Design
CFD	Computational Fluid Mechanics
DED	Directed Energy Deposition
DED-EB	Directed Energy Deposition with Electron Beam
DED-LB	Directed Energy Deposition with Laser Beam
DEDed	Directed Energy Deposited
DMD	Direct Metal Deposition
FDM	Fused Deposition Modelling
ISF	Isotropic Superfinish
ISO	International Organisation for Standardisation
LED	Linear Energy Density
LENS	Laser Engineered Net Shaping
LP	Laser Polishing
LPed	Laser Polished
PBF	Powder Bed Fusion
SAG	Shape Adaptive Grinding
SDGs	Sustainable Development Goals
SLA	Stereolithography
SLS	Selective Laser Sintering
TIG	Tungsten Inert Gas
W-EDM	Wire - Electric Discharge Machining
WAAM	Wire Arc Additive Manufacturing
XRD	X-ray diffraction

Chapter 1

Directed Energy Deposition Background Information

Additive manufacturing (AM) knew a rapid growth across the manufacturing industry over the last decades, from being used only for prototyping purposes to providing market-ready components. Different manufacturing processes fall under the definition of AM. One of the most noteworthy process is Directed Energy Deposition (DED), primarily due to its high flexibility, large building volumes and fast deposition rates. However, a wider use of Directed Energy Deposition is still hindered by unsolved problems, such as low geometrical accuracy and poor surface quality.

1.1 From Rapid Prototyping to Additive Manufacturing

Additive manufacturing is a family of industrial processes characterised by the common feature of building a component layer-by-layer, directly from a 3D computer model, without the need of bespoke tools [1]. The birth of AM might be traced back to the patent proposed by Pierre Ciraud in 1971 [2]. This pioneering work proposed the use of a concentrated heat source to melt a material in the form of a powder, resulting in a usable component. Going even backwards, in 1925 Ralph

Baker patented a method for producing *decorative articles*, as depicted in Figure 1.1, by means of a fusible metallic electrode and a movable welding head [3].

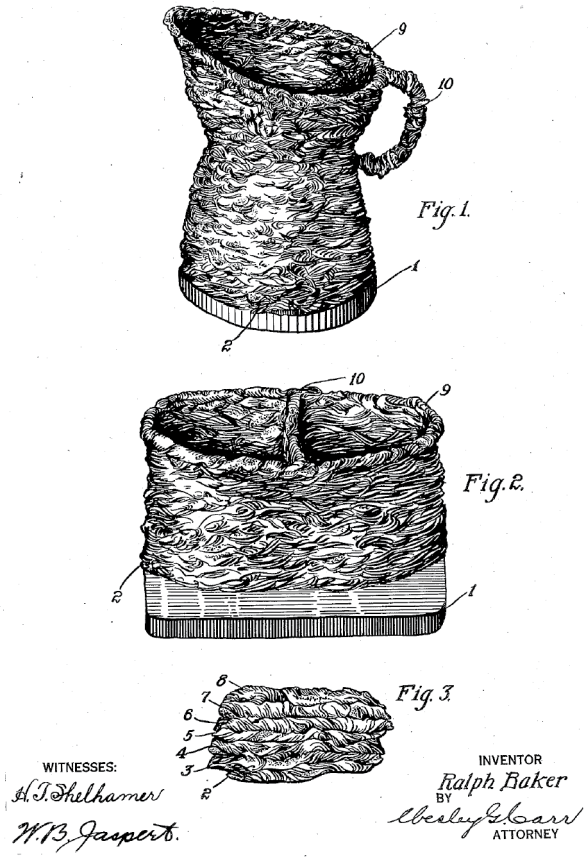

Fig. 1.1 Examples of metallic manufacts produced by Ralph Baker, 1925 [3].

The first commercial AM system entered the market only in 1987, with the first stereolitography (SLA) system by 3D system. In 1991 Stratasys proposed its Fused Deposition Modelling (FDM) technique, reasonably assumed as the most widely known technique to the general public, and a year later Desk Top Manufacturing (DTM) corp proposed the first Selective Laser Sintering (SLS) machine. All these first AM processes, together with many others that did not meet similar fortune on the market, made mostly use of polymeric materials. These embryonic AM systems showed the world the disruptive capabilities intrinsic in AM processes, overcoming many paradigms of the conventional manufacturing world. However, the narrow material availability, together with limited system capacities, constrained the newborn AM systems to the only prototyping activity.

Fast forward, it took ten more years from the introduction of the SLA to find on the market the first examples of metal AM machines, the Laser AM systems by AeroMet in 1997, and the Laser Engineered Net Shaping (LENS) systems by Optomec in 1998, ascribable to the idea of Ciraud. EOS GmbH, already in the market of polymeric SLS machines, presented in 2001 a 20 µm steel powder, essential step for the later growth of all Powder Bed Fusion (PBF) processes. Through the years, thanks to the improvements provided by the early stakeholders of the AM field, companies started to understand the potentialities of AM also outside of the mere prototyping activity. AM systems started to be used for fabrication and repair of tools and moulds, with 8% of the whole AM production intended for end-use products [4]. The last fundamental step has been done in the last decade, with AM systems producing market-ready components on a permanent basis. Most of the historical milestones here reported were taken from the Wohlers report 2016-2022 [5].

1.1.1 Latest Developments on Additive Manufacturing

Lately, universities and companies have kept improving AM processes, expanding the range of possibilities. Machines with relatively large working volume, especially if compared to previous AM ones, have been proposed on the market; increasing the maximum dimensions of additively manufactured components [6]. At the same time, considerable effort has been taken to enlarge the plethora of available materials. Non ferrous materials, such as reflective materials, refractory materials, intermetallic compounds and high entropy alloys have slowly started to enter the AM market [7]. Similarly, the interest in ceramic matrix composites processed by AM has been growing, showing useful applications in the aerospace and biomedical sectors [8]. Multi-material components are also being studied due to the unique properties that arise from the concurrent use of different materials [9].

These fundamental improvements allowed AM process family to keep growing in the relative markets, especially in the aerospace, automotive and biomedical ones. The AM market size in the aerospace sector is expected to reach 8.35 billion dollars in 2029 [10], mainly due to the high performances and lower weights granted by AM components. AM processes can also mitigate the problem of the high demand volatility of spare parts in the aerospace sector, being extremely flexible and able to work with small production volumes [11]. Similarly, the automotive AM market size is estimated around 9 billion dollars in 2029, only considering end-use part

production. Lastly, the AM biomedical market should overcome 6 billion dollars by 2030 [10, 12], pulled by the extreme customisation granted by AM, able to meet the specific needs of each single patient.

The significant AM permeation in several industrial fields forced engineers to question also its role in the modern industrial paradigm [13]. Calignano and Mercurio [14] proposed a conceptual framework on the possible effects of AM on distributed production, reshoring and sustainability. The shift to a more distributed and regionalised production was also studied by Akbari [15], who reasserted AM advantages in low volume production scenarios. Orji and Ojadi [16] proposed a similar investigation on the barriers limiting the implementation of AM in developing African countries, suggesting how supply chain sharing could help to overcome these same barriers.

Overall, it should be clear to the reader that AM technologies have the potential to gain a leading role in specific industrial fields with peculiar needs. However, different AM processes have strongly different characteristics, often being complementary rather than in direct competition.

1.2 Directed Energy Deposition: Introduction and Market Positioning

DED is one of the seven processes AM is conventionally divided into [1], and one of the most promising limiting to metallic materials. DED systems use a focused energy source to locally melt a substrate, resulting in a melt pool. Feedstock materials are delivered inside the melt pool, melting in turn. The energy source and the feedstock delivery system compose the deposition head, core element of any DED machine. The relative motion between deposition head and substrate enables the almost instantaneous solidification of previously melted material, laying the foundations to the growth of the component [17]. This motion can be provided by different solutions, from extremely simple 2.5-axis machines to more than 5-axis machines, even including robotic arms.

Although PBF processes account for the largest share of metal-AM market, DED systems are expect to increase their own share up to the 11% of market revenues in the near future [18]. Deepening some details, DED represents a family of industrial

processes in turn, where each single DED processes is characterised by a singular combination of energy source, either laser beam, electron beam or electric arc, and feedstock material form, either powder or wire. From here, several largely known processes come, such as Wire Arc Additive Manufacturing (WAAM), Direct Metal Deposition (DMD) and LENS among all. In order to ensure a clearer communication between DED stakeholders, ISO and ASTM proposed a join standard nomenclature [1], also followed in the present document. For example, DED-LB/Powder refers to all those DED systems using a laser beam as energy source and powder as feedstock material. The present document mostly investigated DED-LB/Powder systems, as they account for the vast majority of installed systems [19, 20].

DED-LB/Powder systems are characterised by unique features, making them stand out from other AM processes. Firstly, DED-LB/Powder systems, and more in general most DED systems, do not require a closed chamber and can work in open environment, safety issues permitting. Removing the closed chamber constraint, DED-LB/Powder systems can deposit components considerably larger than other AM processes, such as PBF ones. Unique case is the DED-EB configuration, which requires a vacuum chamber due to the use of an electron beam as energy source. Still, also in this case the declared working volumes are in the order of the cubic meter [21]. Secondly, DED-LB/Powder usually deposit material one order of magnitude faster than the PBF counterpart [22]. This is a key feature of DED-LB/Powder systems since it allows a time-efficient deposition of large components, excessively time consuming otherwise. Moreover, DED-LB/Powder systems have proved capable of depositing complex geometries [23], though not on the same complexity level of PBF systems. Lastly, no constraints have been introduced regarding the planarity of the substrate used for deposition. In fact, DED-LB/Powder systems can effectively deposit both on planar and non-planar surfaces, therefore being suitable for depositing additional features on already existing components and for repairing activities.

1.2.1 Directed Energy Deposition and Repairing Applications

Extending the end-of-life of industrial components by repairing and remanufacturing can contribute in reducing the environmental footprint of the manufacturing sector [24]. Remanufacturing has been defined as the industrial process bringing back a component to an "as good as new condition" [25, 26]. Remanufacturing

can be of extreme importance when considering high value components, such as molds or shells; reducing operational costs [27] and environmental impacts [28, 29]. This manufacturing approach is well embedded in the Agenda 2030 established by the United Nations [30], specially relating to the Sustainable Developing Goals (SDGs) of *Industry, Innovation and Infrastructure*, of *Responsible Consumption and Production*, and of *Climate Change*.

Thus, arc welding techniques have been conventionally used for repairing operations of high-end industrial components [31]. Among arc-welding techniques, Tungsten Inert Gas (TIG) welding takes advantage of a tungsten electrode, that does not melt in the right environmental condition, to melt the filler material under an inert shielding atmosphere [32]. Although TIG welding is known to involve the lower heat input among arc-welding techniques [33], the residual life of components repaired by consecutive TIG welding passes does not usually match the residual life of the original component [34]. This behaviour is usually related to the high heat input of the TIG welding technique [34].

DED has been considered as a possible alternative to arc-welding techniques for repairing activities in several published studies. The main features presented in Section 1.2, namely the possibility of depositing on non-planar surfaces, significant working volumes, and deposition rates, perfectly explain the growing interest of the repairing industry in DED systems over the years. DED systems can deposit on large and complex-shaped components, such as molds and shells, thanks to their significant working volumes. Moreover, they have both the technical capabilities and the deposition speed to make the repairing operations costly effective. It has been confirmed that the repairing through DED-LB/Powder implies a lower environmental footprint than producing a component from scratches, especially when dealing with bulk components such as mould's shell [35, 36], in accordance with the SDGs previously presented. Furthermore, Bennett et al. [34] compared the results of the remanufacturing of a worn automotive die by DED-LB/Powder and TIG welding, results showed in Figure 1.2. They reported that the die repaired by DED-LB/Powder showcased a useful life similar to the original one, whereas the TIG repaired one only lasted for around 20% of the original length, helping to reduce the estimated environmental footprint. The mechanical behaviour of samples repaired by DED-LB/Powder have been investigated too. Rauch, Hascoët, and Mallaiah [37] demonstrated that yield strength and ultimate tensile strength (UTS) of repaired Ti6Al4V components were comparable to wrought alloy ones. On the other hand,

residual elongation was severely lower, up to 75%, than the wrought alloy one. Oh et al. [38] conducted conceptually similar trials on 316L stainless steel samples, repairing notches of variable depth by DED-LB/Powder. They measured lower mechanical strengths and elongations for deeper notched samples, and explained this behaviour with a higher pore concentration at the interface between deposited material and substrate. In a follow-up study, they managed to solve the problem by pre-heating the substrate with a heating table, thereby reducing porosity at material interface [39].

Fig. 1.2 Worn automotive die before and after the repair by DED-LB/Powder [34].

In conclusion, DED-LB/Powder meets all the requirements to be profitably used in the repair and remanufacturing field. That being said, a broader industrial usage of DED-LB/Powder is still hindered by several process restrictions, presented to the reader in Section 1.2.2.

1.2.2 Directed Energy Deposition Weaknesses

DED-LB/Powder is still a relatively new industrial process, especially if compared to casting, forging or machining processes, being on the market roughly for twenty year. As every new industrial process, DED-LB/Powder has to give answer to several open questions related to its real capabilities. DED-LB/Powder systems usually show modest geometrical accuracy, induce considerable residual stresses in deposited components, and do not ensure a satisfying surface quality.

The limited geometrical accuracy of DED-LB/Powder systems has been largely investigated in the recent years [40, 41], stating its equivalence to casting and a minor accuracy than PBF ones [42]. In order to improve the accuracy of deposited geometries, active process control methods have been fruitfully implemented to adjust process parameters in real time, and ensure a stable shape of the melt pool throughout the deposition [43, 44]. Moreover, the large thermal gradients that characterise DED-LB/Powder process usually induce consistent residual stresses in deposited components [45, 46], dramatically detrimental for both their static and dynamic performances. Fine tuning of process parameters [47] and scanning strategy [48] have been proved efficient in mitigating residual stresses. Finally, the poor surface quality of DED-LB/Powder components is well known, usually leading to Ra values between 25 and 35 µm [42]. The adverse role of high surface roughness on tribological, corrosion resistance and fatigue properties of a component are now largely established [49]. Focusing on the only effect of surface roughness on fatigue life, it abruptly decreases the life span of a component under a dynamic load [50, 51, 52]. Roughness reduction of DEDed components by process parameters optimisation has lead to minimal improvements [48, 47], as well as substrate preheating during deposition [53] or deposition strategies optimisation [54]. It is worth highlighting that the process windows granting a better surface roughness might not superimpose with the process windows required for an optimal depositions, i.e. correct layer growth, target accuracy and full densification. Supposing the two process windows do not suggest a common set of process parameters, priority must be given to the process itself, leaving surface finishing to later production stages.

Therefore, it is straightforward to understand how post-deposition surface finishing processes are mandatory to ensure the desired mechanical properties to DEDed components.

1.2.3 Brief Insights on Directed Energy Deposition Finishing Processes

In this section, a brief overview on surface finishing processes for DEDed components is presented. This subsection is meant to allow the reader understand the scope of the present thesis work, and therefore directly move to Chapter 3 where the actual investigation begins. However, a more in-depth literature review of surface finishing techniques of DEDed components is provided in Chapter 2.

The most common approach for finishing DEDed components, and more in general all AMed components, is to machine them by meas of multi-axis milling machines. Multi-axis milling operations have already been largely studied and applied on conventionally manufactured materials to obtain complex shaped manufacts. The experience matured in the conventional manufacturing field was then carried to the AM one, without meeting the same results quality. In fact, machining of DEDed components has been proved difficult without considering their unique features. The rapid cooling mechanisms, inherent in DED-LB/Powder processes, create a very fine microstructure, making components harder than conventional ones. The higher hardness of DEDed components usually causes a faster wear of the mill tool and requires higher power for the machining operations. Moreover, complex geometries deposited by DED-LB/Powder can create areas difficult to reach by a milling machine, whose encumbrance cannot be overlooked. Finally, the need of subsequent milling operations can prompt alignment errors, due to the necessity to move the component from its original position into a new reference system.

Apart from machining operations, another possible solution to improve the surface quality of DEDed components is opting for thermal finishing processes. In thermal finishing processes, a focalized energy source is used to melt the surface of the components and to improve its topography. Out of the available thermal sources, lasers surely represent the most promising option. Laser finishing operations, such as laser machining and laser polishing, have been widely applied in conventional manufacturing scenarios, seeming well suited for DED-LB/Powder components too. Laser treatments do not involve any physical tool, avoiding the problem of tool wear in its entirety, do not require lubricants, and sensibly reduce the accessibility issues to the target area. Moreover, DED-LB/Powder systems already come with a laser source, theoretically allowing the use of the same laser source for both deposition and finishing phases.

1.3 Laser Polishing and Research Questions

Although laser polishing has been showing promising results in previously published articles, a comprehensive experimental campaign is still lacking in literature. Starting from a robust identification of active process parameters, by means of a factor screening analysis, and moving closer to a response optimum using even a simple gradient method. Additionally, in the greatest part of the presented literature, only Ra has been considered to express the quality of the surface obtained after the laser treatment, preventing a more holistic description of finished surfaces by means of other profile parameters. In a second moment, to the author's knowledge no empirical model have been proposed to predict the roughness resulting from laser polishing treatments. A similar model would be extremely helpful when performing real finishing operations, having the potential of saving both time and resources. Moreover, there is no clear statement about the possibility of using the same process parameters, thus the same model, for finishing top and lateral surface of DEDed components. Although these two type of surfaces are closer in DED than in other AM processes, they still have different deposition histories and topographies. Thus, the possibility of neglecting these differences and using the same model to describe both of them is still an open question. Going further, it is common knowledge that laser polishing processes inevitably imply undesired alterations of the substrate, also in its unmelted region. Depth of remelting, microstructural modifications and related microindentation hardness modifications have already been presented in previous works. On the other hand, no results have been proposed concerning the residual stresses induced, or relieved, by laser polishing treatment; leaving the door open for future investigations. Finally, previous investigations always limited their attention to either bulk or thin-walled components. In general, these two classes of components have strongly different heat capacities, and therefore respond differently to laser polishing treatments. As the heat distribution inside the components can influence the results of the laser polishing treatments, a numerical model might be helpful to simulate the same laser polishing operations, providing a deeper understanding of the temperature distribution.

Willing to summarise and formalise the gaps just highlighted, the main objectives of the present thesis are hereby stated:

RQ1: Can a comprehensive experimental campaign lead to a robust empirical model predicting the resulting surface roughness of future laser polishing treatments?

RQ2: Are the collateral effects of laser polishing treatments acceptable? Could laser polishing lead to unexpected improvements of material characteristics?

RQ3: Can a numerical model help the understanding of the temperature distribution inside the sample during laser polishing treatments?

RQ4: What is the real industrial potential of Laser Polishing? In which context could Laser Polishing be profitably used?

In order to cover the aforementioned research gaps, the present investigation was organised in several consecutive stages. Initially, an experimental campaign was carried out to identify an optimal set of process parameters, with the objective of ensuring a high surface quality of the 316L substrates that had been previously deposited. Together with the definition of the optimal set of process parameters, an empirical model was defined to predict future values of Ra and Wa within the investigated domain. Subsequently, the focus was brought upon the collateral effects induced by laser polishing on the 316L substrates. In particular, residual stresses and microindentation hardness variations were measured and correlated with the energy used during the LP treatment. Finally, a FE model was implemented in Abaqus, providing the backbone for a more comprehensive numerical model that is still under development. In conclusion, the investigation was able to define a framework for the use of Laser Polishing in surface treatments of 316L components. Laser Polishing treatments were deemed adequate for polishing free surfaces, and mating surfaces where relative displacement is not considered. Overall, Laser Polishing could have a meaningful impact on the post processing of components deposited by Directed Energy Deposition

Chapter 2

Surface Finishing of Components Deposited by Directed Energy Deposition

The use of DED-LB/Powder in the manufacturing environment has been steadily growing over the last years, finding perfect application in repairing activities. However, its widespread application has been hindered by several process drawbacks, such as limited geometrical accuracy, large residual deformations, and poor surface quality. It is important to notice that the poor surface quality resulting by DED-LB/Powder systems drastically reduces corrosion resistance properties, worsen tribological properties, and has a negative impact on the fatigue life of the DEDed components. Thus, since a poor surface quality has that many negative impacts on the performances of DEDed components, the present section collected an extensive literature review on finishing solutions aimed at improving the surface quality of the same DEDed components. Section 2.1 introduces standard coefficients to ensure a holistic description of the quality of the surface under investigation, not limiting the discussion to a single feature. Subsequently, in Section 2.2 a distinction is proposed between functional and aesthetic surfaces, highlighting the different requirements of the two categories. Therefore, mechanical, chemical and thermal finishing processes are listed in Section 2.3, Section 2.4 and Section 2.5 respectively, and the main academic contributions discussed. Some of the works reported in these Sections

were not directly related to the DED-LB/Powder process, but to PBF processes instead. The studies in question were still considered worth mentioning since the methodology applied, and the results obtained, could be transferred to DEDed components in the near future. Lastly, Section 2.5 provides a detailed analysis of laser finishing processes to enhance the knowledge on the current state of the art of the topic, and to suggests constructive proposals.

2.1 Surface Topography and Texture

The claim of a poor surface quality of DEDed components has already been largely discussed in Section 1.2.2 and Section 1.2.3. Surface quality can be expressed both in terms of profile parameters, typically expressed as roughness parameters (*R*-parameters) and waviness parameters (*W*-parameters), and areal parameters (*S*-parameters). Profile parameters have a considerably longer history in the manufacturing context than areal ones, easily justified by the higher simplicity and cost-effectiveness of the related measuring systems. Accordingly, in the manufacturing industry surface quality is commonly associated to profile parameters, whether in casting [55], AM [56], water cutting [57], grinding [58] or quality control applications [59]. Roughness parameters do not provide a comprehensive description of the studied surface on their own. Therefore, waviness parameters should be also included in the discussion. This section discusses the most significant roughness and waviness profile parameters according to the current ISO 21920 standard [60], to provide a comprehensive description of the studied surface.

2.1.1 Preliminary Definitions

Roughness testers represent the market standard for roughness profile acquisitions. Roughness testers use a probe, mounted on a movable stylus, to gauge the surface under analysis. The first operation that any roughness tester has to accomplish is the definition of a mechanical profile from the actual probed surface. The mechanical profile is an approximation of the real profile of the surface, created by the relative motion of the roughness tester probe on the surface of the component, as perfectly depicted in Figure 2.1. The ISO 21920 standard requires the profile to be acquired along the direction of maximum attended roughness, favouring a more conservative

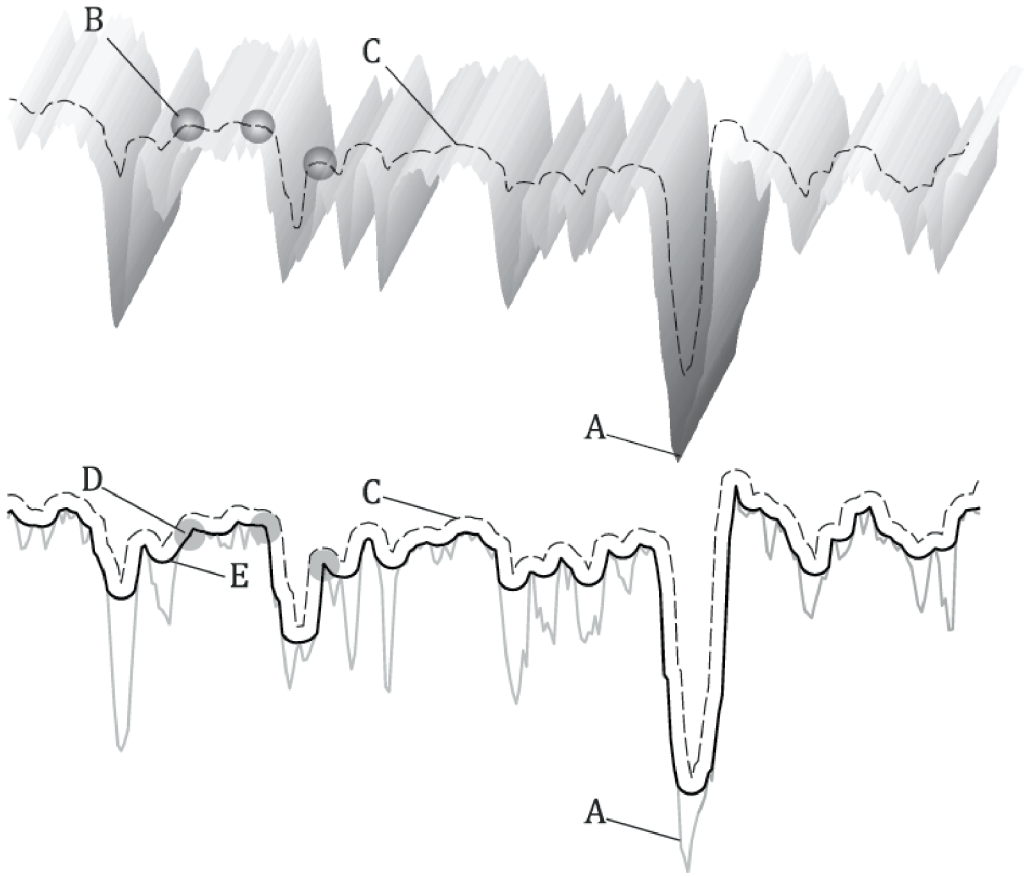

Fig. 2.1 Mechanical Profile. A) skin model; B) ideal tactile sphere of radius r; C) envelope curve of the planar locus of the centre of an ideal tactile sphere rolled over the skin model; D) circular disc of radius r; E) mechanical profile: boundary of the mathematical erosion, by the circular disc D, of the envelope curve C [60].

approach. ISO 21920 does not provide any distinction between periodic and non-periodic profiles, which represents a strong distinction to the previous ISO 4287 standard [61]. Moreover, profiles should be acquired considering surface defects and imperfections as integral part of the surface under investigation, another important perspective change of ISO 21920 compared to ISO 4287. Once the mechanical profile has been acquired, two types of filters are applied on it to derive the roughness and waviness profiles. A profile S-filter, i.e. a high-pass filter, removes small lateral scale components from the mechanical profile, deriving the primary surface profile from it. The small scale components removed at this stage are merely related to measuring errors. Subsequently, a profile F-operation removes the form component from the primary surface profile, i.e. the very large wavelength components, providing the primary profile, P-profile, which can already be used for global considerations on

surface quality. For instance, the form component removed from the primary surface profile may be related to the non-planarity of the real considered surface. From the P-profile, two more filtering operations are needed to derive the R-profile and W-profile. An L-filter, i.e. low-pass filter, removes the large-scale lateral components from the P-profile establishing the R-profile. On the other hand, a second S-filter applied to the P-profile establishes the W-profile. Figure 2.2 intuitively explains the whole chain of filtering operations, leading to the definition of the R and W-profiles.

The evaluation length is defined on the extract profiles and it is used to identify section length parameters, also called field parameters. In the current standard the evaluation length was renamed l_e, whereas it was referred to as l_n in the ISO 4287 standard. l_e is usually smaller than the transverse length, which is the length of the overall excursion of roughness tester probe over the surface. This feature must be considered when measuring a sample, to ensure the roughness tester the presence of the actual required length for acquisition. l_e is divided into n_{sc} smaller segments, namely the section lengths, l_{sc}, used for computing section length parameters. As for l_e, l_{sc} were referred to as sampling lengths l_r in ISO 4287.

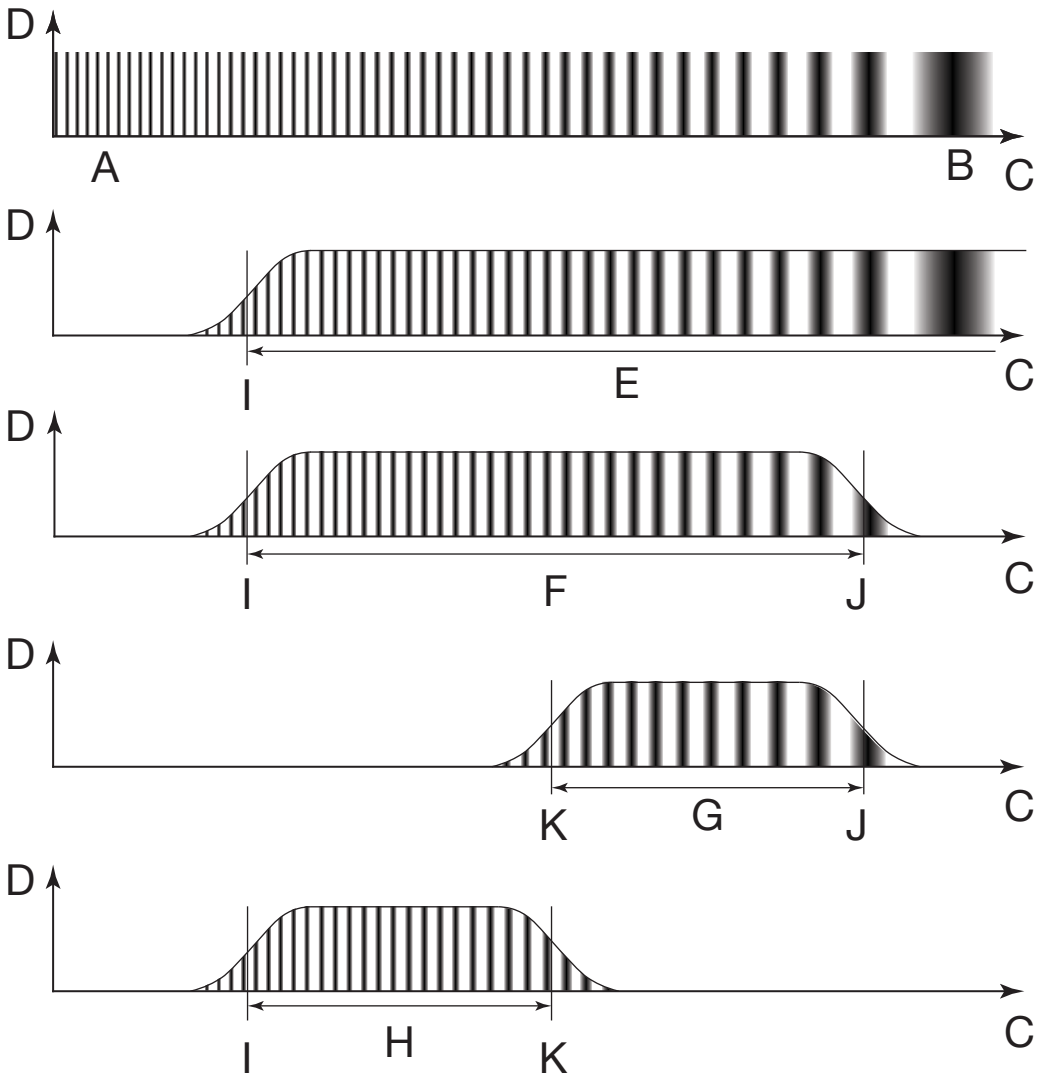

Fig. 2.2 Relationship between the primary surface profile, P-profile, W-profile and R-profile; A) small lateral scale; B) large lateral scale; C) scale axis; D) amplitude axis; E) lateral scale component of primary surface profile; F) lateral scale component of P-profile; G) lateral scale component of W-profile; H) lateral scale component of R-profile; I) profile S-filter; J) profile F-operation; K) profile L-filter [60].

2.1.2 Ra, Wa - Arithmetic Mean Height

Ra is by far the most known and used parameter related to surface quality assessments. In the ISO 21920 Ra is defined as: "*the arithmetic mean of the absolute values of the ordinate values*" [60]. Ra is computed as outlined in Equation 2.1.

$$R_a = \frac{1}{l_e} \int_0^{l_e} |z(x)| dx \tag{2.1}$$

The widespread acceptance of Ra as the most significant surface quality parameter is mainly related to its conciseness. Although Ra can be used to synthetically express the quality of a surface, its indication alone might not be sufficient to comprehensively describe it. For example, two easily distinguishable profiles, as the ones shown in Figure 2.3, might be characterised by similar Ra values while having completely different trends. As Ra is computed on the R-profile, Wa is computed on the W-profile following the same rationale.

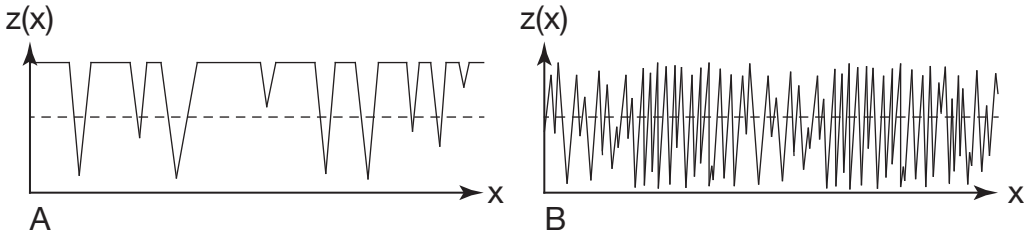

Fig. 2.3 Examples of two different profiles featured by a similar Ra value: A) plateau like profile; B) highly irregular profile.

2.1.3 Rz, Wz - Maximum Height

In the ISO 21920 Rz is defined as "*the mean value, from all section lengths, of the per section sum of the largest peak height and the largest pit depth*" [60]. Rz is computed according to Equation 2.2, where $Z_{ph,j}$ is the height of profile in the i-th section length and $Z_{vd,k}$ is the depth of the profile in the same i-th section length. Therefore, Rz is more pertaining to the presence of large peaks and valleys in the section lengths, than to the average value of the profile quota, as shown in Figure 2.4 for the case where $n_{sc} = 5$.

$$R_z = \frac{1}{n_{sc}} \sum_{i=1}^{n_{sc}} \left(\underset{j \in N_{p,i}}{max} (Z_{ph,j}) + \underset{k \in N_{v,i}}{max} (Z_{vd,k}) \right) \tag{2.2}$$

Roughness testers referring to outdated versions of the standard might compute Rz as the "ten point height of irregularities", leading to slightly different results

compared to more updated instrumentation. This aspect should always be considered when comparing results computed through different instruments.

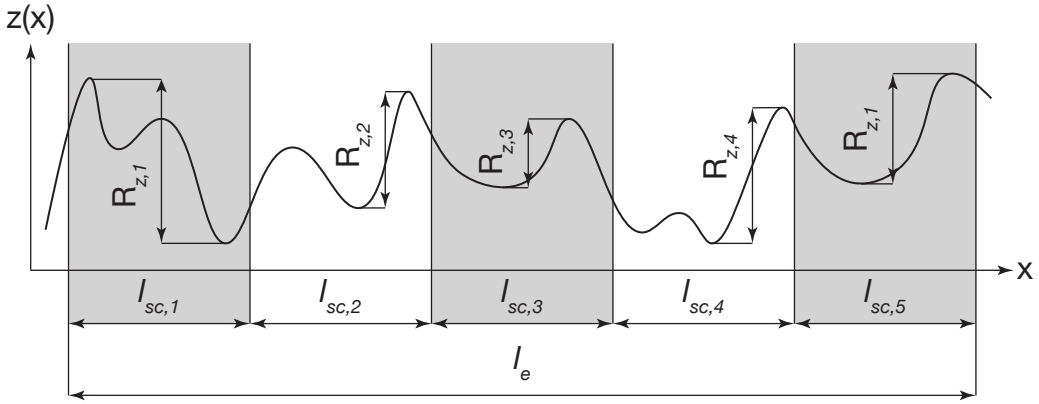

Fig. 2.4 Graphical representation of Rz meaning.

2.1.4 Rsk, Wsk - Skewness

Apart from intuitive parameters, such as Ra and Rz, other less intuitive parameters can be extremely useful to describe the features of a profile. Rsk is the skewness parameter and is defined as "*the quotient of the mean cube value of the ordinate values and the cube of Rq*" [60]. Where Rq is the root mean square height of the profile. The calculation of Rsk is performed using Equation 2.3. Rsk measures the symmetry of the probability density function of the ordinate values of the profile about its mean line, as per Figure 2.5.

$$R_{sk} = \frac{1}{R_q^3}\frac{1}{l_e}\int_0^{l_e} z^3(x)dx \tag{2.3}$$

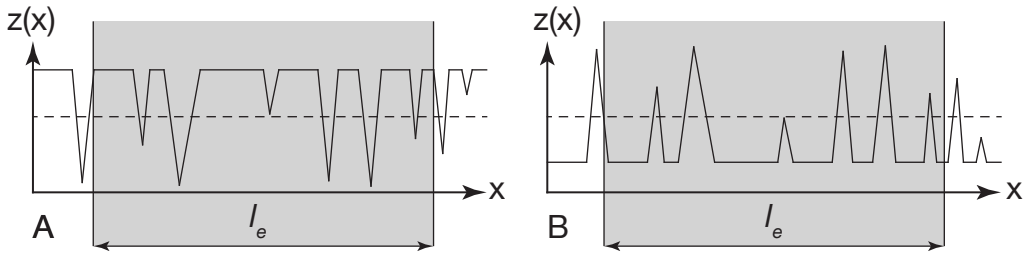

Fig. 2.5 Graphical representation of Rsk meaning. Negative Rsk on left, and Positive Rsk on the right.

Negative Rsk value suggests a positive shift of the profile about its mean value, i.e. a plateau-like profile with deep groves, whereas a positive Rsk value suggests a negative shift of the profile, i.e. a plateau-like profile with high peaks. Rsk is strongly influenced by isolated peaks and valleys, being a third function of profile ordinates. However, the analysis of the Rsk coefficient can point out unique profile characteristics, and ease a better understanding of surface tribological properties.

2.1.5 Rku, Wku - Kurtosis

The Kurtosis parameter Rku is defined as "*the quotient of the mean quartic value of the ordinate values and the fourth power of Rq*" [60], and it is computed using Equation 2.4.

$$R_{sk} = \frac{1}{R_q^4}\frac{1}{l_e}\int_0^{l_e} z^4(x)dx \tag{2.4}$$

Rku measures the "sharpness" of the probability density function representing the ordinate values of the profile. A value lower than 3 is typical of so-called Platykurtic distributions, characterised by lower mean occurrences and higher tails. Conversely, an Rku value above 3 describes a Leptokurtic distribution with a narrower occurrences distributions. Thus, roughness profiles with an Rku lower than 3 usually show gradual and uniform changes of slope. On the other hand, roughness profiles with an Rku far above 3 have most of the profile near the mean line, with few sharp protrusions in both directions, as in Figure 2.6. The use of the fourth power in the formulation of Rku does not allow to distinguish between sharp peaks and valley, as only their absolute value is considered. Moreover, Rku is sensible to the presence of isolated peaks and valleys, as for Rsk.

2.2 Requirements for Functional and Aesthetic Surfaces in the Manufacturing Industry

The present section discussed the most useful parameters to include in a dissertation according to the actual function of the described surface. Different profile parameters tend to describe different features of the reference surface, as outline in Section 2.1.

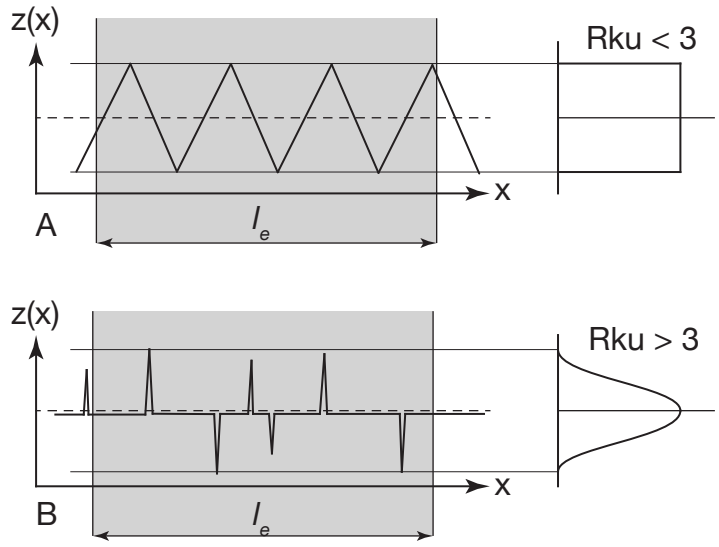

Fig. 2.6 Graphical representation of the meaning of the Rku coefficient for two limit cases.

Therefore, the operator should pay more attention to a single parameter, or parameter set, than to another according to the area of interest [62]. Figure 2.7 shows a table from ISO 12085 [63], relating the function of the surface to the most meaningful parameters. The measurement of R-profile parameters is required for almost all surface designations reported, even for aesthetic ones [64]. W-profile parameters are often required for parts in contact, and rarely for independent surfaces. Moreover, the requirement on surface waviness are extremely strict for surfaces in contact with relative displacements, as for rolling, and more relaxed for surfaces in contact without displacement, as for static sealing.

These specifications should be carefully considered when selecting the R and W profile parameters to be measured prior to a surface quality assessment in order not to overlook important surface characteristics that can greatly affect the performance of the component. Similarly, the same table should also be consulted after the surface quality assessment to certify the suitability of the surface for the desired application.

Surface		Functions applied to the surface		Parameters								
				Roughness profile			Waviness profile				Primary profile	
		Designations	Symbol[a]	*R*	*Rx*	*AR*	*W*	*Wx*	*Wte*	*AW*	*Pt*	*Pδc*
two parts in contact	with relative displacement	Slipping (lubricated)	FG	●			⩽ 0,8*R*			○		●
		Dry friction	FS	●		○		●		○		
		Rolling	FR	●			⩽ 0,3*R*	●		○		○
		Resistance to hammering	RM	○		○	○			○		●
		Fluid friction	FF	●		○				○		
		Dynamic sealing with gasket	ED	●	○	○	⩽ 0,6*R*	●		○		
		Dynamic sealing without gasket	ED	○	●		⩽ 0,6*R*					●
	without displacement	Static sealing with gasket	ES	○	●		⩽ *R*		○	○		
		Static sealing without gasket	ES	○	●		⩽ *R*		●			
		Adjustment without displacement with stress	AC	○								●
		Adherence (bonding)	AD	●							○	
Independent surface	with stress	Tools (cutting surface)	OC	○		○	●			●		
		Fatigue strengths	EA	○	●	○						○
	without stress	Corrosion resistance	RC	●	●							
		Paint coating	RE			○				○		
		Electrolytic coating	DE	●	⩽ 2*R*	●						
		Measures	ME	●			⩽ *R*					
		Appearance (aspect)	AS	●		○	○			○		

●Most important parameters: specify at least one of them.
○ Secondary parameters: to be specified if necessary according to the part functions.
The indication ⩽ 0,8*R*, for example, means that, if the symbol FG is indicated on the drawing, and *W* not otherwise specified, the upper tolerance on *W* is equal to the upper tolerance on *R* multiplied by 0,8.

[a] The symbols (FG, etc.) are acronyms of French designations.

Fig. 2.7 Motif parameters that can be specified according to the function of surfaces [63].

2.3 Mechanical Finishing of Components by Directed Energy Deposition

Mechanical finishing processes are a set of surface finishing techniques that use mechanical energy to transform the surface of a component. These processes can either remove the outermost layer of a component, or induce a local plastic deformation. Limiting to material removal processes, mechanical surface finishing processes can be further classified according to the tool used to remove the outermost material layer. The simplest classification that can be made is between processes that employ tools with defined geometries, such as milling or turning, and those using tools without defined geometries, such as grinding, mass finishing and abrasive finishing. Milling and turning are able to finishing components in limited time periods, concurrently

achieving excellent surface quality. Moreover, multi-axis CNC machining enables the processing of complex geometries, not being limited to axial-symmetric shapes. However, multi-axis CNC machining cannot usually handle the most intricate geometries resulting from AM processes, such as lattice structures or organic features, due to the encumbrance of the tool itself. Mass finishing, abrasive finishing and grinding are usually used to either reach superior surface finishing, and therefore applied after a previous CNC machining phase, or when the geometrical complexity of the surface is outside the capabilities of multi-axis CNC machining.

2.3.1 CNC Machining of Directed Energy Deposited Components

Machining processes have been used in the manufacturing industry for centuries, reaching a satisfying level of maturity [65]. Today, multi-axis CNC machining represents the industrial standard for finishing DEDed components, and more in general for AM ones. Additional care must be taken during the design phase of a component if a CNC machining finishing step is planned. The surfaces of the component to be finished must be addressed according to their functional requirements, as outline in Section 2.2, and allowances must be included in the original design to compensate for the material loss during machining. The determination of the optimal amount of material allowance is still an open question in DED components. Fuchs et al. [66] investigated the influence of the allowance during peripheral milling of DED-Arc/Wire parts. They suggested that an allowance thickness equal to 125% of the roughness maximum peak should lead to optimal surface finishing and waste material minimisation. Although other works have proposed valuable allowances quantification in other metal AM processes [67, 68], no conclusive results have yet being presented in the DED industry. Moreover, other than allowances, additional features might be included in the original design to facilitate the fixing of the component during the machining phase [69]. When additional fixtures cannot be added to the model, such as during repair operations, specific fixtures must be designed for the case, with a non-negligible influence on the final cost of the finishing operation.

The implementation of allowances and fixtures is a common aspect between DED components and conventionally manufactured ones. The main differences arise during the machining phase itself due to the different machinability of the materials. In fact, the same alloy processed by DED and other conventional manufacturing processes usually exhibits different microstructures. DED is characterised by faster

cooling rates, in the order of 10^2 to 10^5 K s^{-1} [70, 71], large thermal gradients and cyclic heat loads, which generate a unique microstructure in the deposited material, as shown in Figure 2.8. In particular, the grain refinement, due to the high DED cooling rates, was proven capable of enhancing the mechanical properties of the material, such as hardness and tensile strength [72]. Therefore, the machining of DEDed materials usually requires higher cutting force, induces a faster tool wear and can lead to worse results than the machining of conventionally manufactured materials [73]. A consistent scientific production has investigated how to optimise CNC machining process parameters to reduce the aforementioned problems; part of which was reported in the following paragraph.

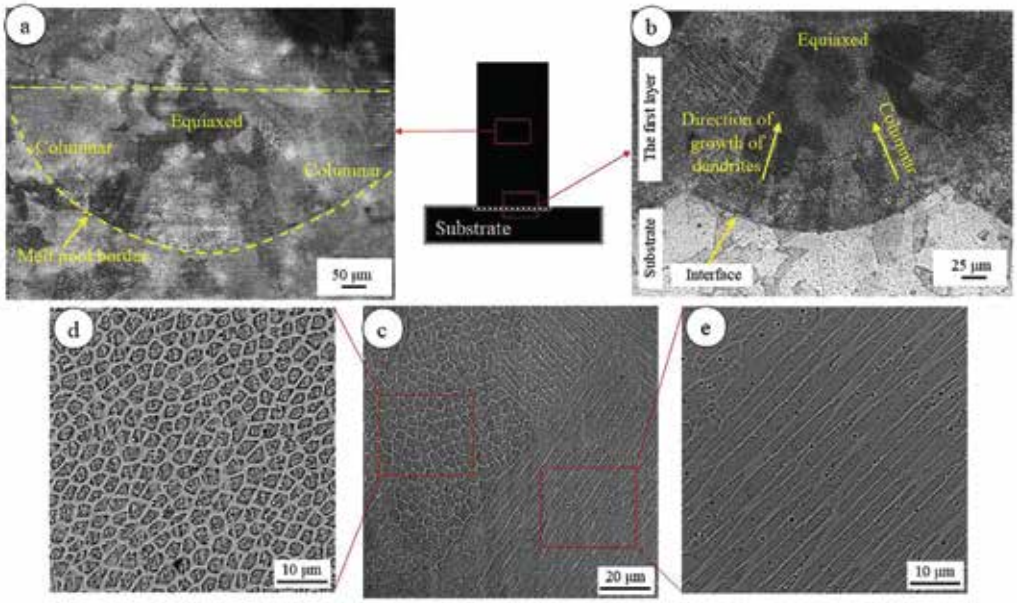

Fig. 2.8 Light optical microscopy micrographs of the DED AISI 216L steel samples produced using fresh powder: (a) a representative melt pool at the middle height, (b) the microstructure of the first layer, (c) SEM images of the columnar and equiaxed microstructures referring to the last deposited layer, (d-e) high magnifications of (c) from different regions [72].

Bai, Chaudhari, and Wang [73] machined ASTM 131 steel samples deposited by DED-LB/Powder and lowered their Ra below the 1 µm threshold. High cutting speeds led to the best surface quality, but at the cost of higher cutting forces, tool wear and continuous chip formation. Lopes et al. [74] milled samples of ER110S-G steel processed by DED-Arc/Wire. Similarly to Bai, Chaudhari, and Wang, they observed lower Ra for higher cutting speed, and a tool wear higher than usual. Kallel et al. [75] deposited Ti6Al4V samples by DED-LB/Powder and machined them reaching Ra

equal to 0.5 µm. Once more, lower feeding rates led to lower Ra, in agreement with Bai, Chaudhari, and Wang. Moreover, high cutting forces, tool wear and compressive residual stresses were registered during the experimentation. The same conclusions were also confirmed by Greco et al. [76] on a micro-scale. They used a 100 µm tool to mill AISI 316L samples deposited by DED-LB/Powder and compared the results with a comparative casted sample. Different tool wear mechanisms were detected, and higher cutting forces measured, stressing once more the necessity of considering the differences between conventionally and AMed materials. Against this background, the necessity of a meticulous process parameter tuning, specific for DEDed samples, is made clear.

As already mentioned, tool accessibility to the finishing area can represent a problem for complex shaped components. Thus, hybrid systems are growing in popularity due to the possibility of alternating deposition and CNC milling steps. However, more challenging process planning and longer production times are hindering a widespread adoption of hybrid systems to date. Moreover, the lubricant used during the machining phase may interfere with powder recycling and further depositions. New approaches must be studied to either remove the need of lubricant, as in dry machining [77], or the use of different ones, as liquid nitrogen in cryogenic milling applications [78].

2.3.2 Finishing of Directed Energy Deposited Components by Abrasives

CNC machining was proven suitable for finishing of DEDed components up to a good surface quality, with Ra generally lower than 1 µm. However, numerous industrial applications deal with tighter surface quality constraints, requiring mirror-like surfaces. Therefore, additional finishing processes are commonly used to reach the required roughness threshold after the first machining operation. In terms of mechanical surface finishing, the most used techniques are grinding, mass finishing, and abrasive finishing.

Grinding is a finishing process enabling extremely low surface roughness. Conventional grinding techniques use abrasive particles of various nature hold in position by a rigid matrix. The use of conventional grinding technologies in the AM industry has been severely impaired by the inability of reworking complex surfaces. Shape

Adaptive Grinding (SAG) was proposed as a flexible grinding system to polish even surfaces of average complexity [79, 80]. SAG uses a compliant elastic tool, covered by nickel-bonded or resin-bonded diamond pellets, to finish complex-shaped surfaces up to Ra lower than 0.1 µm, as schematically shown in Figure 2.9. Although no examples of direct SAG applications to DEDed components are available, this technology surely has the intrinsic potential to be used profitably also on DEDed components.

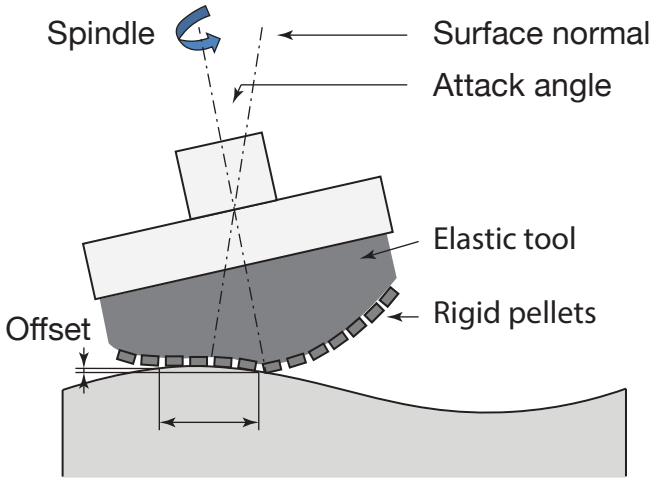

Fig. 2.9 Principles of shape adaptive grinding [79].

Another step forward to finish complex shaped components is represented by mass finishing processes, such as barrel finishing or vibro-finishing. In mass finishing applications the component is put in relative motion with the abrasive media, usually made of ceramic materials. The continuous friction between the component and the abrasive media improves its surface quality. Vibro-finishing has shown promising results on PBF-LB parts, as in the work by Atzeni et al. [81] who used it to finish IN625 samples. Sa was drastically reduced from 44 to 4 µm, but at the cost of more than 60 h to complete. Moreover, the erosion of the edges of the samples also led to a decreased geometrical accuracy of the finished component. The addition of a chemical reactant can enhance the efficiency of the vibro finishing process, as per the Isotropic Superfinish (ISF®) by REM Surface Engineering. Prochaska and Hildreth [82] and Atzeni et al. [83] both achieved excellent results after applying ISF® to PBF components.

Abrasive chips are helpful for finishing complex shaped components, but are still limited by the minimum feature they can reach and by the smaller channel they can

enter. An abrasive slurry is obtained by decreasing the size of the abrasive media indefinitely, becoming extremely useful for finishing even small crevices and internal channels. Abrasive Flow Machining (AFM) uses abrasive slurries of various nature to finish the material surface trough friction. Usually, the component is fixed in position and the slurry is stirred on it surfaces. AFM has gained broad popularity due to its ability to finish internal channel, difficult to reach otherwise. Han et al. [84] finished a maraging steel 300 component processed by PBF-LB, improving the surface quality of internal channels, Sa decreased from 7.7 to 1.8 µm. Guo et al. [85] finished an IN718 component processed by PBF-LB and obtained excellent surface quality of its internal channels, with Ra passing from 10 to 1 µm, suggesting a surface finishing comparable to the one achievable by machining operations. More complex and articulated finishing processes can even be obtained by coupling the abrasive slurry with ultrasonic vibrations [86], cavitation [87], and magnetic materials [88].

Most of the already published examples on abrasive finishing refer to PBF, either PBF-LB or PBF-EB, with little attention to the DED process family. This discrepancy is far from being casual and can be easily explained. Although DED market is rapidly growing, PBF processes still account for the vast majority of the metallic AM market to date, as outlined in Section 1.2. Therefore, it is common sense to invest more resource on exploring finishing solutions for PBF rather than for DED. Moreover, PBF components usually involve higher complexity levels, making almost mandatory the need for non-conventional abrasive finishing. However, the author is confident that the technological improvements in DED process, as the manufacturing of conformal channels by DED [89, 90], will lead to new studies on the suitability of abrasive finishing also on DEDed components.

2.4 Chemical Finishing of Components by Directed Energy Deposition

Chemical finishing processes use chemical reactions to modify the surface of the material in exam. Chemical finishing treatments are well suited for AM components since they can easily reach any point of the surface, with no limitations caused by internal features or thin walls [91, 92]. Moreover, no contact tools are involved and no residual stresses are induced in the part [93]. Scherillo [94] used a mixture of

HNO_3 and HF to finish the outer surface of an AlSi10Mg component manufactured by PBF-LB, resulting in a final Sa value equal to 10 µm. Tyagi et al. [95] finished an AISI 316L component processed by PBF-LB, particularly focusing on its internal channels. They compared chemical and electrochemical finishing, observing a higher flexibility of the former. However, chemical finishing might result in a material removal rate difficult to control, might lead to preferential distribution of specific phases over others, and require specific acidic mixtures for each applications [91].

Electrochemical polishing employs anodic reactions to oxidise the surface of a metallic component and dissolve it into electrolytes by means of electric current [93]. The electrolytes used can be either acidic, highly efficient but hazardous at the same time, or saline. Baicheng et al. [96] finished IN718 samples obtained by PBF-LB in a mixture of sulphuric acid and methanol. The managed to half Ra of the samples, from 6 µm to around 3 µm. Zhao, Qu, and Tang [97] electrochemical polished the internal channel surfaces of an AISI 304 component by PBF-LB in salt bath. The use of a flexible electrode, as shown in Figure 2.10, allowed the finishing of curved channels, perfect examples of the conformal cooling channels typical of AMed components.

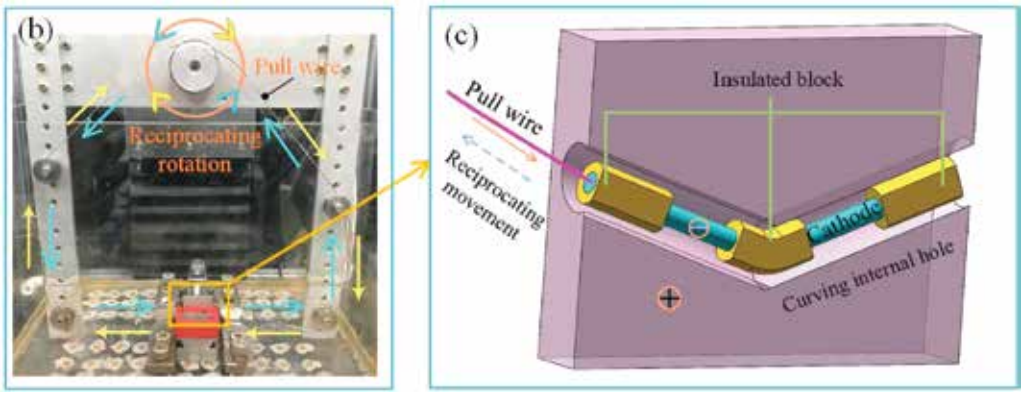

Fig. 2.10 Experimental setup for machining AM curving internal hole: (B) photo of the experimental apparatus; (C) schematic illustration of ECM for AM curving internal hole [97].

In conclusion, both chemical and electrochemical finishing processes could have a meaningful impact on surface roughness reduction of DEDed components. Both processes seem suitable for finishing outer complex-shaped surfaces, whereas some differences appear evident in terms of internal ones. The efficiency of electrochemical finishing is strongly influenced by the relative position between surface and

cathode, hindering its applicability in the case of very complex conformal channels. Conversely, chemical finishing does not have any limitations in that sense, being able to finishing any surface the liquid solution can reach.

2.5 Thermal Finishing of Components by Directed Energy Deposition

Lastly, thermal finishing processes use thermal energy to remelt the outermost layer of the deposited material, redistributing it through the combined action of surface tension and gravity. Unlike mechanical and chemical finishes process, thermal processes do not remove material from the component, but are limited to rearranging its distribution. Two main sources of thermal energy have been used for this purpose, electron beams and laser beams. Laser beams have surely covered a more prominent role in this field, especially considering the number of related works published. Therefore, this section provides an in-depth review of laser finishing processes for DEDed components. The gaps and the limitations of the state-of-the-art in laser polishing were highlighted to provide a better understanding of the following research activity.

2.5.1 Laser Finishing

Laser finishing processes remelts the outermost deposited layer of the material in exam, smoothing its surface through surface tension and gravity, without affecting its bulk properties [65]. In the present document laser finishing processes were named laser polishing (LP) processes, to emphasizing surface finishing as the primary objective of the process. In fact, laser processes, such as laser remelting, can be also used during the manufacturing process, and not after it, for controlling material porosity, hardness and microstructure.

Laser polishing exhibits a high degree of flexibility, enabling the selective melting of a surface area while leaving the remainder intact [98]. Moreover, it does not involve a physical tool, by-passing all the issues related to material hardness and tool wear. No lubricants or cooling fluids are required during LP operations, clearly distinguishing it from CNC machining. The absence of auxiliary fluids can be helpful

in reducing the environmental impact of the process, and enables an easier integration between manufacturing and finishing operations. LP processes can be further divided into two categories according to the type of laser they use. Pulsed-wave LP uses pulsed lasers to remelt very thin material layers, typically a few tens of microns, whereas continuous-wave LP can melt thicker material layers, up to hundreds of microns [99, 100], as schematically represented in Figure 2.11. In this way, pulsed lasers are typically used for the removal of low-frequency roughness, particularly in finishing applications were the starting surface quality is already satisfactory. On the other hand, continuous wave lasers are better suited to the smoothing of more prominent roughness profiles, making them more appropriate for AM applications.

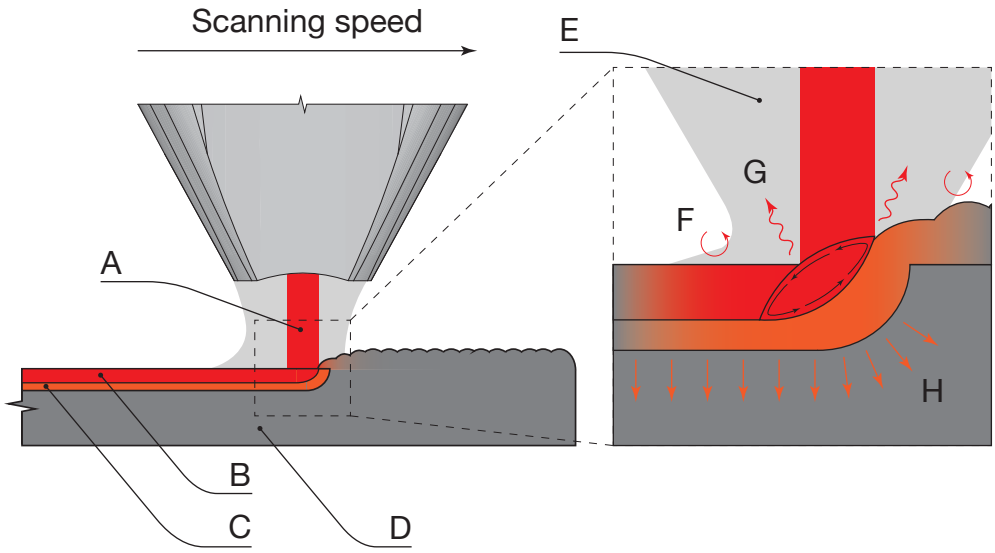

Fig. 2.11 Continuous-wave Laser Polishing scheme: A) continuous wave laser; B) remelted layer; C) heat affected layer; D) unaffected material; E) shielding gas; F) convection heat flow; G) radiation heat flow; H) conduction.

Several studies have proposed LP treatments to improve the surface quality of additively manufactured components, with a consistent scientific production focused on PBF-LB components [101, 102, 103, 104, 105]. However, in this specific scenario, DED-LB systems hold a fundamental advantage on PBF ones, making them predisposed for LP treatments. In a DED-LB system, either using wire or powder as feedstock material, there is already a laser suitable for LP operations, without the need of additional equipment. Therefore, the combination of DED-LB and LP might take place in the same system, using the same laser for both manufacturing steps, and strongly shortening the supply chain of the specific component. Since

no lubricants are required by the LP treatment, not preventing further depositions on the substrate, LP and DED can be effectively alternated. A meticulous process planning could ensure the deposition and finishing of complex geometries, finishing certain areas before they become difficult to reach [106]. Several works already investigated the suitability of LP to reduce the extreme roughness, and waviness, of DEDed components using the same laser for both manufacturing phases.

Rosa, Mognol, and Hascoët [106] LPed AISI 316L samples deposited by DED-LB/Powder. They achieved a drastic 95% reduction of samples Sa, lowering it from 21 to 0.8 µm. Five LP passes were carried out, with an energy density of 525 $\mathrm{J\,cm^{-2}}$ each. Santos Paes et al. [107] LPed samples deposited out of IRON AHC 100.29 and IN625, and compared the resulting surface improvements in terms of both Ra and Wa. Iron samples showed a 30% Ra reduction, whereas inconel ones a more consistent 70% Ra reduction. The superior response of IN625 samples was explained by its higher electrical resistivity and lower thermal diffusivity, which retained all the heat conveyed by the LP treatment near the surface. However, no meaningful Wa reduction were observed, neither for the iron nor for the inconel powder. Hodgir, Singh, and Mujumdar [108] deposited and LPed samples of CPM-9V crucible steel, remarkably decreasing Ra from around 80 to 20 µm, standing a 73% Ra reduction. They investigated the influence of laser power and travelling speed on the resulting quality of the polished surface, while keeping constant track overlap and laser spot diameter. Cho, Shin, and Shim [109] investigated the influence of LP process parameters such as laser power, tracks overlap, and scanning strategy on the surface quality of 316L samples deposited by DED-LB/Powder. Ra decreased from 15.64 to 1.5 µm, mainly influenced by laser power and overlap. Conversely, Wa decreased from 33.9 to 13 µm, especially due to the effect of overlap and scanning strategy. Bruzzo et al. [110] investigated the influence of laser power, tracks overlap and laser incident angle on the resulting $S_{a,sf}$ and $S_{a,lf}$, areal counterparts of Ra and Wa respectively. They managed to reduced $S_{a,sf}$ from 10.35 down to 1.82 µm and $S_{a,lf}$ from 9.57 down to 3.97 µm. Moreover, they highlighted strong non-linear effects for all quantitative factors involved. Various studied have also proposed hybrid laser finishing techniques for DEDed components, involving more consecutive laser treatments. Shen et al. [111] laser machined the outer surface of a DEDed Ti6Al4V sample, removing its outermost layer by laser ablation, and laser polished the resulting surface in a second finishing operation. Liu et al. [112] used a first pulsed laser followed by a continuous wave laser on the outer surface of an IN718

component deposited by DED-LB. Both experiences achieved meaningful surface quality improvements but required the use of other systems outside the DED one, placing themselves outside the scope of the current investigation.

2.6 Conclusions

In conclusion, several surface finishing processes might be used to improve the poor quality of DEDed components. Each process family has its own strengths, to be leveraged in the specific manufacturing scenario. Overall, LP processes here described seem to offer good surface quality without material waste and without the need of additional instrumentation outside the DED-LB system already at use [113]. However, an holistic experimental campaign is still lacking on the topic. Although the presented studies perfectly showed the capabilities of LP treatments, no clear factor screening campaigns have been performed, and no empirical models proposed to quantitatively correlate profile parameters to the process parameters investigated. Moreover, most of the studies in the field only referred to Ra and Sa, overlooking the potential information that other profile parameters might have embodied.

Chapter 3

Exploratory Experimental Campaign

From an engineering perspective, experimental campaigns have consistently served as the initial phase for the comprehension of industrial processes. However, observing a phenomenon and establishing a causal relationship between its observed behaviour and the underlying direct causes can prove to be a more challenging undertaking than initially anticipated. For this reason, experimental campaigns are often divided into subsequent smaller campaigns, each with a specific objective. This chapter describes the initial exploratory campaign, whose main objective was the definition of the LP process parameters that significantly impact the quality of the finished surfaces. In Section 3.1 the equipment used throughout the experimental campaign is presented. Section 3.2 applies the principles of inferential statistics to the problem of laser polishing treatments and chooses the most suitable experimental design for the exploratory experimental campaign in exam. Section 3.3 covers the design of the substrates required for the subsequent LP treatments, outlining their geometrical features and deposition stratagems. Section 3.4 discusses the preliminary experimental experience required to determine the levels of the stand-off distance of the deposition head, to be used during the campaign. Section 3.5 extensively reports the results obtained during the exploratory experimental campaign, primarily in terms of profile parameters. Section 3.6 focuses on the analysis of the defects found on LPed surfaces, while Section 3.7 draws conclusions.

3.1 Experimental Equipment

This section presents the DED-LB/Powder system used throughout this work of thesis, lists the machine characteristics and assesses the feasibility of LP treatments. In addition, the text provides a concise description of the metallic powder used in the experiments. Finally, the most relevant features of the stereo-microscope and of the roughness tester used for surface quality assessment are reported.

The DED-LB/Powder system used in this study was the Laserdyne® 430, a 5-axis commercial DED system provided by Prima Additive (Torino, Italy). This system combines a robust structure with a large working volume, ensuring at the same time great flexibility [114, 115, 116]. The machine was equipped with the TWA 160 roto-tilting table, by Tsudakoma Corp. (Kanazawa, Japan). The TWA 160 provides a 200 mm diameter base with T-slots, enabling a simple fixing of virtually any substrate, enhancing the flexibility of the system. The Laserdyne® 430 system was also equipped with the Advanced Head, featuring four radially distributed nozzles around the central laser beam. In the configuration used in this study, the focal plane of the powder stream and of the laser beam were disposed on the same plane at 8 mm from the nozzle. The laser module coupled with the system was the CF 1000 by Convergent Photonics (Torino, Italy), Yb fibre laser with a maximum power of 1 kW and nominal wavelength equal to 1075 ± 3 nm. The most significant laser characteristics were reported in Table 3.1.

The MetcoAdd 316L-D by Oerlikon (Freienbach, Switzerland) was the feedstock material used for sample deposition. The MetcoAdd 316L is a gas atomised austenitic stainless steel with a granulometry in the range from 45 to 106 µm. The spherical morphology of the powder can be fully appreciated in Figure 3.1, whereas Table 3.2 reports its nominal chemical composition. AISI 316L is one of the most widespread iron-based alloys for DED, mainly due to its good mechanical properties and outstanding corrosion resistance [72]. Moreover, the low carbon content of the alloy ensures an excellent weldability, enhancing its manufacturability by DED-LB/Powder.

The powder was stored in the CS 150, powder feeding system by Optomec (Albuquerque, NM, USA). In the CS 150, the powder is stored in a hopper that directly feeds an underlying chamber. A disk with radially distributed through holes divides the chamber by the following feeding system. The rotation of the disk

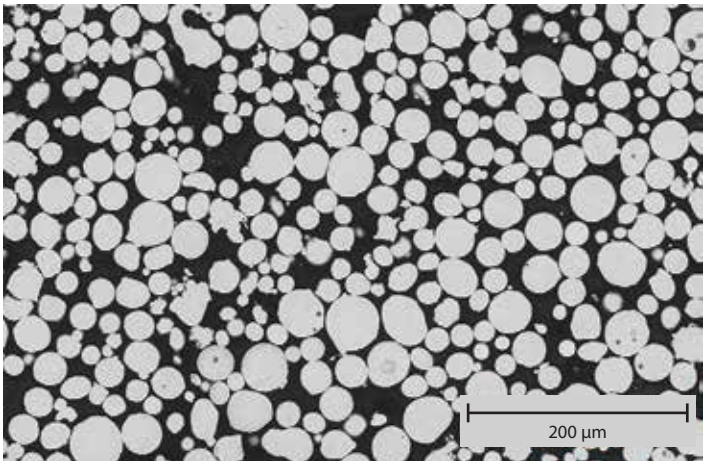

Fig. 3.1 Typical cross-section of MetcoAdd 316L gas atomised powder that demonstrates the spherical morphology and the fully dense inner structure of MetcoAdd 316-L products [117].

Table 3.1 Laser source characteristics.

Wavelength (nm)	Diameter (mm)	Min Power (W)	Max Power (W)
1075 ± 3	2	200	1050

fluidizes the powder in the chamber, allowing it to pass through the holes due to the action of an inert carrier gas. Pure argon was used both as carrier gas and as melt pool shielding gas.

The Leica S9i stereo-microscope, by Leica (Wetzlar, Germany) was employed for image acquisition and qualitative surface characterisation. The Leica S9i provides a 10 MP resolution on the focal plane, with a pixel size of (1.67×1.67) µm^2, and a high magnification of up to 55 times. Moreover, Leica's FusionOptics technology also grants a 12 mm depth of focus, drastically facilitating the use of the instrument.

Table 3.2 Nominal chemical composition of the MetcoAdd 316L-D expressed as weights percentages [117].

Fe	Cr	Ni	Mo	C	Others
Balance	18	12	2	< 0.03	< 1

The RTP-80, by SM Metrology Systems (Volpiano, Italy), was the roughness tester used for surface profile extractions and to perform subsequent quantitative

quality assessments. The RTP-80 is a stylus-based roughness tester that offers a 0.001 µm resolution over a ±500 µm measuring range.

Data collected by the physical instrumentation were analysed using Minitab, by Minitab LLC (State College, PA, USA). Minitab is a statistical software providing easy and accurate data analytics, from experimental designs to analyses of variance (ANOVA).

3.2 Experimental Design Definition

3.2.1 Response Variable Definition

The initial stage of an exploratory experimental campaign is the definition of the response variable. The execution of experimental trials in the absence of a clearly defined response variable may give rise to a number of issues that may prove challenging to resolve at a later stage. It is here recalled that the primary objective of this work has been the identification of an optimal set of process parameters to improve the surface quality of deposited samples. Therefore, it is necessary to select the most suitable parameters to quantitatively describe the texture of LPed surfaces. As already outlined in Section 2.2, both roughness and waviness profile parameters should be considered as they define the functions that LPed surfaces are able to fulfil. The study considered Ra, Rz, Rsk and Rku, along with their corresponding waviness parameters, aiming at an holistic description of surface textures. However, despite measuring and recording several parameters, Ra was chosen as the primary response variable, guiding the decisions made during the experimentation. The prominent role of Ra in scientific literature, international standards and real-life industrial applications made it impossible to opt for a different profile parameter.

3.2.2 Process Parameters Definition

After the definition of the response variable, it is also necessary to define the process parameters to be investigated. Exploratory experimental campaigns aim to screen all considered process parameters for active factors. Therefore, it is good practice to consider a large number of process parameters, limited only by resource availability. To guarantee that no potentially meaningful process parameters were omitted, the ini-

tial step was the analysis of the process parameters that were previously investigated and found to be significant in other studies. Table 3.3 reports the process parameters that have been investigated in published studies, as outlined in Section 2.5.1.

Laser polishing strategy was only considered in two out of five publications, divided in polishing tracks perpendicular to the deposited materials and polishing tracks parallel to the deposited materials. Bruzzo et al. [110] asserted that the parallel polishing strategy led to higher surface quality, both in terms of mean roughness and waviness. However, Cho, Shin, and Shim [109] stated the opposite, in particular regarding Wa. In other articles, Rosa, Mognol, and Hascoët [106] only used a perpendicular polishing strategy, Santos Paes et al. [107] only used a parallel polishing strategy, and Hodgir, Singh, and Mujumdar [108] did not make any statement on the topic. Therefore, the literature did not provide a conclusion solution regarding the LP strategy. All reported studies varied laser power, travelling speed, or both of them at the same time. Laser power and travelling speed are the most intuitive parameters that can be used to control the energy conveyed during the LP process. Thus, the relationship between energy employed and surface quality improvement has been proven to be strongly non-linear, with optimal quality defined for specific energy values. In addition, the hatching distance followed laser power and travelling speed as the most investigated parameter. The hatching distance is the distance between adjacent polishing tracks, also referred to as track overlap in the cited studies, and contributes in defining the energy conveyed during the process. A small hatching distance implies high polishing track overlap, resulting in a higher energy per unit area transmitted to the substrate. Finally, Bruzzo et al. [110] also considered the incident angle between the laser beam and the surface to finish. In their study, it was found that a perpendicular beam to the surface generally resulted in the worst quality after LP. The inclination of the laser beam improved both surface roughness and waviness. This behaviour was perfectly explained relating the inclination of the laser beam to the enlargement of the laser spot, leading to a lower energy density and ultimately to a better result. This results ensured that the inclination a laser beam do not represent a problem per se, but it should be considered when computing the energy used during LP.

On the basis of what was highlighted in previous articles, the current investigation performed LP treatments perpendicular to the last deposited layer. This was expected to reduce surface waviness by minimising the interaction between the as-built surface waviness and the LP treatment. Moreover, all LP treatments were performed holding

Table 3.3 Process parameters investigated in previously published studies.

	Laser Polishing Strategy (-)	Laser Power P (W)	Travelling Speed v ($mm\,min^{-1}$)	Hatching Distance h_d (mm)	Laser Incident Angle θ (deg)
Rosa *et al.* [106]		✓	✓	✓	
dos Santos Paes *et al.* [107]			✓		
Hodgire *et al.* [108]		✓	✓		
Cho *et al.* [109]	✓	✓		✓	
Bruzzo *et al.* [110]	✓	✓		✓	✓

the laser beam perpendicular to the surface, without any tilting. As laser beam inclination was only suggested to change the spot area, other equivalent expedients were investigated. Laser power and travelling speed of the deposition head were summarised in a single factor, the linear energy density (LED), to emphasise the prominent role that energy has over the two components from a physical perspective. LED is defined as the ratio between laser power and travelling speed, and it is already widely used in both welding and AM industries [118, 119]. Moreover, the hatching distance was also investigated as it allows for the conversion from LED to areal energy density, which has an even stronger physical meaning than the linear counterpart. In addition to the first two factors, the stand-off distance, S_d, of the deposition head with respect to the surface was also considered. Adjusting the stand-off distance of the deposition head could be a mandatory requirement to enhance LP accessibility during the treatment of complex geometries. By increasing the stand-off distance, the plane resulting from the interaction between the surface and the laser beam shifts from the original focal plane. The plane shifting results in an increase in the diameter and in the area of the laser spot. Therefore, controlling the stand-off distance during LP treatments should have a similar effect to the tilting of the laser beam. Finally, in addition to previous works, this thesis also investigated the influence of the shielding gas flow rate on the quality of the final surface. The

ambient gas in which the LP treatment takes place has a meaningful impact on surface morphology [120]. In general, the use of inert gases to reduce oxygen concentration in the molten area is necessary to achieve significant surface quality improvements [100]. However, an excessive shielding gas flow rate on top of the molten pool might even be detrimental, increasing the resulting surface roughness [121] and eventually leading to melt ejection [100]. Therefore, the argon flow rate, V_{Ar}, used as melt pool shielding gas, was varied to better understand its influence on the surface quality of DEDed components finished by continuous-wave LP.

In conclusion, four process parameters were selected for the current exploratory experimental campaign: linear energy density, hatching distance, stand-off distance and argon flow rate. The choices of the number of levels and of the quantitative values of the chosen levels were extensively discussed in Sections 3.2.3 and 3.2.4.

3.2.3 Factorial Designs

The identification of the response variable and of the process parameters of interest are the necessary preliminary operations for a profitable experimental campaign. Once these aspects have been consolidated, the most appropriate experimental design can be selected with full awareness. A common experimental strategy in scientific literature is the one-factor-at-a-time approach. This approach consists in selecting a baseline level, or reference value, for each parameter, and subsequently in varying one factor while keeping the others constant at their baseline values [122]. Although this approach allows a clear identification of the effects of each parameter involved, it is still strongly limited. Considering that the parameters are varied one at a time, any potential interaction is, by default, overlooked. An interaction can be defined as "*the failure of one factor to produce the same effect on the response at different levels of another factor*" [123], therefore requiring the concurrent variation of more than one factor to manifest. Factorial designs of experiments succeed in doing exactly so, varying more than one factor at the same time and ensuring that "*in each complete trial or replicate of the experiment, all possible combinations of the levels of the factors are investigated*" [123]. Table 3.4 shows an example of the experimental trials required to complete a factorial design with two factors and two levels per factor. The high level of a factor is indicated by 1, while -1 indicates its low level. The resulting experimental trials were named according to the common nomenclature, often used to address the specific combination of process parameters.

Factorial designs were first introduced by Ronald Fischer at the beginning of the 20^{th} century [124, 125], building on the principles of inferential statistic developed in the 19^{th} [126]. Nonetheless, factorial experiments are able to provide a clear description of the effects of the factors and of their interactions, still representing the standard in industrial research.

2^k Factorial Designs

A fundamental advantage of factorial designs is the possibility of dividing the experimental activity into multiple sub-phases. Each sub-phase has a different shape, tailored to its specific objective. Usually, experimental campaigns starts with an exploratory phase, whose role is the identification of the active factors among the considered ones. A factor is considered active if its perturbations have a clear and distinguishable influence over the chosen response variable. Therefore, at this stage the experimenter usually manages more factors than the one really needed to control the response variable. Exploratory campaigns are required to be extremely resource-efficient, reducing their own cost to the minimum in terms of raw materials, time and energies. In particular, exploratory campaigns usually use only two levels for each investigated factor [123]. Two-levels factorial designs are commonly referred to as 2^k factorial designs, where k is the number of investigated factors. This simple notation perfectly highlights the number of overall trials as an exponential function of the investigated factors. The use of only two levels reduces to the minimum the resources needed to conduct the experimentation, at the cost of neglecting possible non-linear effects of the factors. In fact, a minimum of three levels is required for a description of non linear effects and for allowing the bending of the characteristic effect plots. However, a perfect description of the complex dynamic of the effect

Table 3.4 Experimental trials required to complete a full factorial design investigating 3 factors over 2 levels each. -1 indicates the low level of the factor, whereas 1 indicates the corresponding high level.

A	B	
−1	−1	(1)
1	−1	a
−1	1	b
1	1	ab

of the factors is usually outside the scope of exploratory campaigns, and typically demanded during the subsequent optimisation campaigns.

Full Factorial Designs

Moreover, two possible designs are available for 2-level factorial experiments: full factorial designs and fractional factorial designs, graphically represented in Figure 3.2. Fractional experimental designs take to the extreme the concept of resource efficiency provided by 2^k designs. Without going too deep in the theoretical aspects of experimental design, fractional designs reduce the resource impact of the experiment, at the cost of confounding some of the effects of the factors between them. This phenomenon is known as aliasing and its extent depends strongly on the type of design used. For examples, in the case of the half fraction reported in Figure 3.2, 2^{3-1} design, the main effects are not aliased with each other, but the two-way interactions may be aliased with main effects or with each other. Therefore, fractional designs can introduce additional complexity during the interpretation of the results, making it not always straightforward. On the contrary, full factorial designs are straightforward to handle, both during and after the experimental phase. Although it required more resources than its fractional counterpart, a 2^k full factorial design was chosen for the current investigation. Setting k to four, number of the investigated factors, gives a 2^4 full factorial design of 16 experimental trials.

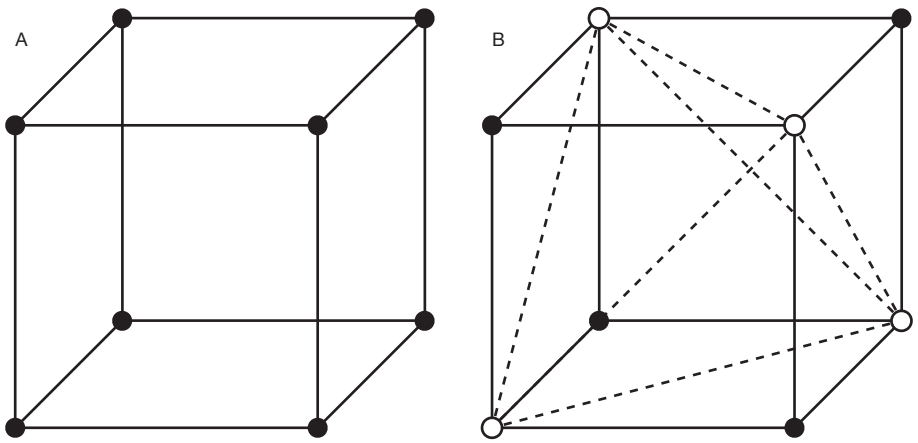

Fig. 3.2 Graphical representation of the one-half fraction of a 2^3 factorial design; A) full factorial design; B) one-half fractions (either black or white vertices).

Replications, Randomisation and Central Points

Other aspects of the experimental campaign must be covered before its complete definition. Firstly, experimental trials should be replicated to increase the precision of the campaign [124]. A replicate of an experimental run involves a complete repetition of the trial, starting with the setup up to its conclusion. A large number of replicates can reduce the impact of uncontrollable nuisance factors that introduce random variability in the response variable. Replicates enhance the capability of the experiment to detect small differences in the response variable, overcoming the random noise caused by nuisance factors. Therefore, studies conducted without replicated runs may draw weak conclusions on the investigated topic [127], as they may not be completely able to detect small effects. In this work, the experimental campaign consisted of three replicates of each factorial point, assuming the structure of a 3×2^4 experimental campaign, and resulting in a total of 48 experimental runs. Secondly, another cornerstone of industrial experiments is the randomisation of the experimental runs. Randomised runs can reduce the influence of unknown bias on the response variable, such as instrumentation drift or uncontrollable changes in the environmental conditions [124]. Therefore, prior to their execution, all 48 runs of the experimental campaign were randomised. Finally, central points have been added to the experimental campaign.

As previously described, the necessary choice of a 2^k design prevented the quantification of any non-linear effect during the experimental campaign. The addition of central points can partially solve the problem by providing an estimate of the overall contribution of non-linear effects. A 2^k design with central points can be considered an intermediate solution between 2^k designs and more complex solutions, such as 3^k designs, Central Composite Designs or Box-Behnken designs. Although 2^k designs with central points cannot distinguish the non-linear effects of each single factor, they can still provide a single estimate of the sum of all these effects. Whether this sum is deemed significant, there is a high likelihood that non-linear effects have a meaningful role in the distribution of the results. Figure 3.3 shows an example of a 2^2 factorial design, where the addition of the central point implied the presence of significant non-linear effects. Therefore, 5 central points were introduced in the experimental campaign to provide an estimate of the non-linear effects in action, and bringing the total number of required experimental runs to 53. Table 3.5 reports

the randomised order of the experimental run. Levels are only indicated in coded variables since their quantitative values have not been discussed yet.

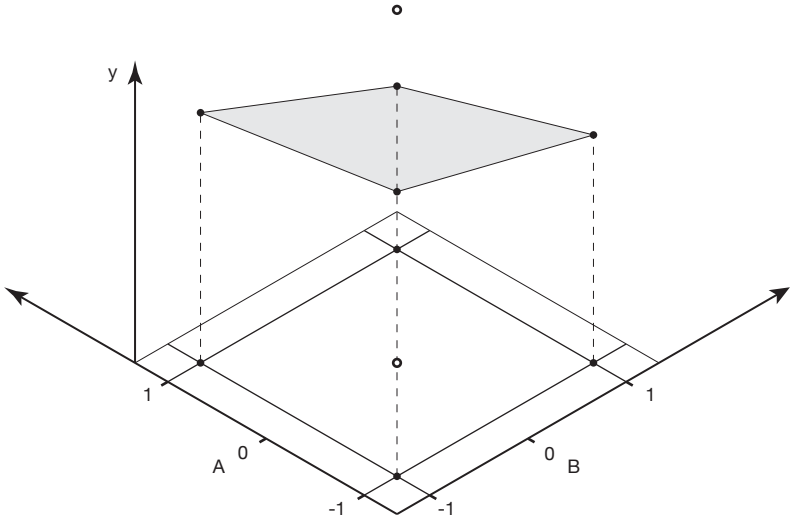

Fig. 3.3 Example of a 2^2 design with central point.

Table 3.5 Run order of the 53 treatments composing the exploratory campaign. Low and high levels of investigated factors are reported in coded variables.

Run number	LED	h_d	S_d	V_{Ar}	Run number	LED	h_d	S_d	V_{Ar}
1	1	−1	−1	1	28	1	−1	−1	−1
2	1	1	1	−1	29	−1	−1	1	−1
3	−1	1	1	1	30	−1	−1	−1	−1
4	1	1	−1	−1	31	−1	−1	−1	−1
5	−1	−1	1	1	32	1	−1	1	1
6	−1	1	1	−1	33	−1	−1	−1	1
7	1	−1	−1	1	34	1	1	1	−1
8	−1	1	−1	1	35	1	1	1	1
9	1	1	−1	1	36	−1	−1	1	1
10	1	−1	1	1	37	1	1	−1	1
11	−1	1	1	−1	38	−1	−1	1	1
12	−1	−1	−1	1	39	1	−1	−1	−1
13	−1	−1	−1	−1	40	−1	1	1	1
14	−1	1	−1	1	41	1	1	−1	−1
15	1	−1	1	−1	42	1	−1	−1	1
16	−1	1	1	−1	43	1	1	1	1
17	1	1	−1	1	44	−1	1	−1	−1
18	1	1	−1	−1	45	1	−1	1	−1
19	−1	−1	1	−1	46	−1	−1	1	−1
20	1	−1	−1	−1	47	−1	1	1	1
21	−1	−1	−1	1	48	1	−1	1	1
22	1	−1	1	−1	49	0	0	0	0
23	1	1	1	−1	50	0	0	0	0
24	−1	1	−1	−1	51	0	0	0	0
25	−1	1	−1	−1	52	0	0	0	0
26	1	1	1	1	53	0	0	0	0
27	−1	1	−1	1					

3.2.4 Level Definition

In a 2^k experimental campaign, it is generally good practice to cover the widest possible domain by spreading the factorial levels as far apart as possible. Starting from the LED, its central level matched the LED value used during sample deposition. Low and high levels were selected at a distance far enough from the central value while still remaining within the processability window of the material. The underlying assumption was that the material would have behaved well under both deposition and LP when using the same LED. Secondly, the h_d value was chosen based on the diameter of the laser spot in its focal plane. The h_d low level was set to 1 mm, which is equal to half laser spot diameter, implying a 50% superposition between consecutive LP tracks. Whereas the high level of h_d was set to 2 mm, equal to the laser spot diameter and resulting in no theoretical superposition between LP tracks. S_d low level was maintained at the value used during deposition, indicating that no defocusing occurred. Conversely, the definition of the high level of S_d required additional care and was extensively discussed in Section 3.4. Finally, the low and the high levels of V_{Ar} were limited by the flow meter fitted to the CS 150. Table 3.6 reports the quantitative values of the factorial levels.

3.3 Substrate Definition: Geometrical Features and Deposition Strategy

The LP experimental campaign required DEDed substrates to accommodate the experimental trials. This section presents the geometrical features of the DEDed substrates, specifically designed to satisfy the requirements imposed by the international

Table 3.6 Levels of the investigated factors.

Factor	Low level	High level	Central point
$LED/(\mathrm{J\,mm^{-1}})$	21	70	45.5
$h_d/(\mathrm{mm})$	1	2	1.5
$S_d/(\mathrm{mm})$	8	28	18
$V_{Ar}/(\mathrm{L\,min^{-1}})$	2	10	6

standards. Most of these geometrical features, together with additional information, are also shown in Figure 3.4.

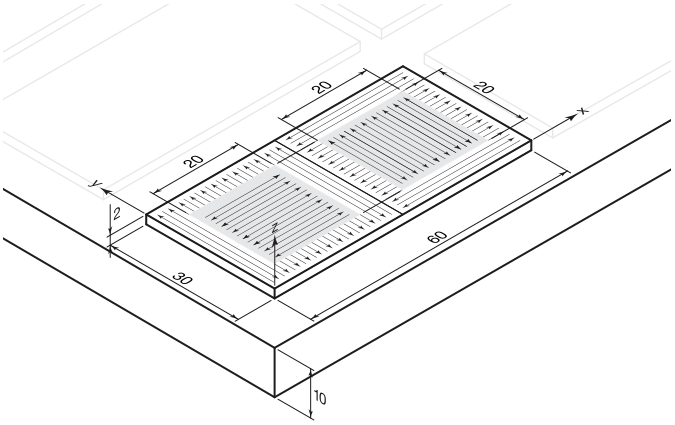

Fig. 3.4 Dimensions of the substrate employed for LP treatments, and of the areas undergoing LP treatments.

It has been already proven that the upper surface of DEDed samples tends to have a higher Ra value [47, 128]. Therefore, the substrates were designed to accommodate the LP treatments on their upper surface, starting from the most critical condition. In particular, ISO 21920-3 [129] gathers all the practical suggestions that the operator has to follow for a reliable assessment of the surface roughness. The main prerequisite to be met by the surface under test relates to the evaluation length, whose prescribed value increases for rougher surfaces. The deposition of a unique wide substrate was discarded because it would have induced dramatically high stresses and deformations within the base platform. Instead, the deposition of various smaller substrates was considered more easily manageable. Therefore, ISO 21920-3 reports the prescribed acquisition lengths as a function of the estimated R-profile parameter. Since DED-LB/Powder samples typically have Ra values well above the 10 µm threshold, the prescribed l_e is equal to 40 mm. An additional 8 mm should be added to obtain the overall transverse length required by the roughness tester. Therefore, considering a minimum length of 48 mm and willing to avoid any border effect, the substrate length was set to 60 mm along the acquisition direction. The second dimension of the substrate was determined by the dimensions of the LP area. As for the as-built condition, the minimum acquisition length of the LP areas depended on the expected outcome. As outlined in Section 2.5, the Ra value of LPed surfaces would likely have been below the 10 µm threshold, suggesting an l_e of 15 mm. Once more, to make room for the transverse length and to avoid border

effects, the LP area was dimensioned at (20×20) mm^2. Thus, the second dimension of the substrate was set to 30 mm to easily accommodate the LP area, resulting in a (30×60) mm^2 substrate. Up to three LP treatments could be contained in a single substrate, number that was reduced to two in order to avoid any possible interaction between adjacent treatments. Four layers of 0.5 mm each were sequentially deposited for a total substrate height of 2 mm. An island deposition strategy with 90° rotation between layers was used to further reduced the residual stresses induced during the deposition. Table 3.7 presents the process parameters used for substrates deposition. Since only two LP treatments could be performed on every substrate, and recalling that 53 trials were required by the experimental campaign, 27 substrates were planned for deposition. Two AISI 316L platforms, $(210 \times 210 \times 210)$ mm^3, were used to accommodate all 27 substrates.

3.4 Preliminary Campaign: Stand-off Distance

Table 3.6 in Section 3.2 anticipated the value of the high level of the stand-off distance, equal to 28 mm. The present section presents a preliminary, and concise, experiment performed to consciously define this value.

The primary objective of the experiment was the correlation of the stand-off distance with the laser spot diameter. Therefore, the laser spot diameter was selected as response variable, with the stand-off distance being the only investigated factor. Laser marks were produced on a 10 mm thick platform of AISI 316L by activating the laser of the Laserdyne® 430 for 0.4 s with a power of 700 W. The time 0.4 s is the interval required by the deposition head to cover a distance of 2 mm, equal to the spot diameter, at a traveling speed of 600 mm min^{-1}, equal to the travelling speed used for LP. Five levels of the stand-off distance were investigated while maintaining a

Table 3.7 Process parameters used for substrate deposition.

Laser Power P (W)	Travel speed v (mm min^{-1})	Layer height ΔZ (mm)	Hatching distance h_d (mm)	Powder flow rate Q_P (g min^{-1})	Argon flow rate Q_{Ar} (L min^{-1})
700	850	0.5	1	4	6

constant laser power and activation time. The high number of levels used was easily justified by the simplicity of the trials, for they did not required significant resources or time. Six replicates of each experimental trial were performed to increase the likelihood of detecting even small differences in laser marks diameters. The Leica S9i was used to capture images of the marks and to measure their diameters. Minitab was used to perform an ANOVA on the obtained results, to better clarify the functional relationship between laser spot diameter and S_d.

Table 3.8 reports the results of the experiments. Repetitions of the same experiment were aggregated in terms of mean value and standard deviation for the sake of conciseness. Results were also analysed in Minitab using a 1-way ANOVA. Assuming a 95% level of confidence, the S_d was found to be significant (p-value < 0.001) and explained most of data variability (R^2 = 98.44%). A closer examination of the meaning of the p-value test, R^2 and all other coefficients computed during the ANOVA is reported in Annex A. Figure 3.5 shows that only the highest S_d level resulted in a sensible change in laser mark diameter. A 28 mm S_d ensured a laser mark diameter of approximately 2.40 mm, showcasing a consistent 44% increase in the laser mark area. That is why it was also selected as S_d high level in the exploratory experimental campaign, as reported in Table 3.6.

Table 3.8 Results of the experiment for the definition of the S_d high level. Experiment replications aggregated as mean and standard deviation.

Stand-of distance S_d (mm)	Mean diameter ϕ (mm)	Standard deviation σ (mm)	Area A (mm^2)
8	2.07	0.01	3.37
10	2.06	0.03	3.32
12	2.06	0.02	3.33
18	2.07	0.01	3.37
28	2.39	0.01	4.47

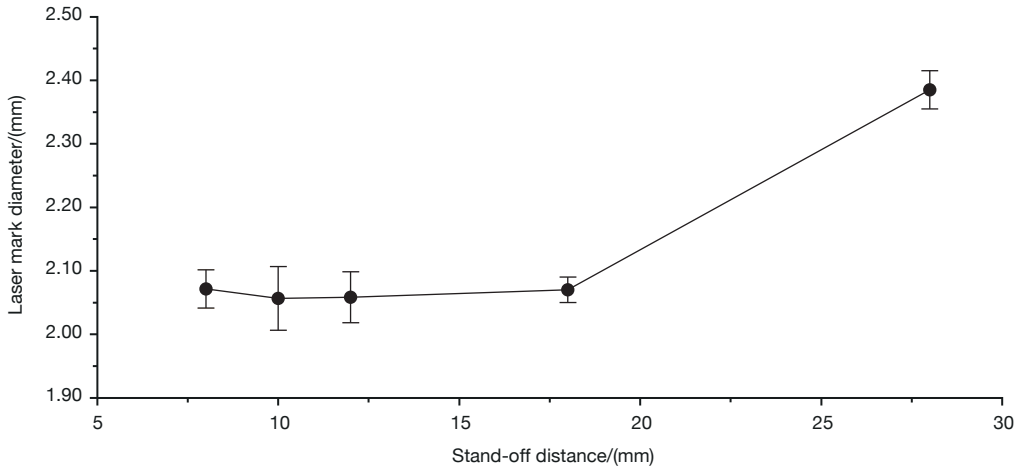

Fig. 3.5 Results of preliminary campaign aimed at the identification of the stand-off distance high level.

3.5 Results

3.5.1 As-built Surface Characterisation

The deposition of the substrates required by the LP treatments was carried out as outlined in Section 3.3. Images of the upper surface of the substrates were captured by the Leica S9i for visual inspection. R-profile and W-profile parameters were computed by means of the RTP-80. To ensure a representative result of the entire surface, five measurements were repeated on every sample at different locations. An ANOVA on the 27 Ra mean values, obtained this way, was performed to assess the equivalence of the substrates for the subsequent LP treatments. Ra was the response variable considered, whereas the investigated levels were the substrate themselves. The ANOVA did not highlight significant differences between the mean Ra values of the deposited substrates, at a 95% confidence level (p-value = 0.119). As the substrates can be considered equivalent, the mean values of the parameters for the 27 samples were further averaged in a common as-built condition. Table 3.9 collects both R and W-parameters computed using this method. Ra and Wa values were in accordance with literature [47, 112, 130], suggesting no meaningful deviation of the DED-LP/Powder process in exam from common behaviour.

The high Rz value indicates an extremely indented surface, with high peaks and deep valleys. Moreover, the Rsk value close to zero suggests an R-profile sym-

Table 3.9 R-profile parameters and W-profile parameters for a complete characterisation of the as-built surface of substrates.

Ra (µm)	Rz (µm)	Rsk (-)	Rku (-)	Wa (µm)	Wz (µm)
23.60 ± 2.21	152.58 ± 9.86	0.12 ± 0.11	3.24 ± 0.34	22.14 ± 9.80	102.90 ± 38.74

metrically distributed about its mean value, without the presence of plateau-like behaviours. Finally, the Rku value close to three highlights a normal distribution of the probability density function representing the ordinate values of the profiles. Overall, the generic R-profile of as-built surfaces exhibited a highly chaotic behaviour, with no specific features. The irregularities in the as-built surface may be partially attributed to the consistent presence of partially sintered powder particles, as clearly depicted by Figure 3.6.

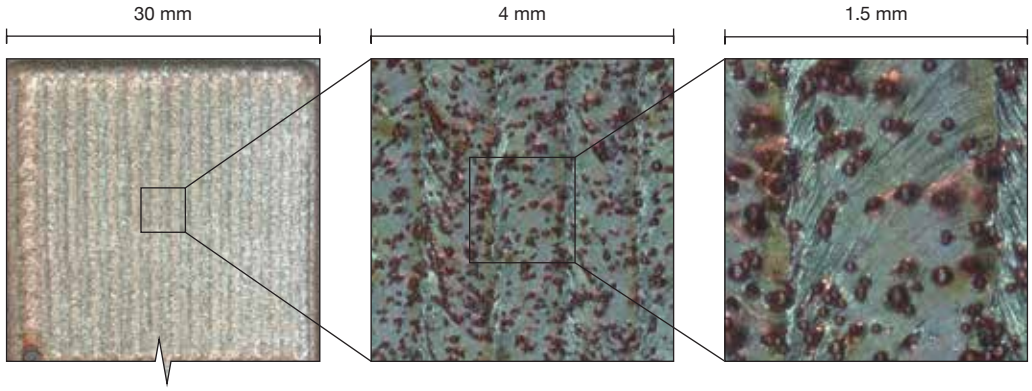

Fig. 3.6 Visual inspection of surfaces in as-built conditions with details of sintered powder particles.

3.5.2 LP Results

The LP treatments were performed following the randomised order presented in Table 3.5. The Leica S9i was used to capture pictures of the each treatment, and the RTP-80 used for roughness evaluation. Five roughness measurements were taken, both along the direction of polishing tracks (x direction) and perpendicularly to it (y direction), as shown in Figure 3.7.

The same Figure 3.7 shows the bar chart of the results for both $Ra_{\perp}$ and $Ra_{\parallel}$. The height of the each bar represents the mean Ra mean value over the three replicated

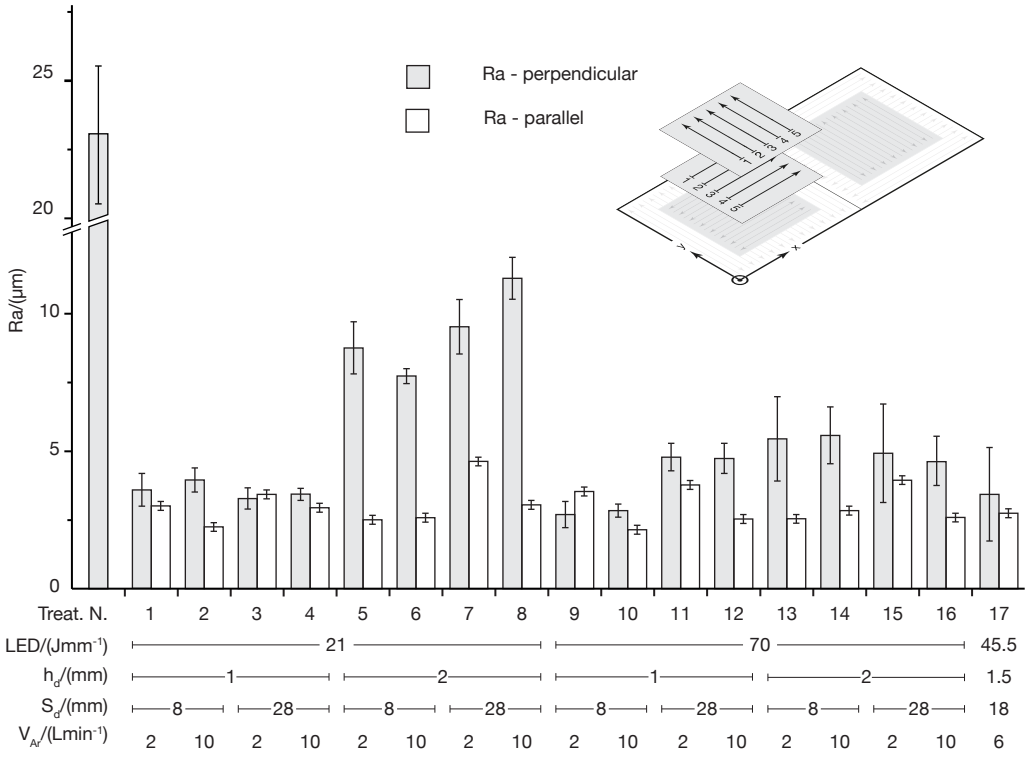

Fig. 3.7 Results of the exploratory campaign in terms of Ra.

samples, whereas the error bars are equal to twice the standard deviation computed over the three replications. In this way, the error bars provides a clear visual understanding of the superposition of confidence intervals for the mean values. Upon close inspection, it appears that $Ra_{\perp}$ consistently exhibits higher values than its parallel counterpart, suggesting that the perpendicular direction was the most critical of the two. This consideration alone would be sufficient to set aside the parallel measures. In fact, ISO 21920-3 [129] emphasises the importance of considering the direction of higher roughness when performing surface characterisation procedures. Before setting aside the $Ra_{\parallel}$, a correlation analysis was performed to enhance a finer understanding of the relationship between $Ra_{\perp}$ and $Ra_{\parallel}$.

The Spearman correlation coefficient was used to quantify the correlation between the two coefficients due to its wide use in the scientific literature [131]. LP treatments were ranked from best to worst to proficiently use the Spearman correlation coefficient. Therefore, two rankings where obtained, one for $Ra_{\perp}$ and one for $Ra_{\parallel}$. The Spearman correlation coefficient is computed as described by Equation 3.1. The variable n represents the number of distinct elements composing the rankings,

and d_i represents the ranking difference of each LP treatment. From its mathematical definition, the Spearman correlation coefficient is strictly bounded between ± 1. Values closer to the extremes suggest a strong correlation between the compared variables. Positive values suggest a direct correlation, whereas negative values suggest an inverse correlation. On the other hand, a value close to zero suggests that there is no functional relationship between the rankings. Figure 3.8 displays the results of the correlation analysis, whose value of $r_s = 0.752$, computed at a 95% confidence level, suggests a strong correlation between the rankings. This result was considered of the utmost importance since it ensures that LP treatments could be similarly ranked using both $Ra_{\perp}$ and $Ra_{\parallel}$. Therefore, the present study focused only on the perpendicular parameters acquired, being confident that no meaningful differences were overlooked. This choice should improve the conciseness and clarity of the work, helping the reader to better navigate trough the document. However, the complete data sets are available in Appendix C for consultation.

$$r_s = 1 - \frac{6\sum_{i}^{n} d_i^2}{n(n^2-1)} \tag{3.1}$$

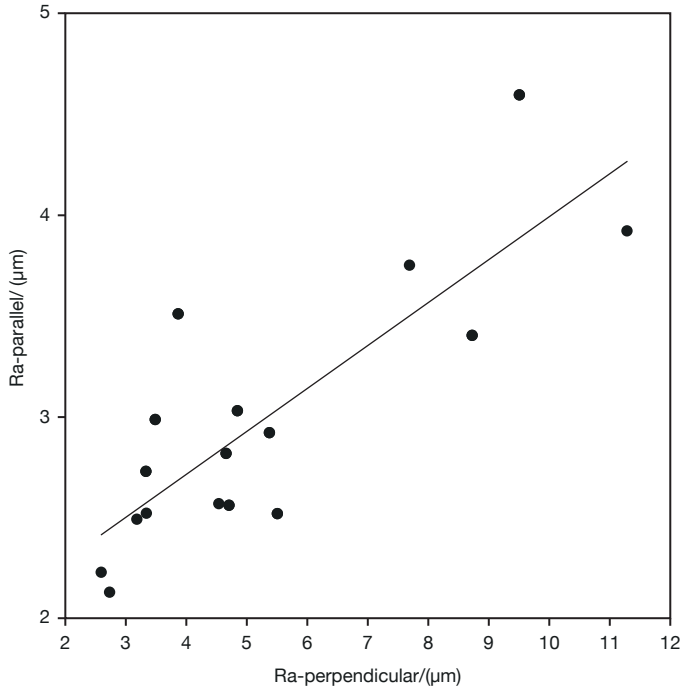

Fig. 3.8 Graphical representation of the correlation between $Ra_{\perp}$ and $Ra_{\parallel}$.

The bar chart in Figure 3.7 highlights the LP treatments that achieved the best and worst surface quality. Treatment N.8 resulted in the least reduction of $Ra_{\perp}$, which was still equal to a 53.5% reduction of the initial value, and to a final value of (11.2 ± 0.4) µm. Treatment N. 8 employed low LED, high h_d and high S_d, resulting in the lowest energy density out of the entire experimental campaign. Moreover, the high value of V_{Ar} likely contributed to a faster cooling of the melt pool, already enhanced by the low energy density. On the other hand, Treatment N.9 produced the most consistent reduction of $Ra_{\perp}$, equal to the 88.7% of the as-built value. Thus, $Ra_{\perp}$ of (2.7 ± 0.2) µm was obtained with high LED level, and low levels of h_d, S_d and V_{Ar}. Although the primary objective of the exploratory experimental campaign was not the achievement of a specific Ra threshold, as for the other parameters, the drastic reduction in roughness of the samples was not overlooked. Thus, the combination that yielded the best result also considered the highest energy density among the investigated ones. This meaningful evidence was later confirmed by the results of the ANOVA. Table 3.10 contains all R and W-profile parameters for a comprehensive characterisation of the substrate polished by Treatment N.9. The drastic reduction of $Ra_{\perp}$ was followed by an even greater $Rz_{\perp}$ reduction, equivalent to 91.7% of the initial value. This result ensures that, apart from an averagely smooth surface, no sudden peaks or valleys were created by the LP treatment. Moreover, the value of $Rsk_{\perp}$ close to zero suggests high profile symmetry about its mean line, while the $Rku_{\perp}$ close to three suggests a normally distributed probability function of the ordinates of the measured profile. Overall, the R-profile appears to be extremely smoother, without critical features worth citing. Similar considerations might be proposed for the W-profile as well. $Wa_{\perp}$ was reduced by 63.3% and $Wz_{\perp}$ was reduced by 67.0%. The limited impact of LP on W-profile parameters was anticipated by the already demonstrated difficulties that LP faces in modifying the W-profile [132]. Although the waviness reduction was more contained than the roughness one, it still represents a promising outcome for the following experimental phases.

Table 3.10 R-profile parameters and W-profile parameters for a complete characterisation of the surface of the substrates polished by Treatment N.9.

$Ra_{\perp}$ (µm)	$Rz_{\perp}$ (µm)	$Rsk_{\perp}$ (-)	$Rku_{\perp}$ (-)	$Wa_{\perp}$ (µm)	$Wz_{\perp}$ (µm)
2.68 ± 0.24	12.68 ± 0.82	-0.10 ± 0.04	2.49 ± 0.06	7.58 ± 1.05	33.94 ± 5.42

The effects of LP treatment N.9 is also clearly illustrated in Figure 3.9. The as-built surface of the substrate is displayed alongside the profile acquired by the roughness tester. Both the image and the profile show the poor surface quality of the DEDed substrate, with a significant presence of sintered powder particles. The LP treatment was able to completely remove all sintered powder particles from the surface of the substrate, leaving no residual particles visible after the treatment. The LP treatment seemed also capable of removing the underlying form error due to deposition tracks, typical of any DED-LP/Powder process. No meaningful oxidation appears to have occurred, suggesting that even a modest argon flow rate was effective in profitably shielding the molten pool from the oxygen in the environment. However, a new texture was created on the LPed surface. Polishing tracks were clearly visible, and their presence confirmed also by the R-profile acquired by the roughness tester. Moreover, inside every polishing track the solidification fronts of the molten pool were also clearly visible.

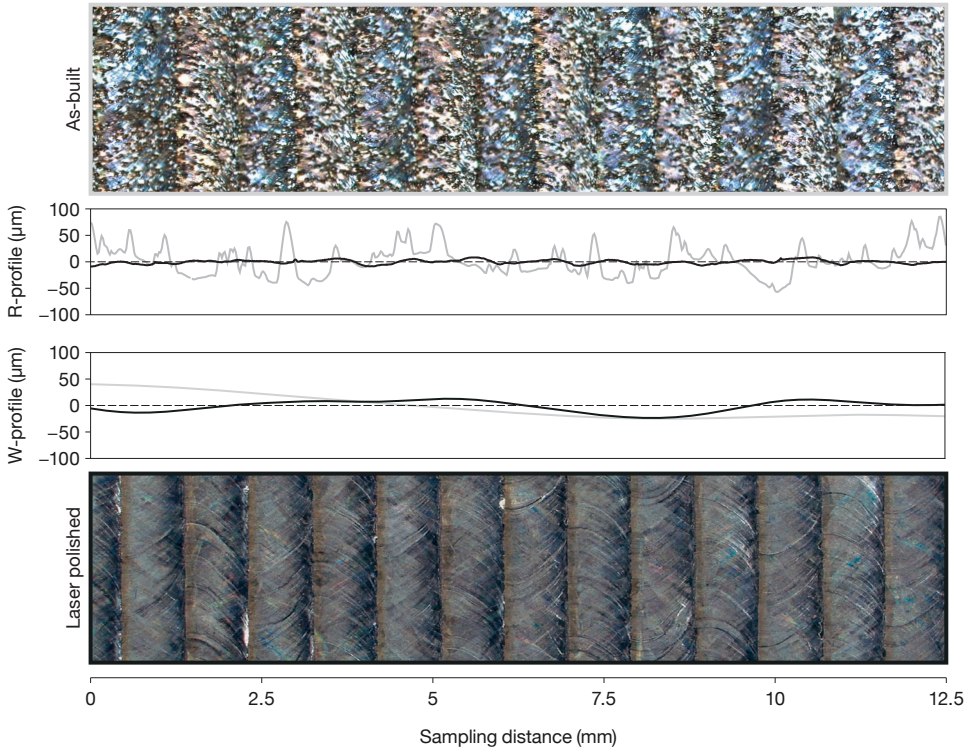

Fig. 3.9 Comparison of as-built and sample surface LPed by Treatment N.9.

More powerful statistical tools were required in order to deepen the understanding on the influence of process parameters on the quality of LPed surface. Section 3.5.3 presents the main results of the ANOVA and the following empirical models.

3.5.3 ANOVA and Response Surface

ANOVA for $Ra_{\perp}$

Table 3.11 collects the results of the ANOVA that considered $Ra_{\perp}$ as response variable. The ANOVA was able to estimate the significance level of the investigated process parameters, and of all interactions, due to choice of using a full factorial design, drastically easing the interpretation phase. The p-value column highlights that three out of the four process parameters were statistically significant at a confidence level above 99.9%. Only V_{Ar} was found not significant for the definition of the response variable, being significant only at confidence level of 76.5%. Similarly, the 2-way interaction between LED and h_d was found to be significant at a confidence level above 99.9%. Furthermore, moving at higher order interactions, two 3-way interactions and the 4-way interaction were found significant. Finally, the curvature term was also significant with a confidence level above 99.9%

Limiting the discussion on the mere statistical significance of the investigated parameters and their interactions may lead to a misinterpretation of the results. The p-value test alone does not provide a source of information for estimating the effect size of the significant factors [133], which is usually the most meaningful aspect from an engineering perspective. Therefore, the additional η^2 coefficient was introduced to compare the relative effect sizes of the different factors [134, 135]. The η^2 coefficient is defined as the ratio between the Adj SS of a factor and the total Adj SS. It provides a straightforward indication of the percentage of the total variability of the system accounted by a single factor. For instance, the η^2 coefficient of h_d was equal to 0.477, suggesting that h_d alone covered almost half of the whole data variability. On the contrary, several other significant parameters such as the S_d, the 3-way interactions, the 4-way interaction, and the curvature terms had all low η^2 coefficients, suggesting a secondary role in data distribution.

Figure 3.10 integrates the information provided by table 3.11 by displaying the factorial plots of the main effects, i.e. the effects of the process parameters

Table 3.11 ANOVA for $Ra_{\perp}$.

		DF	Adj SS	Adj MS	F-value	p-value	η^2
Model		16	307.952	19.247	80.94	0.000	0.973
	LED	1	47.088	47.088	263.94	<0.001	0.149
Linear	h_d	1	151.201	151.201	847.53	<0.001	0.477
Terms	S_d	1	6.708	6.708	37.60	<0.001	0.021
	V_{Ar}	1	0.261	0.261	1.46	0.235	0.021
	LED·h_d	1	57.063	57.063	319.86	<0.000	0.180
	LED·S_d	1	0.182	0.182	1.02	0.320	0.001
2-Way	LED·V_{Ar}	1	0.340	0.340	1.91	0.177	0.001
Interactions	$h_d \cdot S_d$	1	0.019	0.019	0.11	0.744	<0.001
	$h_d \cdot V_{Ar}$	1	0.001	0.001	0.00	0.950	<0.000
	$S_d \cdot V_{Ar}$	1	0.702	0.702	2.94	0.056	0.002
	LED·$h_d \cdot S_d$	1	20.888	20.888	117.08	<0.001	0.066
3-Way	LED·$h_d \cdot V_{Ar}$	1	0.041	0.041	0.23	0.633	<0.001
Interactions	LED·$S_d \cdot V_{Ar}$	1	1.883	1.883	10.55	0.003	0.006
	$h_d \cdot S_d \cdot V_{Ar}$	1	1.405	1.405	7.87	0.008	0.004
4-way Interaction	LED·$h_d \cdot S_d \cdot V_{Ar}$	1	1.952	1.952	10.94	0.002	0.006
Curvature		1	18.218	18.218	76.61	<0.001	0.058
Error		36	8.561	0.238			0.027
Total		52	316.513				

investigated. In fact, table 3.11 is limited to assessing the significance of the process parameters, but does not provide any information on the functional relationship between process parameters and response variable. In the main effect plots, acquired data are divided in two clusters based on the low and high levels of the considered factor, the average of each cluster is computed, and the results plotted. Therefore, the slope of the resulting segment provides valuable details on how the process parameters affect the response variable. From Figure 3.10 it is straightforward to notice how a high energy density resulted in better surface quality after LP treatments. In particular, high levels of LED and low levels of h_d and S_d ensure lower $Ra_{\perp}$ at end of the treatment. On the other hand, V_{Ar} changes do not have a meaningful influence on $Ra_{\perp}$, confirming the results of the ANOVA. Finally, the average value of the central points is also reported to complete the description.

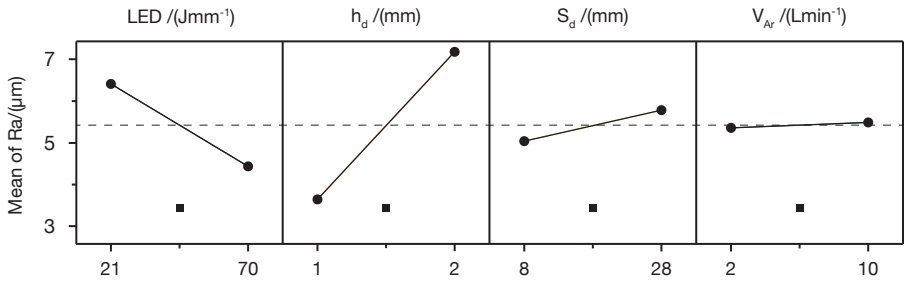

Fig. 3.10 Main effect plots for $Ra_{\perp}$.

Similarly, Figure 3.11 shows the 2-way interaction plots. It is here recalled that a significant 2-way interaction implies a different behaviour of a first process parameters for different levels of a the second process parameter considered. In particular, focusing on the interaction between LED and h_d, the effect of the LED can be appreciated only when h_d is maintained at its high level (as shown by the segment with white extremes in Figure 3.11). Conversely, changes of LED become almost negligible when h_d is maintained at its low level (as shown by the segment with black extremes in Figure 3.11). This specific behaviour can be attributed to the higher effect size of h_d compared to LED. When h_d is maintained at its low level, its larger effect size does not allow LED changes to be fully appreciable. This result is in partial disagreement with the conclusions of Cho, Shin, and Shim [109], who observed that high laser power and small h_d led to lower Ra values. The difference may be ascribed to the different ranges of the process parameters levels investigated during the studies. It is always important to contextualise the results of different studies according to their investigated domain. Additionally, minor interactions can also be noticed for LED $\cdot$ V_{Ar} and S_d $\cdot$ V_{Ar}. As for LED $\cdot$ V_{Ar}, differences on the influence of V_{Ar} could only be noticed for low levels of LED. At low LED levels, slightly better results were measured for the low V_{Ar} level, in accordance to previous studies. In particular, high shielding gas flow rate could result in Marangoni instabilities, altering the convective flows of molten material inside the melt pool, thus affecting the quality of the LPed surface in turn [121]. Understanding the interaction between S_d and V_{Ar} is substantially more complex. If S_d is maintained at its high level, low V_{Ar} values results in lower $Ra_{\perp}$ values, in agreement to what already discussed for the LED $\cdot$ V_{Ar} interaction. However, if S_d is maintained at its low value, closer to the LPed surface, the effect of V_{Ar} on $Ra_{\perp}$ decreases consistently. This behaviour was not explained by similar published studies, leaving the question unanswered. Therefore, further CFD investigations might be required in order to better understand

the reason behind this behaviour. Other 2-way interactions, reported for the sake of simplicity, do not provide meaningful insights into the relationship between process parameters.

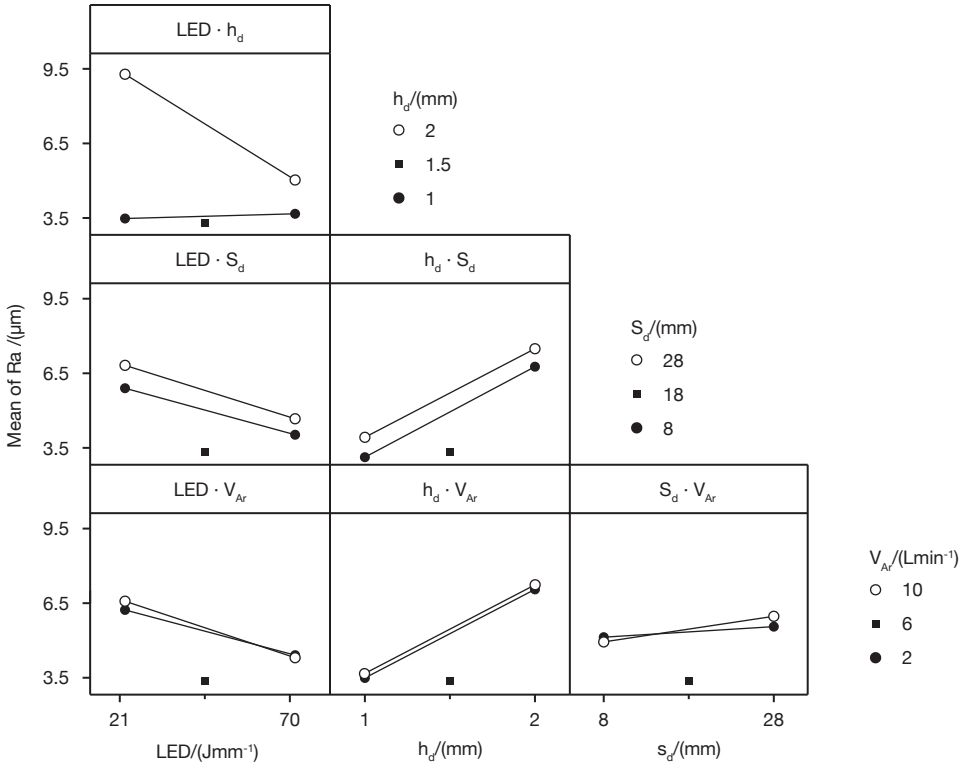

Fig. 3.11 Interaction plots for $Ra_{\perp}$.

The ANOVA conducted for $Ra_{\perp}$ also provides a regression equation, an empirical model that established a functional relationship between process parameters and $Ra_{\perp}$. Equation 3.2 displays the complete model provided by the ANOVA, including all linear terms and interactions. All process parameters must enter the model using the units of measure used throughout the study. Figure 3.12 displays the normal probability plot of the residuals of the proposed model, supporting its quality. The black dots represent the residuals of the model, whereas the solid line represents the ideal normal distribution. Since no clear deviation from normality can be identified, as supported by the p-value of 0.461, the hypothesis of the residuals being normally distributed cannot be rejected. This hypothesis is extremely meaningful since it suggests the lack of systemic biases that could have affected the distribution of the results.

$$\begin{aligned} Ra_{\perp} = &-2.85 + 0.0395 \cdot LED + 6.674 \cdot h_d - 0.1405 \cdot S_d + 0.306 \cdot V_{Ar} + \\ &-0.0563 \cdot LED \cdot h_d + 0.00533 \cdot LED \cdot S_d - 0.00411 \cdot LED \cdot V_{Ar} + \\ &+0.0773 \cdot h_d \cdot S_d - 0.247 \cdot h_d \cdot V_{Ar} - 0.0287 \cdot S_d \cdot V_{Ar} + \\ &-0.00292 \cdot LED \cdot h_d \cdot S_d + 0.00352 \cdot LED \cdot h_d \cdot V_{Ar} + \\ &+0.000415 \cdot LED \cdot S_d \cdot V_{Ar} + 0.02728 \cdot h_d \cdot S_d \cdot V_{Ar} + \\ &-0.000412 \cdot LED \cdot h_d \cdot S_d \cdot V_{Ar} \end{aligned} \tag{3.2}$$

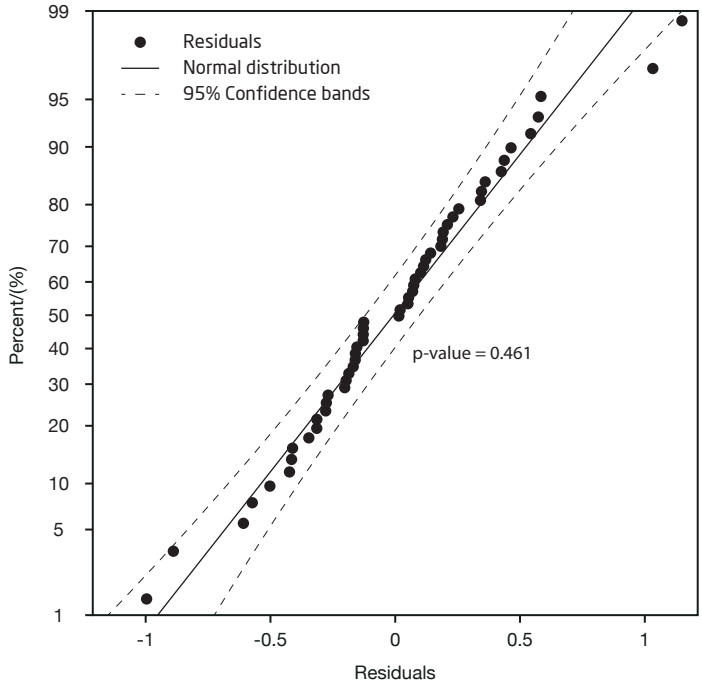

Fig. 3.12 Normal probability plot of the residuals of the $Ra_{\perp}$ model.

The complete model reported above accurately describes the behaviour of the acquired data. The ANOVA also provided useful coefficients to support the quality of the obtained model. At first, the standard deviation of the data S is computed. S is defined as the square root of the Adj MS of the error, as reported in Table 3.11. S is equal to 0.488 µm and is expressed in the same unit of measure as the response variable. S is significantly lower than the effects of the process parameters, suggesting a low stochastic dispersion of the investigated data. This first element already hinders a good model description of data dispersion. Moreover, the R^2, R^2_{adj} and R^2_{pred} were computed according to the mathematical definition reported in

Annex A. R^2 equal to 97.30% reassures that the proposed model is perfectly able to describe the dispersion of the data, leaving small room for stochastic effects. The R^2_{adj} equal to 96.09%, thus close to the R^2 value, ensures that no redundant process parameters were considered for investigation. Finally, the R^2_{pred} equal to 94.53% states an optimal capability of the model in forecasting the results of LP treatments inside the investigated experimental domain.

ANOVA for $Wa_{\perp}$

Although Ra certainly plays a major role in defining the surface quality of a sample, the average height of the W-profile, namely Wa, is still worth considering. Therefore, an ANOVA was performed on $Wa_{\perp}$ following the same rationale outlined in the previous section. Once more, the ANOVA was performed to understand which process parameters have an active role in the definition of the $Wa_{\perp}$ of LPed surfaces, and to start a possible quantification of the same influence.

Table 3.12 reports the results of the ANOVA for $Wa_{\perp}$. This time, only h_d was found to be significant at the confidence level of 95%. The S_d is significant at a 94.6% confidence level, which makes it worth considering nonetheless. V_{Ar} and LED are not statistically significant and therefore should have no influence on $Wa_{\perp}$. In addition, no significant interactions were highlighted and no contribution from the curvature terms was identified. At this stage, differences between the influence of process parameters on the response variable are already manifest. In particular, LED does not seem to influence the waviness response, while having a prominent role in the roughness one.

However, the biggest difference is the major role covered by the stochastic error, which alone covers more than two thirds of the variability of the data, η^2 equal to 0.675. The primary role covered by the stochastic error probably shadows other possible meaningful effects, reducing the descriptive ability of the model. A similar situation might have different possible explanations. The simplest one is that $Wa_{\perp}$ is intrinsically more scattered than $Ra_{\perp}$, being more influenced by random fluctuations. In this scenario, the three replicates performed might be insufficient to accurately detect the $Wa_{\perp}$ differences caused by the process parameters. A second possible explanation concerns the possibility of having reached a plateau-like area of $Wa_{\perp}$, where the changes in the process parameters have no real influence on the distribution of $Wa_{\perp}$ itself. This condition might be overcome by moving the experimentation out

Table 3.12 ANOVA for $Wa_{\perp}$.

		DF	Adj SS	Adj MS	F-value	p-value	η^2
Model		16	138.986	8.6866	1.09	0.403	0.482
	LED	1	0.080	0.080	0.01	0.921	<0.001
Linear	h_d	1	65.575	65.575	8.19	0.007	0.154
Terms	S_d	1	29.328	29.328	3.66	0.064	0.069
	V_{Ar}	1	12.680	12.680	1.58	0.216	0.030
	LED·h_d	1	10.368	10.368	1.30	0.263	0.024
	LED·S_d	1	0.586	0.586	0.07	0.788	0.001
2-Way	LED·V_{Ar}	1	8.244	8.244	1.03	0.317	0.019
Interactions	$h_d \cdot S_d$	1	0.001	0.001	<0.01	0.989	<0.001
	$h_d \cdot V_{Ar}$	1	1.210	1.210	0.15	0.700	0.003
	$S_d \cdot V_{Ar}$	1	3.614	3.614	0.45	0.506	0.008
	LED·$h_d \cdot S_d$	1	0.512	0.512	0.06	0.802	0.001
3-Way	LED·$h_d \cdot V_{Ar}$	1	0.365	0.365	0.05	0.832	0.001
Interactions	LED·$S_d \cdot V_{Ar}$	1	0.569	0.569	0.07	0.791	0.001
	$h_d \cdot S_d \cdot V_{Ar}$	1	2.237	2.237	0.28	0.891	<0.001
4-way Interaction	LED·$h_d \cdot S_d \cdot V_{Ar}$	1	0.154	0.154	0.02	0.891	<0.001
Curvature		1	3.462	3.462	0.43	0.515	0.008
Error		36	288.126	8.003			0.675
Total		52	427.113				

of the currently investigated domain. At the moment, it is not possible to understand which was the cause of the high stochastic contribution to data dispersion. Further experimentation may yield insights that are currently obscured.

Figure 3.13 shows the main effect plots of the process parameters for $Wa_{\perp}$. Low values of $Wa_{\perp}$ are observed for low values of h_d, the only process parameter that is significant at a confidence level above 95%. This trend is similar to the one highlighted in Figure 3.10 for $Ra_{\perp}$. The second process parameter of interest is the S_d, which is almost significant at a 95% confidence level. Contrary to what was highlighted for $Ra_{\perp}$, the higher S_d level implies lower $Wa_{\perp}$ values. Although this result may seem to contradict the previous discussion, it does not. Reducing the value of surface roughness, *Ra* above all R-parameters, requires the use of high energy density during LP treatments. Therefore, the higher value of the laser spot, consequence of the higher value of S_d, worsen the situation by decreasing

the energy density of the LP treatment. As for waviness reduction, it has already been proven in literature that larger laser spot diameters can be beneficial. Larger laser beam diameters led to lower Wa values in both the studies of Bruzzo et al. [110] and Meylan, Calderon, and Wasmer [136]. In addition, Temmler et al. [137] created higher surface structures when using larger laser beam diameters in surface structuring processes. Although their results belong to a different process, they can be generalised to support the adequacy of larger beam diameters in reducing surface Wa.

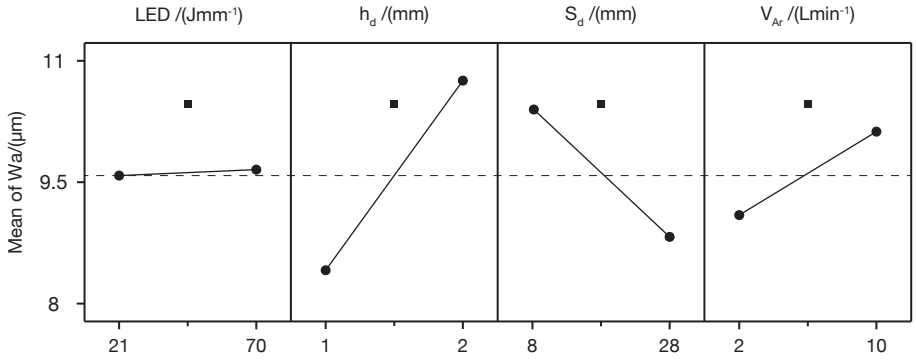

Fig. 3.13 Main effect plots for $Wa_{\perp}$

Figure 3.14 displays the 2-way interaction plot for $Wa_{\perp}$. Although the ANOVA did not reveal any significant interactions, some valuable inside were given nonetheless. The interaction between LED and h_d was the closest to being significant, with a p-value of 0.262 (still very far from the 0.05 threshold). LED $\cdot$ h_d suggest a possible interaction between the two process parameters, reducing $Wa_{\perp}$ at low levels of h_d and high levels of LED, i.e. for high energy conveyed. These results might suggest the need for higher energy to achieved a lower $Wa_{\perp}$ after remelting, partially supporting the previous hypothesis on the selected window of process parameters. The second interaction worth considering is the LED $\cdot$ V_{Ar} interaction. In particular, better results were obtained at low V_{Ar} levels when using high LED. More in general, in all 2-way interactions that considered V_{Ar}, better $Wa_{\perp}$ were obtained for low V_{Ar} values. This further supports the previous claims about the preferability of minimal V_{Ar} in LP treatments.

The ANOVA performed on $Wa_{\perp}$ also provided an empirical model relating $Wa_{\perp}$ to the investigated process parameters. Equation 3.3 reports $Wa_{\perp}$ as a function of the process parameters. Although the model is reported for the sake of completeness, its utility is extremely limited at this stage. The strong influence of stochastic

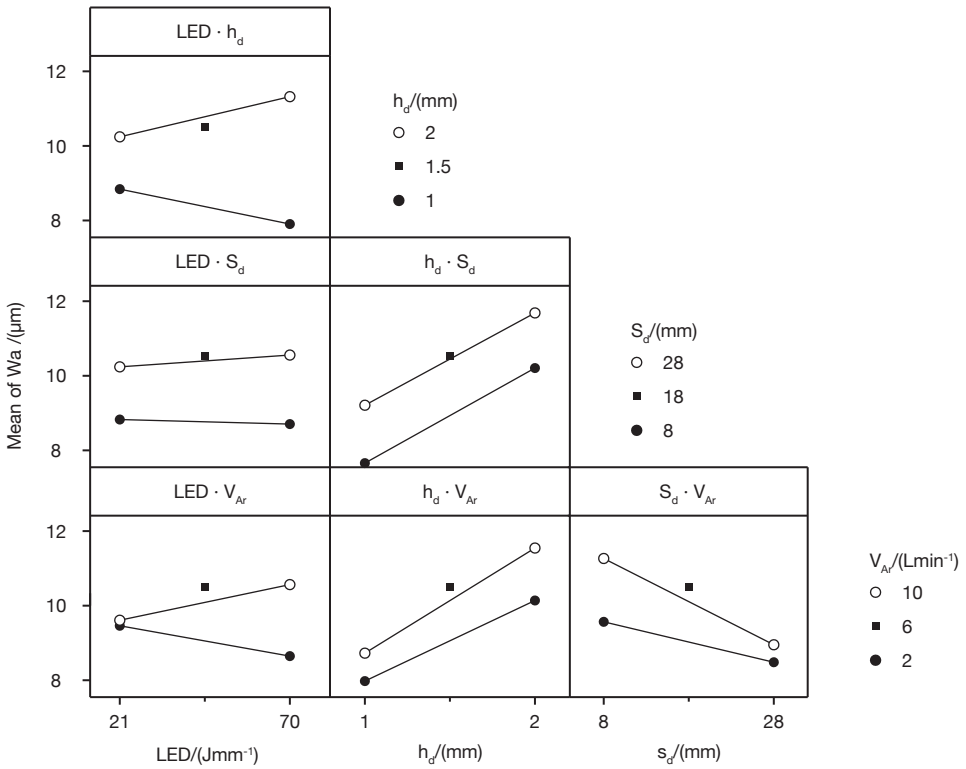

Fig. 3.14 Interaction plots for $Wa_{\perp}$.

phenomena, quantified by a standard deviation of 2.83 µm, led to limited description capabilities of the model. The R^2 coefficient equal to 32.54% perfectly summaries the situation, representing the small role of the process parameters in the distribution of the data. Values of R^2_{adj} and R^2_{pred} even lower than R^2 overt the inability of the model to describe the effect of the process parameters on $Wa_{\perp}$.

$$\begin{aligned} Wa_{\perp} = 8.57 - 0.069 \cdot LED + 1.21 \cdot h_d + 0.042 \cdot S_d + 0.197 \cdot V_{Ar} + \\ + 0.0288 \cdot LED \cdot h_d + 0.00044 \cdot LED \cdot S_d + 0.0009 \cdot LED \cdot V_{Ar} + \\ - 0.059 \cdot h_d \cdot S_d - 0.162 \cdot h_d \cdot V_{Ar} - 0.0259 \cdot S_d \cdot V_{Ar} + \\ - 0.00015 \cdot LED \cdot h_d \cdot S_d + 0.0029 \cdot LED \cdot h_d \cdot V_{Ar} + \\ + 0.00006 \cdot LED \cdot S_d \cdot V_{Ar} + 0.0160 \cdot h_d \cdot S_d \cdot V_{Ar} + \\ - 0.000115 \cdot LED \cdot h_d \cdot S_d \cdot V_{Ar} + 0.87 \cdot CtPt \end{aligned} \tag{3.3}$$

Finally, Figure 3.15 shows the normal probability plot of the residuals of the $Wa_{\perp}$ model obtained by the ANOVA. In this case, the hypothesis of normal distribution of the data was rejected, p-value of the distribution lover than 0.05. However, the result depends solely upon a single residual, the one in the upper right corner of the graph. The simple removal of this single data resulted in a p-value of 0.158, suggesting a normal data distribution. Therefore, the claim of data non-normality was not pursued, stating the absence of systematic biases also for $Wa_{\perp}$.

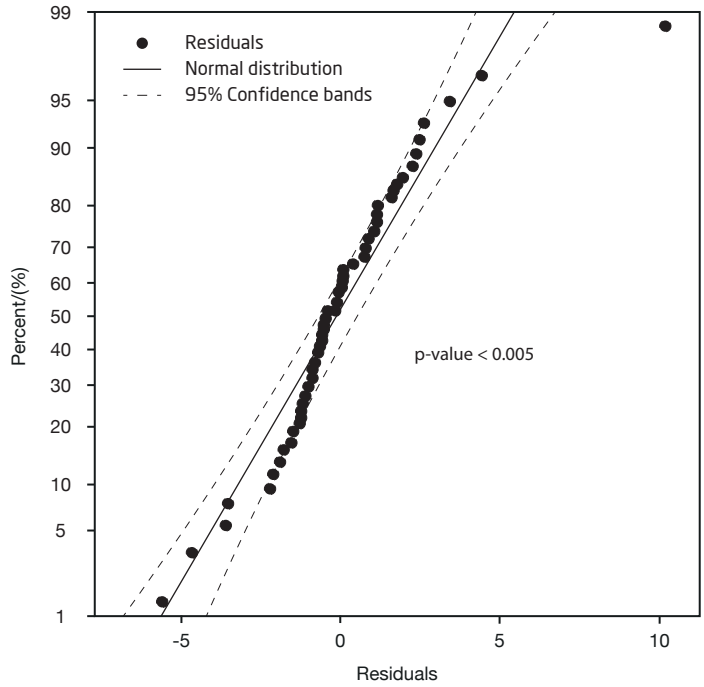

Fig. 3.15 Normal probability plot of the residuals of the $Wa_{\perp}$ model.

3.6 Defect Analysis

Laser polished surfaces experienced an abrupt improvement in surface quality compared to the as-built condition. However, some recurring defects were highlighted on the same LPed surfaces. This section covers the three main defects observed: the oxidation of the surface during the treatment, the appearance of cracks undermining the integrity of the surface, and what seemed to be spatter of molten material on adjacent tracks.

3.6.1 Surface Oxidation

A clear distinction between two clusters of LPed surfaces emerged throughout the course of the campaign. Half of the LPed surfaces showed a bright surface with no visible oxidation. On the other hand, the other half of the LPed surfaces were consistently oxidised. Figure 3.16 displays the evident differences between the two clusters. The two samples selected for this comparison where treated with the same high level of LED, same low levels of h_d and V_{Ar}, but different S_d. The same pattern was also observed on the other LP treatments composing the experimental campaign. Therefore, the S_d was identified as the only cause of oxidation. In fact, when LP treatments were performed using the high level of S_d, and regardless of the considered level of V_{Ar}, the surface oxidised inevitably.

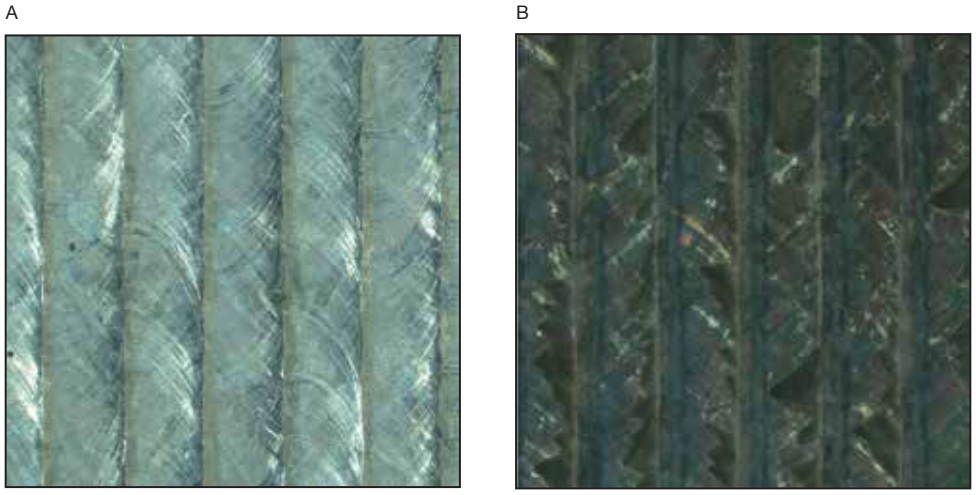

Fig. 3.16 Comparison between unoxidised and oxidised LPed surfaces; A) Treatment N. 9: LED = 70 J mm^{-1}, h_d = 1 mm, S_d = 8 mm, V_{Ar} = 2 L min^{-1}; B) Treatment N. 11: LED = 70 J mm^{-1}, h_d = 1 mm, S_d = 28 mm, V_{Ar} = 2 L min^{-1}.

3.6.2 Cracks and Surface Irregularities

In addition to surface oxidation, cracks and molten metal spillage were identified by visual inspection alone, as in Figure 3.17. Unlike oxidation, which could only be described qualitatively, these defects were suitable for quantitative analysis. Therefore, defects were identified and their total area computed for each LPed sample. The total defective area was the response variable in an ANOVA to understand which process parameter was responsible for their appearance. S_d was the only process

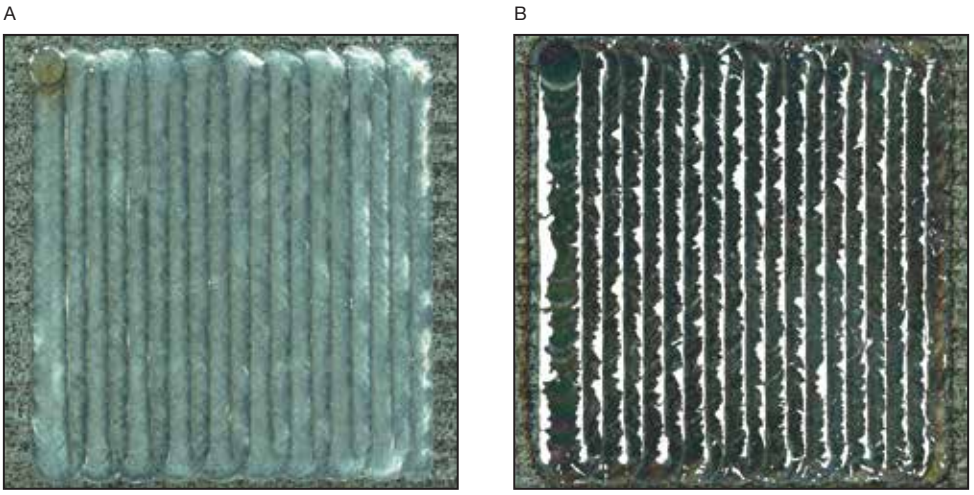

Fig. 3.17 Defect quantification; ; A) Treatment N. 9: LED = 70 J mm^{-1}, h_d = 1 mm, S_d = 8 mm, V_{Ar} = 2 L min^{-1}; B) Treatment N. 11: LED = 70 J mm^{-1}, h_d = 1 mm, S_d = 28 mm, V_{Ar} = 2 L min^{-1}.

parameter found to be significant by the ANOVA, p-value lower than 0.001, and explaining alone 75% of the overall variability. The other terms found significant were the interactions to which S_d belonged to.

Therefore, The high S_d level was responsible for both higher defect concentration and surface oxidation, potentially reducing the fatigue life of the sample rather than increasing it by reducing its roughness.

3.7 Conclusions

In conclusion, Chapter 3 presented the exploratory experimental campaign carried out. The main objective of the exploratory campaign was the definition of the process parameters having a significant influence on the quality of the treated surface. The primary findings of the experimental campaign were here summarised for the reader:

- linear energy density, hatching distance and stand-off distance were identified as significant factors, having a clear influence on Ra and Wa;
- high values of linear energy density and low values of hatching distance provided the best surface quality, paving the way for further optimisation campaigns;

- the increase of the stand-off distance, together with the consequent defocusing of the laser beam, had a strong detrimental influence on the Ra value and caused the occurrence of defects on the surfaces of LPed samples. However, the increased stand-off distance resulted in a consistent reduction of Wa, due to the enlarged laser spot diameter;

- although the argon flow rate played a minor role in some of the interactions with other process parameters, it did not have a significant role for Ra determination. this result was far from being unhelpful as it ensured that the shielding gas flow rate could be adjusted as required. A low shielding gas flow rate seems to ensure a lower Ra value, thereby reducing the cost of the experimentation at the same time. On the contrary, a high value of the shielding gas flow rate may be employed to prevent any form of oxidation or contamination of the melt pool when necessary.

Chapter 4

Optimisation Campaign

The present chapter covers the activities that followed the initial exploratory campaign. The exploratory campaign established the significance of LED and h_d over the roughness of LPed surfaces. Experimental evidence suggested that higher LED and lower h_d may result in more desirable surface quality, due to the higher thermal energy transferred to the material during the polishing treatment. On the other hand, defocusing the laser beam by increasing S_d was found to be largely detrimental for the surface quality. High values of S_d resulted in higher Ra and in the appearance of different types of defects on the LPed surfaces. In addition, V_{Ar} did not play a significant role in Ra definition, suggesting that it could be adjusted according to the need. These findings were implemented in the subsequent procedure, aimed at inquiring for an Ra minimum. Following the identification of the minimum area, a final optimisation campaign was conducted. The objective of the optimisation campaign was to accurately describe the functional relationship between process parameters and the response variable. The optimisation campaign provided an empirical model that might be useful for predicting the results of future LP treatments, thereby reducing the need for additional experimentation, and saving both resources and time. In detail, Section 4.1 describes the gradient method used to locate the possible minimum of Ra. Results are reported in terms of pictures captured for visual inspections and of quantitative data acquired using the roughness tester. Section 4.2 is devoted to the proper optimisation campaign. At first, the rationale behind the selection of the experimental plan is presented. Subsequently, the results of the experimental campaign are extensively discussed and a conclusive descriptive model

is proposed. Finally, Section 4.3 presents the optimal set of parameters, certifying the usefulness of the empirical model obtained, and Section 4.4 draws the conclusions on the whole experimental campaign.

4.1 Process Improvement

Most experimental activities are designed to identify a working condition that ensures an optimal behaviour of the system under examination. When little prior knowledge on the topic is available, several parameters are typically considered at the same time, trying not to overlook any important ones. The definition of an accurate functional relationship between the response variable and the process parameters usually requires the use of at least three levels per investigate factor. In fact, three levels are the minimum number required to describe the nonlinear behaviours of each factor, and therefore to identify the optimal working condition of the system. It is straightforward that conducting an experimental campaign with a large number of parameters, and at least three levels per parameter, would result in an unreasonable number of experimental trials. The resources required for a similar experimental campaign would be prohibitive in terms of raw materials, equipment utilisation and amount of data.

Therefore, the planning of experimental activities should be conducted in a systematic manner, comprising several consecutive steps. At first, active factors should be screened from the considered ones. Once the number of investigated factors has been consistently reduced, a second and equally important phase must take place, i.e. the search for a possible region of optimum. Although the search for the optimum region is a crucial phase for any experimental activity, it is often overlooked by the same experimenters. At the beginning of the exploratory phase, there is no evidence that the current region of interest and the region of the optimum overlap. Consequently, limiting the entire discussion to the same initial region of interest may be highly detrimental to the results of the experimentation, as illustrated in Figure 4.1. Nevertheless, all previous examples available in the literature, as presented in Section 2.5, failed to consider this fundamental aspect of experimental planning, thereby providing no illustrative examples.

In order to provide a mathematical structure to the search problem, the behaviour of the system is approximated by the empirical model computed during the ANOVA.

Consequently, the problem of finding the region of optimal response of the system can be formulated as the optimisation problem of a mathematical function. Several algorithms can be used to solve the optimisation yet introduced. The gradient method and the Newton-Raphson method are two of the most commonly used due to their implementation simplicity.

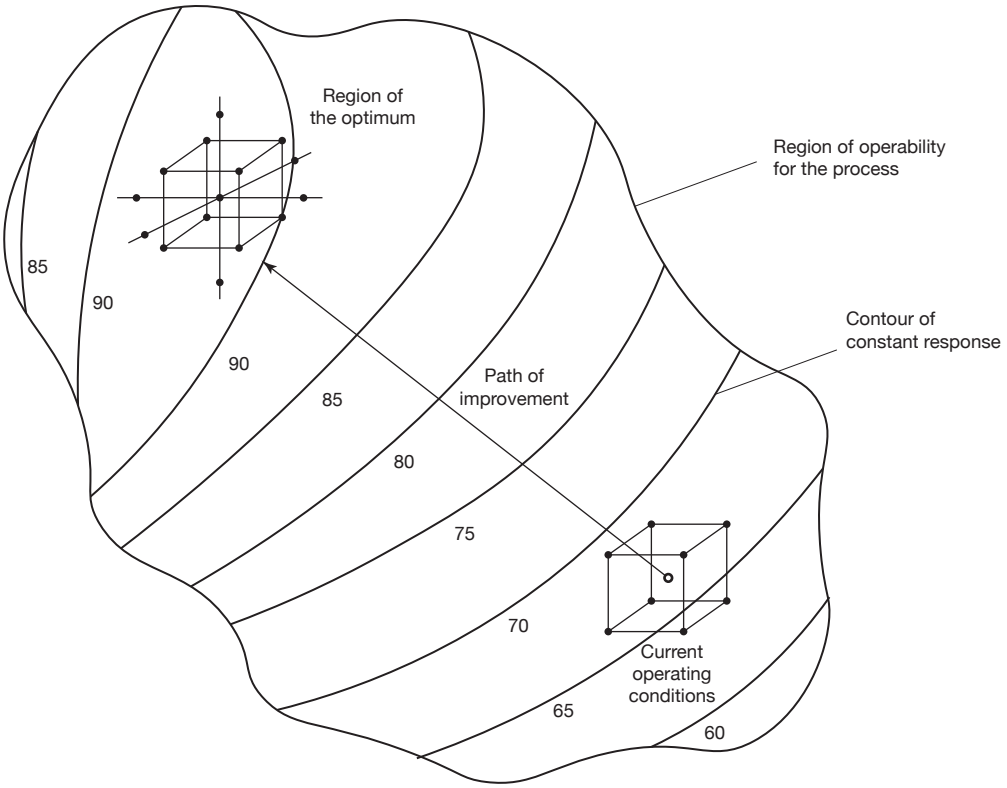

Fig. 4.1 Sequential nature of experimental activities. Adapted from [123].

4.1.1 Steepest Descent Method

The steepest descent method, or gradient descent method, is an optimisation algorithm that locally approximates the behaviour of the system with a first-order model, neglecting any non-linear contribution. From there, the fastest decay direction can be defined by simply computing the gradient of the model. Since the reference model is a linear one, the direction computed is unique and assumed constant also outside the previously investigated region of interest. Subsequently, the value of the response variable is regularly checked along the same direction. As-soon-as the monotony of the response value changes, the procedure can be stopped and

later optimisation campaigns can be conducted in the newly identified region. In its simplicity, the steepest descent method provides a powerful instrument for the identification of a minimum (or maximum) of a multi-dimensional function. However, some preliminary precautions should be considered.

The steepest descent method approximates the system with a first-order model, setting aside any nonlinear contributions during the definition of the path direction. This hypothesis must be carefully checked in order to avoid overlooking significant effects. In general, if the first guess proves to be far from the optimal region, the contribution of non-linear terms could be negligible and the linearity approximation considered reasonable. Most exploratory campaigns use 2^k experimental plans, either full or fractional, which do not permit the verification of the linearity hypothesis. In this situation, the use of the steepest descent algorithm should be carefully considered, being aware of the related risks. A simple precaution to ascertain the linearity hypothesis is the introduction of one or more central points into the experimental plan already at its exploratory stage.

Once the model is assessed eligible for the steepest descent method, the direction of motion is defined by the same coefficients of the model (regression equation) that were previously computed. Aiming at a minimum of the function, the coefficient of each factor should be considered with the same absolute value but with the sign being opposite to that of the model. Conversely, the same sign should be maintained when aiming at a function global maximum. Alongside the direction, the angular uncertainty should be computed to complete the information provided. Equation 4.1 provides the mathematical formulation of the angular uncertainty of the path of steepest descent [138].

$$\theta = \sin^{-1} \sqrt{\frac{(k-1) \cdot s_b^2 \cdot F_{\alpha,k-1,\nu}}{\sum_{i=1}^{k} b_i}} \tag{4.1}$$

Where k is the number or variables considered in the steepest descent algorithm, b_i are the coefficients of the variables used to define the direction of the path, and s_b^2 is the common variance associated with the coefficients b_i. Finally, $F_{\alpha,k-1,\nu}$ is the inverse F probability function computed at an α significance level, with $k-1$ degrees of freedom at the numerator and ν degrees of freedom at the denominator. The coefficient ν equals the degrees of freedom of the error for the computation of

the path. The mathematical definition of the angular uncertainty does not impose any limitation on the maximum number of dimensions that can be considered, as for the path of steepest descent itself. In the simplest case of two and three dimensions, the angular uncertainty can be graphically represented as a planar angle and solid angle respectively. However, if more than three dimensions are considered simultaneously, the hyper-angle maintains its mathematical definition and meaning, but looses its graphical representation. Similar effort should be dedicated to accurately define the step used to space the experimental trials along the steepest descent path. An excessively small step could result in massive resource consumption without the guarantee of convergence of the method. Conversely, a coarse sampling along the steepest descent path may fail to identify the optimal region and could eventually result in divergence of the method. Finally, replications of each defined step should be also considered to reduce the influence of nuisance factors and improve the estimate of the error.

4.1.2 Results and Discussions

Section 3.5 reported the complete model computed during the ANOVA for $Ra_{\perp}$. Although the model provided for an accurate description of the distribution of the data, it also considered all interactions between process parameters, making it difficult to use for the steepest descent algorithm. Therefore, a linear model was obtained by simply performing an ANOVA on $Ra_{\perp}$ limited to first order terms only. Equation 4.2 refers to the aforementioned linear model. The linear model provided a leaner equation that described the system at the cost of a lower accuracy, $R^2 = 64.85\%$. However, the results were deemed satisfactory for the intended purpose.

Equation 4.2 provided an $Ra_{\perp}$ hyperplane in a four-dimensional space, as it considered all four process parameters investigated. However, V_{Ar} was found to be non statistically significant, while S_d was found to be significant but detrimental for $Ra_{\perp}$. Therefore, both V_{Ar} and S_d were maintained at their low level during this phase, with only the effects of LED and h_d being investigated. This approach allowed a graphical representation of the level curves of $Ra_{\perp}$ as a function of LED and h_d, as well as the graphical representation of the steepest descent path. In this scenario, the steepest descent path can be easily defined considering the normal direction to the level curves of $Ra_{\perp}$.

$$Ra_{\perp} = 1.259 - 0.0404 \cdot LED + 3.550 \cdot h_d + 0.0374 \cdot S_d + 0.0184 \cdot V_{Ar} \qquad (4.2)$$

Being the direction defined, the angular uncertainty was computed using Equation 4.1. Having considered only two process parameters, K was set equal to two. The sum of the squared coefficient of the two parameters was equal to 4.113, and their common variance s_b^2 was equal to 0.203. Finally, a significance level α of 0.05 was selected, and the F-distribution was defined by 1 degree of freedom at the numerator and 47 degree of freedom at the denominator (degree of freedom of the error). The outcome of Equation 4.1 was $\theta = 26.359°$, deemed an acceptable result and providing good accuracy of the drawn path. No comparisons with other published results were possible as no previous records about angular uncertainty computation in steepest descent methods were available in literature.

Furthermore, the step size used to sample the $Ra_{\perp}$ along the steepest descent path was selected. Steps of 0.25 mm were opted for h_d, as they were considered to be sufficiently close to provide a detailed description of the $Ra_{\perp}$ trend without requiring excessive resources. The value of the LED steps, equal to $7\,\mathrm{J\,mm^{-1}}$, was therefore uniquely defined, having already set the direction of the path. Four steps were considered, given that the region of operability was inferiorly constrained by a minimum value of h_d. The hatching distance h_d represents the distance between two consecutive tracks, being ideally constrained to positive values. In addition, the minimum h_d value considered eligible for LP treatment was set to 0.10 mm, as lower values would result in excessively long treatments.

Figure 4.2 displays a comprehensive overview of the information discussed in the present section. In the upper half of the picture, the curve levels of the linear model for Ra are represented. This choice enhanced an immediate comprehension of the relationship between the linear model and the steepest descent path. The path itself is reported in the lower half of the picture. The four steps are highlighted on the path, with the first step being on the edge of the previously investigate region of interest. The angle representing the uncertainty of the path direction was superimposed onto the graph, clearly demonstrating its geometrical meaning. The angle originates from the centre of the previously investigated region of interest, as the path itself.

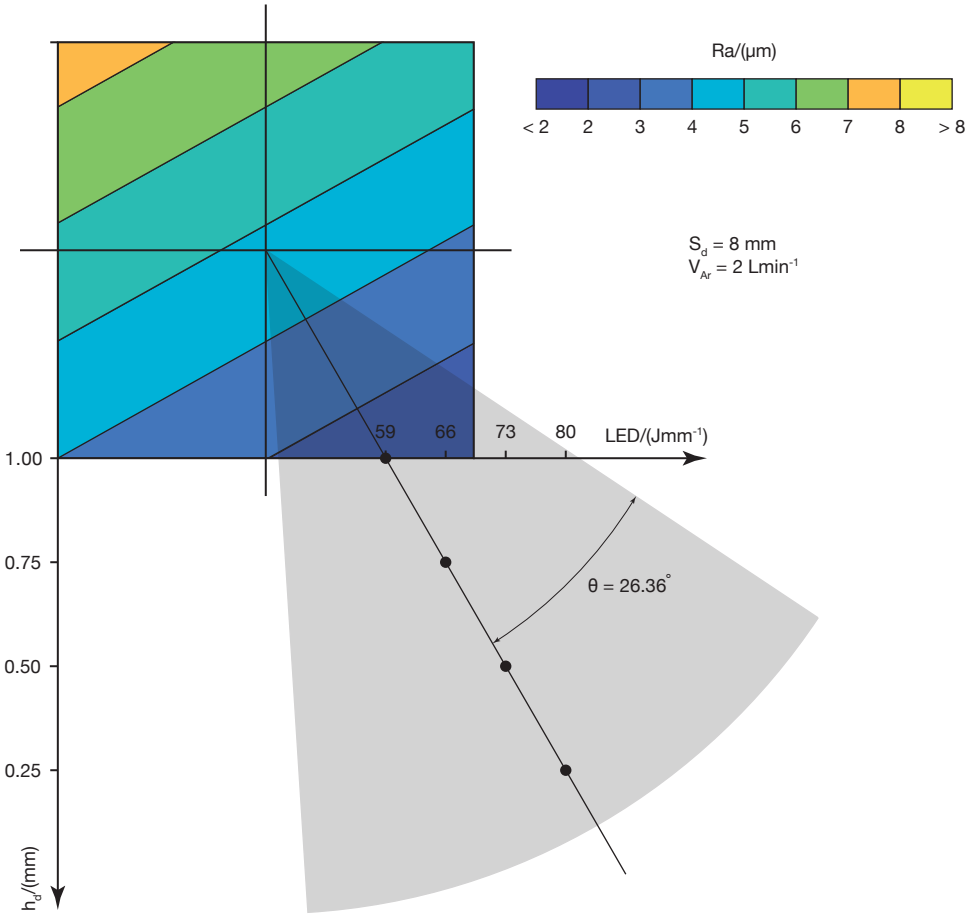

Fig. 4.2 Steepest descent path considering LED and h_d. V_{Ar} equal to 2 L/min and S_d equal to 8 mm.

Figure 4.3 presents the pictures of the LPed surfaces finished during the steepest descent algorithm. Upon initial observation, it can be seen that the samples exhibit an increasing density of patterning as the steepest descent algorithm progresses. This phenomenon can be attributed to the utilisation of a smaller h_d value during the steepest descent algorithm. Additionally, the sample finished during the final step of the steepest descent exhibits a notable degree of oxidation, which must be taken into account during the subsequent quantitative measurements.

Figure 4.4 illustrates the numerical outcomes of the steepest descent algorithm. Three replications of each step were carried out, and the results were aggregated in terms of means and standard deviations. The error bars of the graph are equal to twice the computed standard deviation, enhancing a clear comparison between confidence intervals of different mean values at a confidence level around 95%. Ra

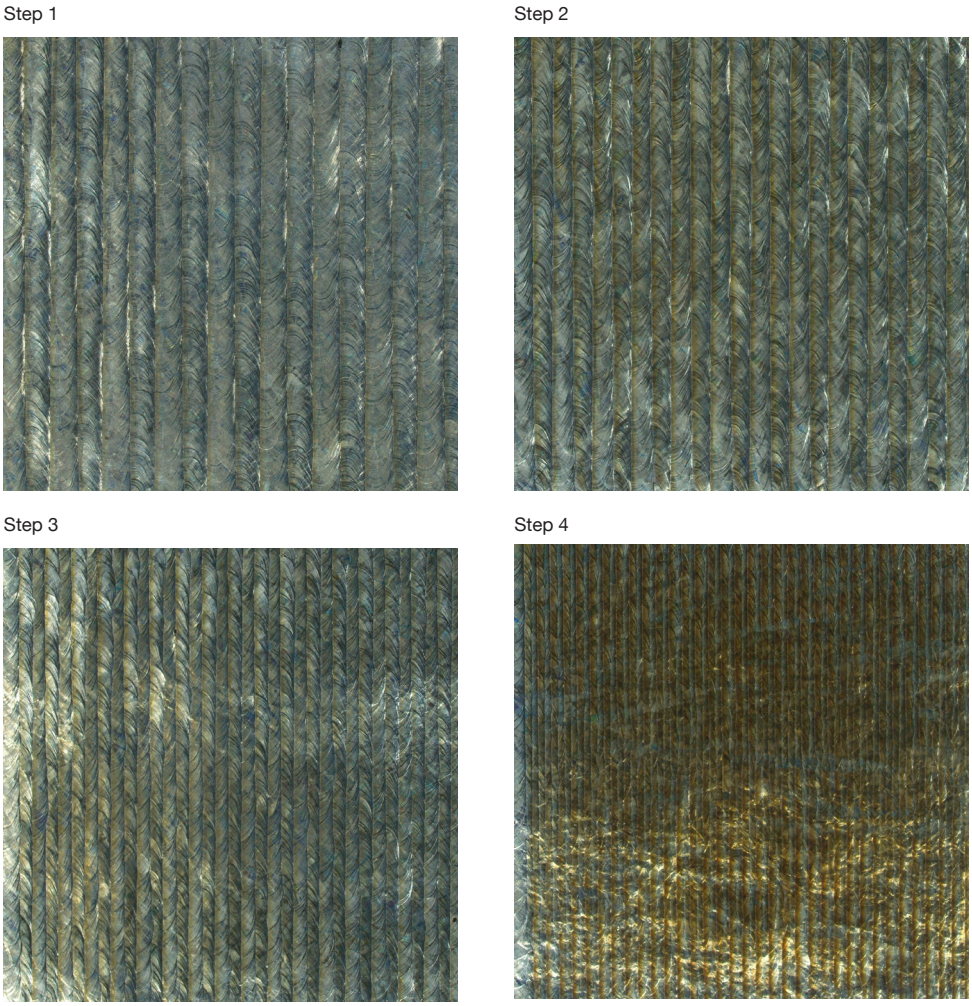

Fig. 4.3 LPed surfaces resulting from the steepest descent algorithm.

results were used to take actions and halt the steepest descent algorithm when a possible optimal region was identified. In addition, other R and W-parameters were measured and reported to provide a holistic description of the transformations that the samples underwent. Ra exhibited a monotonic trend, with a gradual decrease over the four steps. However, the amount of the Ra improvement decreased at each step, dropping below 10% at the fourth step. At that point, the Ra improvement was comparable with the measured standard deviation, suggesting that a possible region of optimum was reached. In contrast, Rz did not improved significantly after the first step, assessing around 11 µm. Therefore, and higher thermal energy level facilitated a more uniform redistribution of the molten material, resulting a smoother profile on average. However, although the profile was averagely smoother,

consistent peaks and valleys were still observed. Finally, Rsk and Rku remained almost constant along the steepest descent path, suggesting that the higher energy conveyed during LP treatments had no significant influence on profile symmetry and distribution, as can be also observed in Figure 4.5. The data provided by Wa and Wz were not deemed to be of sufficient utility. Wa remained within the same range of (8.5 ± 2) µm, comparable to the the best values measured during the exploratory campaign. Similarly, also Wz resulted in values comparable to the exploratory campaign. On the one hand this results can hinder the hope for further improving surface waviness of LPed samples. On the other hand, it appears that higher energies did not result in increased waviness of the sample, that could have counterbalanced eventual roughness improvements observed.

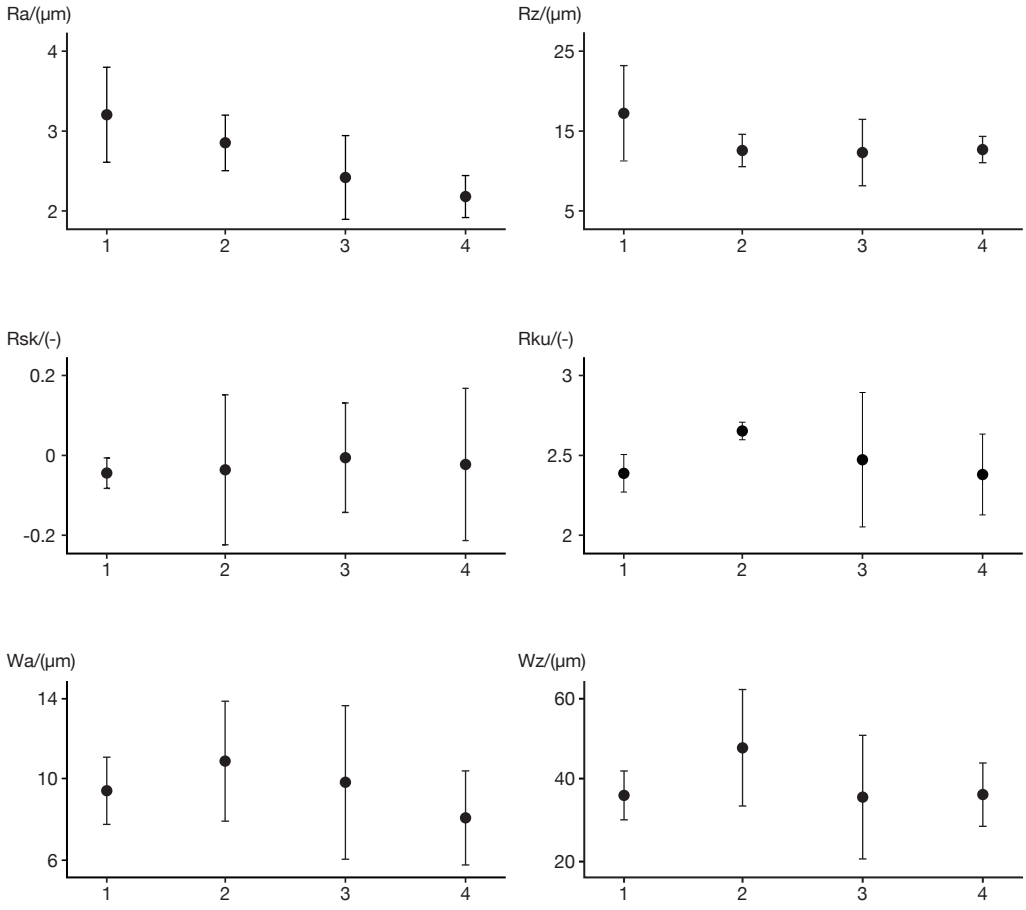

Fig. 4.4 Results of the steepest descent algorithm in terms of Ra, Rz, Rsk, Rku, Wa and Wz.

In conclusion, the impossibility to indefinitely decrease h_d, together with increasingly smaller Ra improvements, suggested the possibility of halting the steepest

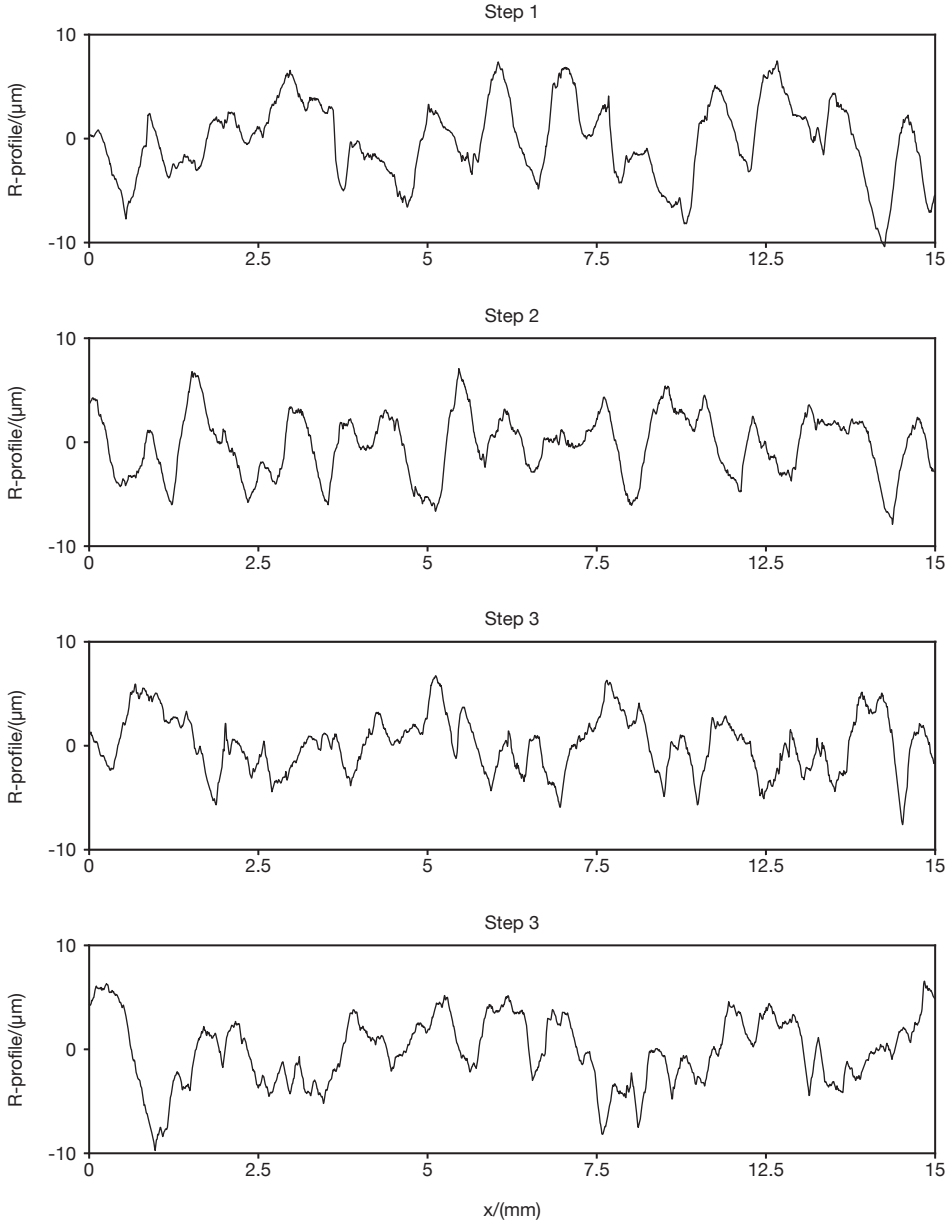

Fig. 4.5 R-profiles acquired during the steepest descent algorithm.

descent method at its fourth step. Therefore, the pair of LED = 80 J mm^{-1} and h_d = 0.25 mm was selected as the central value for a further optimisation campaign, aiming at computing a model to accurately describe the linear and non-linear effects of LED and h_d.

4.2 Optimisation Campaign

The culminating moment of any experimental activity is the definition of an optimal working condition, granting the best answer from the studied system. Optimisation campaigns fulfil this role, with the aim of providing an accurate empirical model that mathematically describes the behaviour of the system in the region of interest. In addition, the mathematical description of the system also provides the possibility of graphically representing its response, especially for two and three dimensions problems. Optimisation campaigns usually require previous phases, including screening studies and optimal regions research, as it was done in the present investigation.

In the present section LED and h_d were investigated once more to define the functional relationship between them and R and W-parameters. The present section is articulated in three subsections. In the first one the discussion focuses on the definition of the most suitable experimental design, and on the definition of the levels of the factors. Results and discussions are then reported in the second subsection. With regard to the exploratory phase, results are extensively discussed for Ra and Wa, considered the most significant out of the measured parameters. Once the optimal set of parameters was defined, a final experimental run was carried out to test the optimal parameter set. The surface of the sample treated with the optimal parameter set was then comprehensively characterised and compared to the initial as-built condition. Finally, the third subsection describes the LP of the lateral surface of a DEDed sample with the same optimal set of process parameters.

4.2.1 Experiment Design

It is of paramount attention that experimental plans used for optimisation campaigns receive the requisite attention during their design phase. Experimental plans designed for optimisation campaign must ensure a clear description of linear effects, interactions and quadratic effects for each factor distinctly, therefore being able to fit

second-order models. In addition, optimisation plans must provide a good variance distribution throughout the region of interest, and an estimate of both stochastic error and lack of fit of the model. Therefore, although 2^k experimental plans are of primary importance during exploratory campaigns, they are not suitable for optimisation campaigns. Even considering central points, 2^k experimental plans can only provide an approximate indication of second order effects. In order to achieve a clear description of second-order effects, it is necessary to consider at least three levels for each factor. Several designs have been proposed to provide a response surface for the investigated variable. In this subsection, three possible experimental designs to fit a second order response surface are reported, to provide the reader with sufficient background information to understand the rationale behind the final choice made.

The Central Composite Design (CCD)

The Central Composite Design (CCD) is one of the most widely used experimental plans for fitting second-order response surfaces [138]. A CCD can be easily obtained by adding additional axial runs and central points to a 2^k design. Therefore, the possibility of working in an additive manner is one of its major leverages. A 2^k experiment can be performed in a first moment, and later expanded with central points and axial runs aiming at a description of second-order effects. The positioning of the axial runs, namely the distance α between the axial runs and the centre of the design, is of dramatic importance as it can affect the rotatability of the design itself. A design is considered rotatable if the precision of the prediction is solely dependent on the distance from the centre of the design, without any influence from the direction selected. Further insight into the concept of rotatability and the means of assessing it, can be found in the Annex A.3. Two common solutions can be adopted for CCDs, according to the shape of the investigated domain, as shown in Figure 4.6.

- $\alpha = \sqrt{k}$ is probably the most popular option, which results in a spherical region of interest. This means that all factorial and axial run are equidistant from the centre of the region of interest. In this case, the design is almost rotatable, therefore ensuring an almost uniform variance distribution of the response in the spherical region of interest.

- $\alpha = k$ is a less frequently employed option that results in a cuboidal region of interest. The lower usage of the second option can be attributed to the loss of rotatability of the resulting design. However, it can still be beneficial when the investigated phenomena naturally present a cuboidal region of interest.

Regardless from the selected value of α, CCD designs should always include a certain number of central runs, to enhance their stability. A value between three and five central runs is typically sufficient for the scope [138].

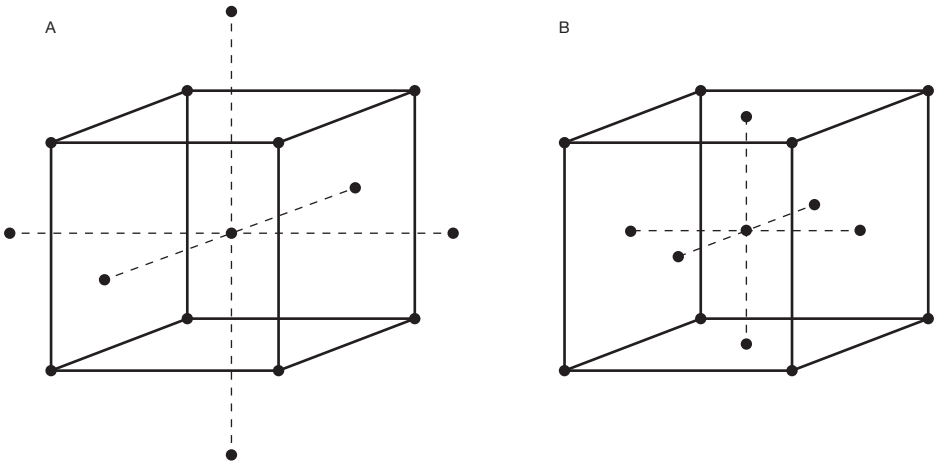

Fig. 4.6 CCD for k = 3; A) Spherical region of interest; B) Cuboidal region of interest. Adapted from [138].

The Box-Behnken Design (BBD)

The Box-Benhken (BBD) design was first introduced in the 60s [139] to provide a three-level design for fitting second order response surfaces. The BBD belongs to the class of balanced incomplete block designs, meaning that the complete experimental plan can be obtained by the modular combination of smaller design plans. Without going too deep in the construction of BBD designs, it is sufficient to say that these designs have grown in popularity since they provide three equally spaced levels, can be more resource efficient than CCD, and are always near rotatable, being exactly rotatable in the cases of $k = 4$ and $k = 7$. Figure 4.7 depicts the distribution of the experimental runs in a BBD for $k = 3$. It is straightforward to notice that the BBD provides a good coverage of the core of the interest region, without placing any point at the vertices of the cube. This feature of BBD must be carefully considered when implementing it.

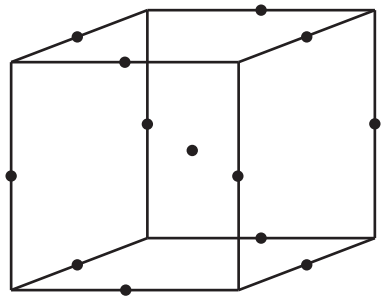

Fig. 4.7 Box-Behnken Design for k = 3. Adapted from [138].

3^k Factorial Designs

The last example of experimental plan here outlined is the 3^k factorial design, as in Figure 4.8. This option is the least commonly used in industrial activity, primarily due to the large number of experimental trials required for high values of k [140]. In addition, 3^k factorial designs lack of rotatability, which might be a limitation in certain cases. Figure 4.9 shows the Scaled Prediction Variance (SPV) surface for a 3^2 factorial design. The SPV is an index of the variance of the response variable as a function of the spatial distribution of the factorial points. A more detailed mathematical discussion about SPV can be found in the Annex A.3. Therefore, rotatable designs have symmetrical SPV, whose value only depends on the distance from the centre of the design and does not depend on the angular direction. The curve levels reported in Figure 4.9 are clearly indicative of a strong dependency between the variance of the response variable and the angular position considered, thereby supporting the statement of the non-rotatability of the 3^2 factorial design.

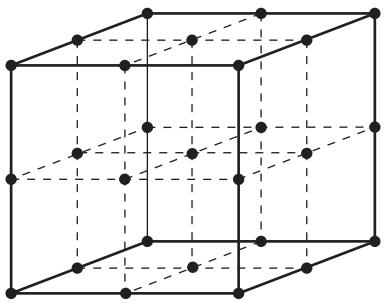

Fig. 4.8 3^k factorial design for k = 3.

The 3^k factorial design also offers significant advantages. Firstly, 3^k designs provide an immediate understanding of nonlinear effects, being easily manageable even by technical figures without a strong statistical background. In addition, 3^k

designs ensures a perfect coverage of cuboidal interest regions, more uniformly than CCD and BBD. Finally, the 3^2 design, thus limited for k = 2, is as resource efficient as the CCD design, requiring the same number of proofs. It should be noted, however, that the BBD does not exist for k = 2.

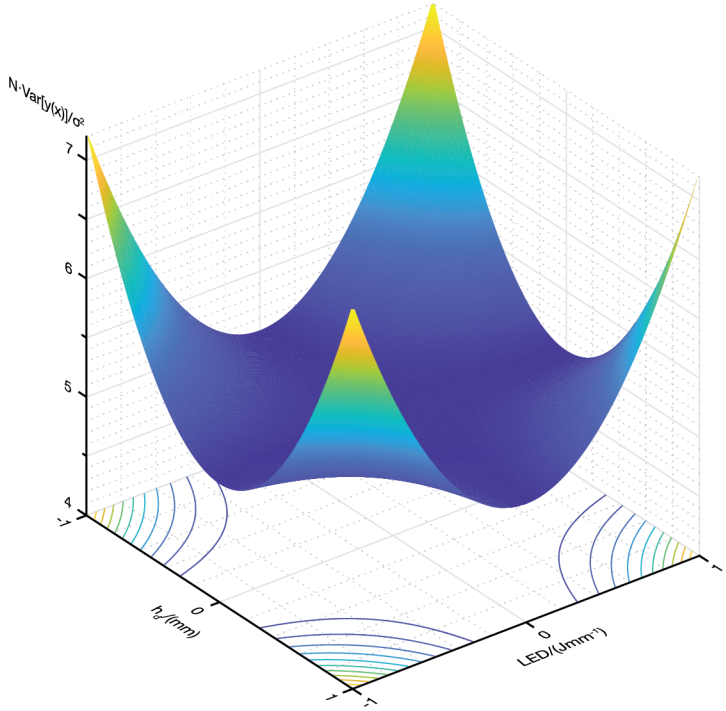

Fig. 4.9 Scaled Prediction Variance surface for a 3^2 factorial design.

Accordingly, a 3^2 factorial design was opted for the optimisation campaign described in this thesis. Three replications were also considered for the optimisation campaign to increase the number of degrees of freedom of the error, thereby increasing the reliability of the results in turn. As only two factors were investigated, i.e. LED and h_d, the same number of trials would have been required by both the CCD and the 3^2 design, removing a first potential advantage held by the CCD over the 3^2 one. Moreover, the selection of a CCD would have been impractical since the optimisation campaign needed to be centred on the point LED = 80 J mm^{-1} and h_d = 0.25 mm, as previously concluded in Section 4.1. The low h_d central value, along with its lower limit set at 0.1 mm, delimited a relatively small region of interest. A rotatable CCD would have been unable to accommodate its axial run withing the available design space, forcing the choice for a CCD whose axial runs lied at the same distance of the factorial points. In two dimensions, a similar CCD would be indistinguishable from a 3^2 factorial design. After the delineation of the experimental

plan, it was necessary to define the levels of the factors. LED and h_d levels were selected to have two factorial points along the same direction defined by the steepest descent method. The other process parameters, i.e. S_d and V_{Ar} were maintained at the same levels used during the steepest descent. The quantitative values of factors levels are reported in Table 4.1.

Table 4.1 Levels of the investigated factors.

	Low level -1	Intermediate level 0	High level 1
$LED/(\mathrm{J\,mm^{-1}})$	76	81	86
$h_d/(\mathrm{mm})$	0.10	0.25	0.40
$S_d/(\mathrm{mm})$		8	
$V_{Ar}/(\mathrm{L\,min^{-1}})$		2	

4.2.2 Results and Discussion

Five repeated measures were performed on each LPed sample perpendicularly to the direction of LPed tracks. Therefore, $Ra_\perp$ and $Wa_\perp$ were the main parameters considered and discussed. Other R and W-parameters were measured and reported for the sake of completeness, as already done during the exploratory analysis.

ANOVA for $\mathbf{Ra_\perp}$

Table 4.2 collects the numerical results of the ANOVA for Ra. The p-value test immediately reveals that only the h_d maintained a significant role in the distribution of the results. Both the linear h_d term and the quadratic h_d^2 term were statistically significant above the 95% confidence level, and with similar effect sizes. They collectively accounted for approximately a quarter of the overall variability. Setting aside other small contributions, the vast majority of the remaining variability was accounted by the pure error. It is noteworthy that the lack of fit of the model was not found to be significant, suggesting that the non-linear model was sufficient for describing the behaviour of the system. However, the pure stochastic error had a prominent role in the distribution of the results. The same conclusions could also be reached considering the regression model provided by the ANOVA, which represents

Table 4.2 ANOVA for $Ra_{\perp}$.

		DF	Adj SS	Adj MS	F-value	p-value	η^2
Model		5	1.0992	0.2199	5.76	0.002	0.578
Linear	LED	1	<0.0000	<0.0000	<0.00	0.974	<0.000
Terms	h_d	1	0.4841	0.4841	12.68	0.002	0.255
Square	LED^2	1	<0.0000	<0.0000	<0.00	0.995	<0.000
Terms	h_d^2	1	0.5039	0.5039	13.20	0.002	0.265
2-Way Interaction	LED$\cdot h_d$	1	0.1113	0.1113	2.92	0.102	0.058
Error		21	0.8014	0.0382			0.422
Lack-of-fit		3	0.1402	0.0467	1.27	0.314	0.074
Pure Error		18	0.6613	0.0367			0.348
Total		26	1.9007				

the response surface for Ra. Equation 4.3 contains the aforementioned model, all terms included.

$$Ra_{\perp} = 0.7 + 0.029 \cdot LED + 2.87 \cdot h_d + 0.00002 \cdot LED^2 + 12.88 \cdot h_d^2 + \\ -0.1284 \cdot LED \cdot h_d \tag{4.3}$$

This model ensured an acceptable description of data dispersion, with the R^2 coefficient close to 60%. The relatively low value is likely affected by the great role that the stochastic error plays, which simultaneously reduces its predictive ability, R^2_{Pred} only slightly above 30%. A similar outcome partially undermines the possibility of using the model for predicting LP results, potentially hindering the scope of the same optimisation campaign. Moreover, the pooled standard deviation S of the model was found to be equal to 0.2 µm, which is significantly lower than the value computed during the experimental campaign ($S_{exploratory} = 0.488\,\mu m$). This result helps understanding that the random effects influencing the distribution of the data were smaller than during the previous campaign. Therefore, stochastic phenomena had a small effect and still managed to overshadow the effects of the investigated parameters. In fact, the response variable did not undergo a sudden change throughout the region of interest, remaining at almost constant values. This behaviour strongly suggests that the new region of interest is a plateau-like one,

and that it is likely to also contain the minimum of the response variable. This consideration still supports the importance of the obtained model, proving a possible explanation for its poor prediction capability.

One strategy to enhance the predictive capacity of the model and, consequently, the ability to accurately locate the minimum point, is the removal of irrelevant terms from the same equation. The procedure is referred to as *stepwise* regression, and aims at defining an equation model comprising only the terms that are more significant than a predetermined threshold. Starting from an empty model, the stepwise procedure adds one term at the time, checking for its significance. At each iteration, terms that are found to be more significant than the chosen threshold are retained, whereas those terms that are not found to be significant are removed. The procedure continues until all terms have been tested for significance, all significant terms have been included in the model and all non-significant terms have been excluded from it. At the end of the procedure the equation may be further elaborated to obtain a hierarchical model. A hierarchical model includes all the lower-order terms required by higher-order ones. For instance, if the interaction between two main effects is found to be significant, a hierarchical model is obtained including both linear terms. While a hierarchical model is not always necessary, it ensures an easier handling of the equation. The main advantage of handling a hierarchical model is the possibility of expressing the independent variables in their natural unit of measures, as it has been done thus far. In the absence of a hierarchical model, terms must be expressed in terms of scaled values, namely between ± 1. The use of scaled values may introduce an additional complexity level to the use of the model, which should be avoided if possible.

Therefore, the stepwise procedure was applied to the model described in Equation 4.3. The model was made hierarchical at the end of the procedure, resulting in Equation 4.4. The main feature of the stepwise model is the absence of the quadratic term LED^2. This single change resulted in an R^2_{Pred}, now close to 40%. Although this result is far from being optimal, it still represents a meaningful improvement from the starting condition.

$$Ra = 0.57 + 0.0324 \cdot LED + 2.87 \cdot h_d + 12.88 \cdot h_d^2 - 0.1284 \cdot LED \cdot h_d \qquad (4.4)$$

Figure 4.10 collects the normal probability plots of the residuals for both the complete and stepwise model. In both cases no significant deviations from normality were highlighted, and no systematic biases were detected. This provides an additional indication contributing to increase the reliability of the results obtained.

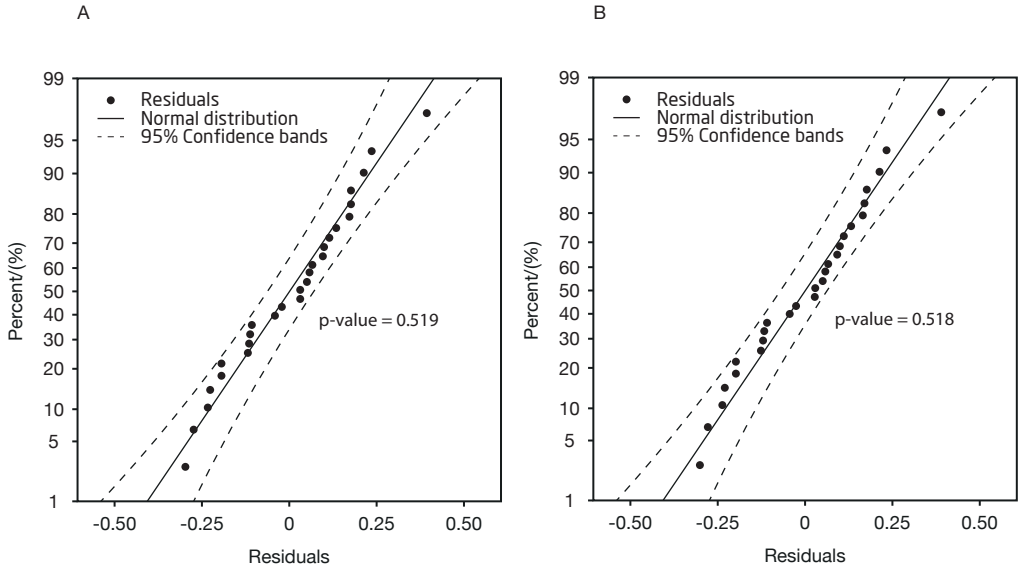

Fig. 4.10 Normal probability plot of residuals for $Ra_{\perp}$; A) complete model; B) stepwise model.

Equation 4.4 describes Ra as a function of two independent variables, easy to be graphically represented. Figure 4.11 displays the plot of the Ra response surface. This plot allows the visualisation of the nonlinear h_d effects on the value of Ra. In particular, the contour plot highlights two main regions. The upper part of the contour plot, featured by medium-to-high h_d values, represents the actual optimal region for Ra. The energy conveyed by the LP treatment is sufficient to remelt the upper layer of the sample and correctly redistribute the material. Conversely, the lower part of the contour plot shows a gradual worsening of surface quality for higher energy values, i.e. for lower h_d values. In this region, a minimal contribution of the linear LED term can be also observed. An increase in the value of LED results in a further deterioration of Ra, in agreement to what has been just discussed. In addition, the surface plot also suggests that further surface quality enhancements might be achievable for higher LED values and moderate h_d. However, since Ra improvements were found to be extremely limited during the optimisation campaign, the introduction of an additional LED level was not deemed to be worth pursuing.

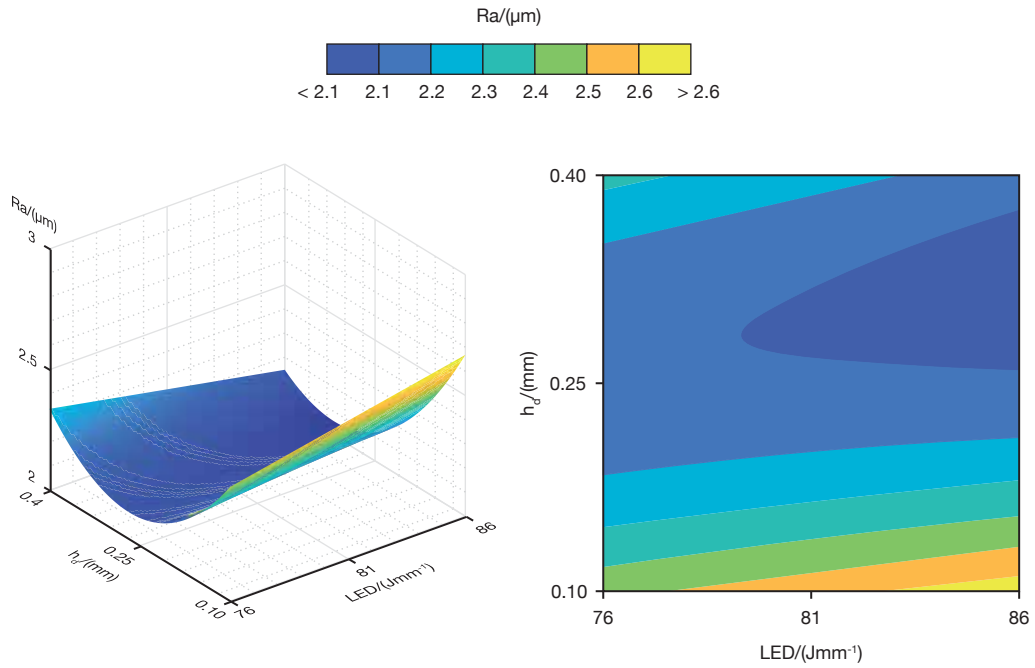

Fig. 4.11 Surface and contour plots for Ra.

ANOVA for $Wa_{\perp}$

Moving to Wa, Table 4.3 collects the results of the related ANOVA. The only term that was found to be significant at a confidence level of 95% is the h_d^2 quadratic term, while LED^2 and h_d were significant only at a 85% confidence level. The primary role of h_d^2 is also established by the η^2 coefficient. h_d^2 accounted for around 25% of the entire variability of the system, while the other considered terms all shared slightly more than 25% of the variability. The remaining 40% of system variability is directly relatable to the error, in a situation quite similar to the Ra one. Furthermore, both the complete model, Equation 4.5, and the model resulting from the stepwise algorithm, Equation 4.6, have extremely similar R^2_{pred} coefficient, lower than 10%. This strongly established the inadequacy of Wa models in predicting new values in the region of interest, drastically hindering their applicability. However, the surface plot of Wa was depicted in Figure 4.12 nonetheless. The prominent role of second-order effects is clearly depicted buy the shape of the surface, characterised by the presence of saddle point at the centre of the region of interest. Although the information provided by the graph should be carefully handled, due to the low prediction capabilities of the model, it may still be useful for the present investigation. The region defined by intermediate h_d values and high LED values is one of the two regions leading to the

lowest Wa, and was already identified as an optimal response region for Ra. Figure 4.13 displays the Wa curve level overlayed on the Ra ones, and highlights a region where both response variables are minimised simultaneously.

Table 4.3 ANOVA for Wa.

		DF	Adj SS	Adj MS	F-value	p-value	η^2
Model		5	22.774	4.555	2.98	0.035	0.415
Linear	LED	1	1.510	1.510	0.99	0.332	0.028
Terms	h_d	1	3.433	3.433	2.24	0.149	0.063
Square	LED^2	1	3.705	3.705	2.42	0.135	0.067
Terms	h_d^2	1	13.339	13.339	8.72	0.008	0.243
2-Way Interaction	LED$\cdot h_d$	1	0.788	0.788	0.51	0.481	0.014
Error		21	32.137	1.530			0.585
Lack-of-fit		3	0.716	0.239	0.14	0.937	0.013
Pure Error		18	31.421	1.746			0.572
Total		26	54.911				

$$Wa = -197 + 5.12 \cdot LED - 2.5 \cdot h_d - 0.0314 \cdot LED^2 + 66.3 \cdot h_d^2 + \\ -0.342 \cdot LED \cdot h_d \tag{4.5}$$

$$Wa = -190 + 5.03 \cdot LED - 30.2 \cdot h_d - 0.0314 \cdot LED^2 + 66.3 \cdot h_d^2 \tag{4.6}$$

The optimal set of parameters, granting an Ra minimum, was computed by means of the gradient of the 2-order model resulting from the optimisation campaign. The procedure resulted in LED = 86 J mm^{-1} and h_d = 0.32 mm, leading to a predicted Ra mean value of 2.06 µm. The confidence interval (CI) of the same mean value was found to be equal to $(1.93, 2.18)$, at a confidence level of 95%. Figure 4.14 shows the same optimal values for LED and h_d on Ra factorial plots. The same set of process parameters was also used for predicting the corresponding value of Wa. The Wa model predicted a mean value of 7.85 µm, with a $CI = (6.85, 8.57)$. The predicted values was also experimentally validated by additional LP runs. In particular, three more LP treatments were carried out with the optimal set of process parameters previously outlined. As always, five repeated measurements were performed with

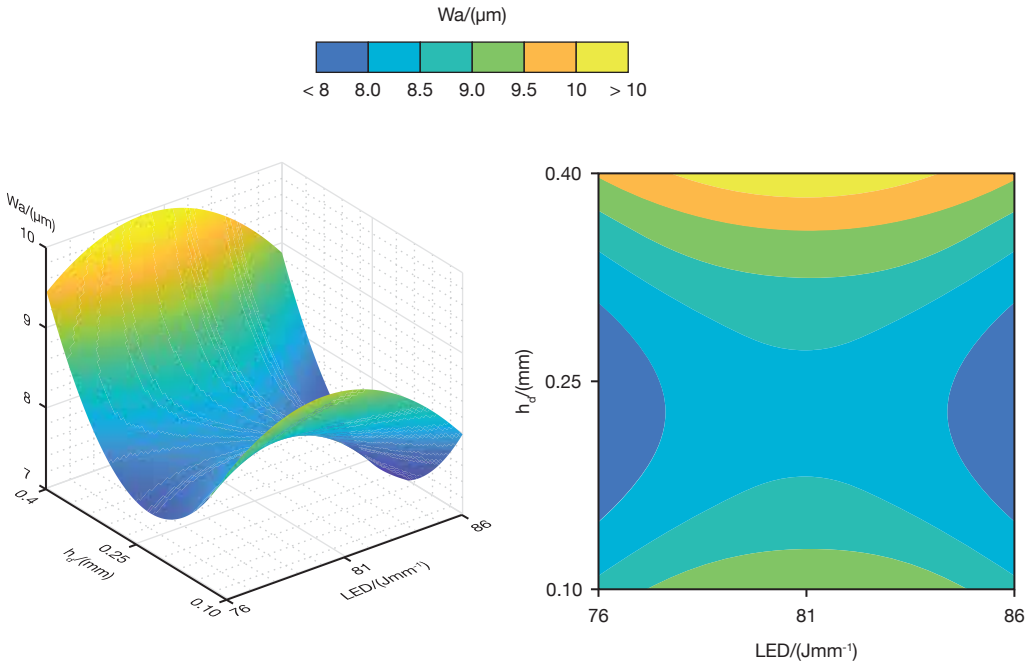

Fig. 4.12 Surface and contour plots for Wa.

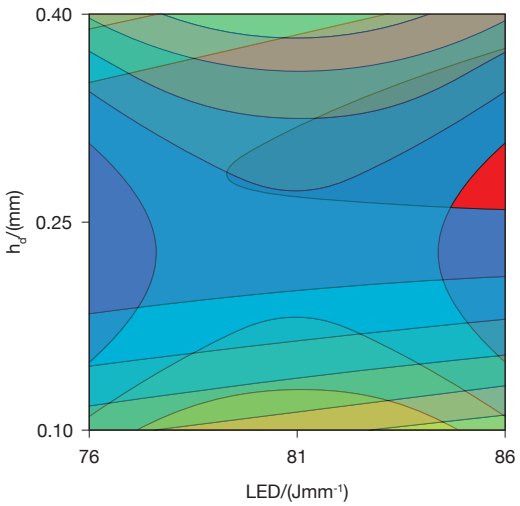

Fig. 4.13 Overlay of Wa and Ra curve levels.

the roughness metre on different positions on the LPed surfaces, and their mean considered as response variable.

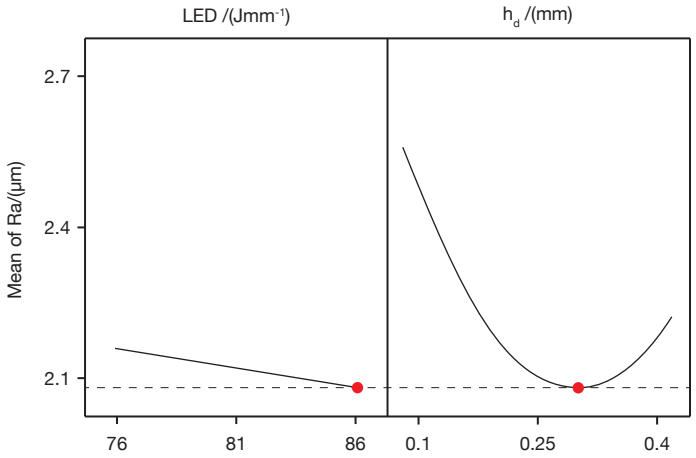

Fig. 4.14 Optimal set of process parameters (LED = 86 J mm^{-1}, h_d = 0.32 mm) for Ra minimisation.

Figure 4.15 presents the qualitative results of the finishing treatment carried out with the optimal set of process parameters. The surface of the sample appears slightly oxidised, suggesting that the shielding gas flow rate might not be sufficient to prevent the oxidation induced by the high thermal energy conveyed during the treatment. In addition, the R-profile and the W-profile did not highlight critical features induced by the finishing treatment onto the profile.

Table 4.4 presents the numerical results of R and W-profile parameters measured on the three samples. Starting from Ra, the measured value is comparable with the CI estimated during the optimisation campaign. In fact, the two-sample T-test did not highlight significant differences between the means at a confidence level of 95% (p-value = 0.173). Although the model did not have extremely high predictive ability, it was able to correctly predict the position and the value of the Ra minimum. This is an important proof of the potential of the model, particularly for future investigations. Overall, a remarkable 91% reduction of the DEDed samples has been reached, restating the profitability of using DED-LB systems for both deposition and finishing operations. Similarly, also Rz demonstrated sensible reductions close to the 93% of the as-built value. In addition, Rsk remained close to zero and Rsk close to three, as in the as-built profiles. Rsk and Rku ensures that the R-profile remained symmetrical and normally distributed along its mean line after LP operations. Conversely, the measured Wa can be considered statistically different

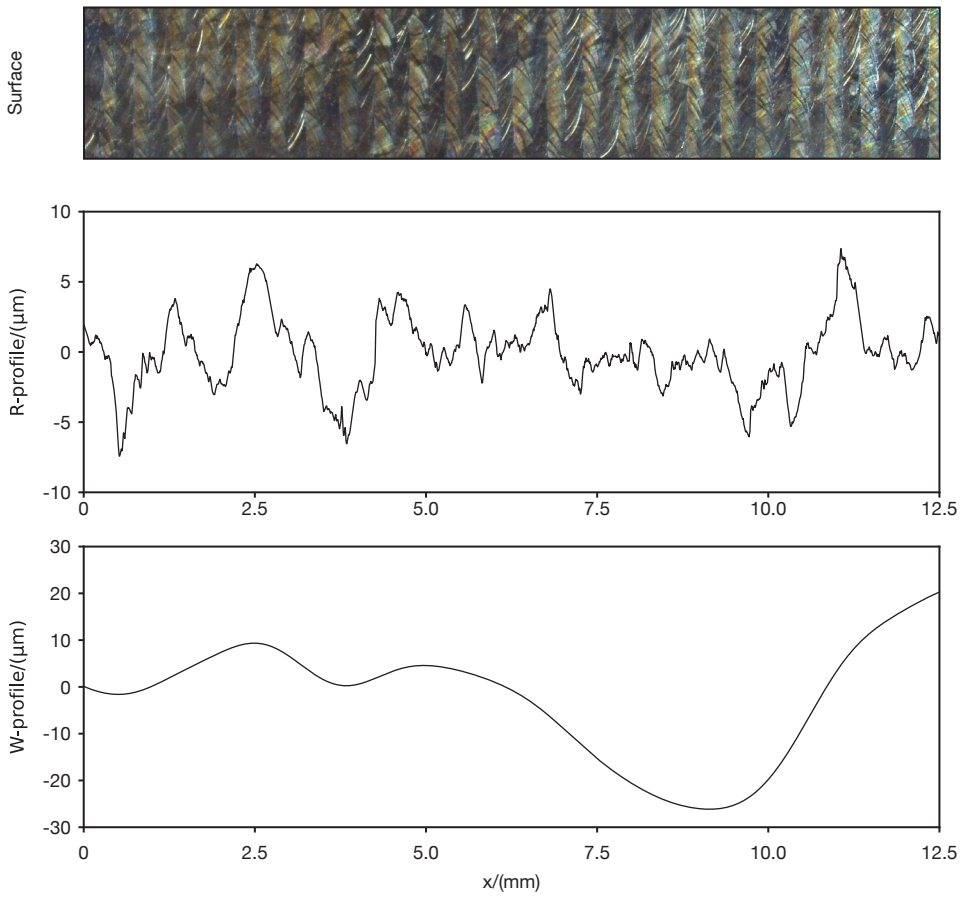

Fig. 4.15 Picture, R-profile and W-profile of the surface after the LP treatment performed with the optimal set of process parameters.

from the predicted value with good approximation, as the two-sample T-test resulted in a p-value of 0.059. However, the T-test did not highlight a drastic difference between the means, suggesting that the model used for prediction may not be entirely without utility. Apart from the prediction ability of the Wa model, the final Wa marked a 52% percent reduction of the as-built value, which can be considered a satisfying result nonetheless. Finally, the LP operation also resulted in a considerable Wz improvement, with a 61% reduction of the as-built value.

Therefore, it can be confidently concluded that both R-profile and the W-profile were significantly smoothed during the experimental campaign. When finished with the optimal set of process parameters, the surface of the quality deemed to be satisfactory and comparable with the quality ensured by mechanical finishing processes.

Table 4.4 R-profile parameters and W-profile parameters for a complete characterisation of the sample finished with the optimal set of process parameters.

Ra (µm)	Rz (µm)	Rsk (-)	Rku (-)	Wa (µm)	Wz (µm)
2.18 ± 0.10	10.9 ± 0.67	-0.04 ± 0.13	2.90 ± 0.35	9.31 ± 0.70	39.7 ± 1.00

4.3 Laser Polishing of Lateral Surfaces

The previous exploratory campaign was exclusively dedicated to the LP of the upper surfaces of DEDed samples. In order ascertain the potential of LP in a real industrial scenario, it is necessary to test its capabilities also on the lateral surfaces of DEDed components. DED-LB/Powder fabricates components in a layer-by-layer fashion, as is the case with all AM processes. The layer-wise fabrication of a component inevitably results in the formation of different textures between the upper surface and the lateral ones. Despite the fact that DED-LB/Powder is one of the AM processes that exhibits the least significant differences between the upper and lateral surfaces, it is nevertheless necessary to test the optimal set of process parameters on the lateral surfaces.

An additional sample was designed and deposited, serving as a substrate for further LP treatments on its lateral surfaces. Consequently, a $(25 \times 25 \times 25)$ mm^3 316L cube was deposited in close proximity to the edge of a $(110 \times 110 \times 10)$ mm^3 stainless steel platform, Figure 4.16. The position of the cube was required in order to facilitate the access to the lateral surface with the deposition head of the machine; depositing the cube in the centre of the platform would have presented a more complex task. The dimensions of the cube were constrained by the necessity of having a (20×20) mm^2 area for LP and subsequent roughness and waviness assessments. The optimal set of process parameters, defined for the upper surfaces, was employed fro the LP treatments. The process parameters are here recalled for the ease of the reader: $LED = 86\,\mathrm{J\,mm^{-1}}$, $h_d = 0.32\,\mathrm{mm}$, $S_d = 8\,\mathrm{mm}$, and $V_{Ar} = 2\,\mathrm{L\,min^{-1}}$. Following the completion of the treatment, five repeated measures were acquired using the roughness metre and subsequently aggregated in terms of mean and standard deviation.

Figure 4.17 depicts the improvements observed in the lateral surfaces following the LP treatment. As for the upper surfaces, lateral surfaces also exhibit notable

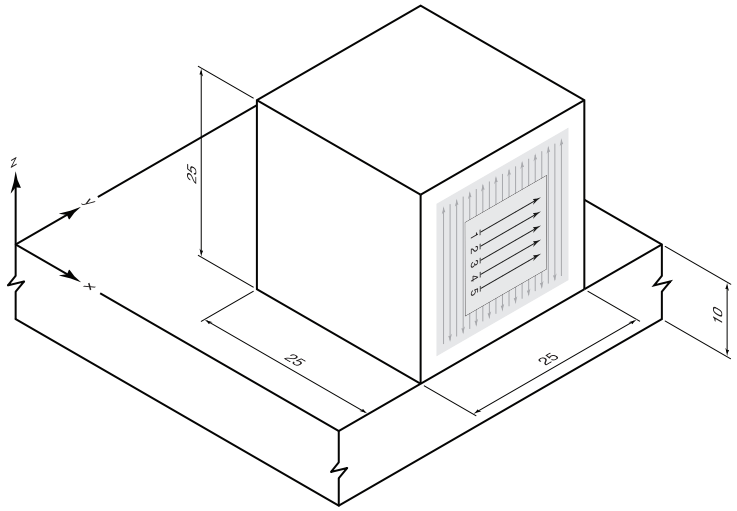

Fig. 4.16 Cubic substrate used for LP of lateral surfaces.

texture alterations. In particular, all partially sintered powder particles were molten and a new pattern emerged following LP. However, at least one significant difference can be easily identified in Figure 4.17. Despite the process parameters being the same as those used for finishing upper surfaces, this time the shielding gas was not sufficient to avoid surface oxidation. In fact, LP caused a consistent oxidation of the finished surface, which is indicative of the higher temperatures reached. The different geometry used as substrate can easily explain the higher temperatures reached during this LP operations. As already outline several times now, LP uses thermal energy to redistribute the outermost material layer. Therefore, the results of the treatment are influence by the thermal properties of the substrate, such as its heat capacity. In light of this, the dimensions and the location of the substrate can have a meaningful impact on the results of the LP treatment. In the preceding experimental campaign on upper surfaces, the flat samples, with a thickness of only 2 mm, were deposited on $(210 \times 210 \times 10)$ mm^3 platforms. It can be concluded that the flat samples were able to dissipate the heat conveyed by LP to the large platform underneath with ease, thereby lowering the temperature of the melt pool and avoiding oxidation. In contrast, the DEDed cube exhibited a markedly different scenario, whereby the energy was retained near the surface, resulting in a consistent temperature increase. Despite the absence of any sensor to quantitatively evaluate the temperature reached, the different colours of the oxides provide valuable information on the thermal history. The oxides formed on stainless steels exhibit a colour change with increasing temperature. At 300 °C, the oxides are pale yellow, at 450 °C they

turn to purple, and at 600 °C they become light blue. The exact palette can be observed in the image of the LPed surface in Figure 4.17, indicating that the average temperature of the surface reached a minimum of 600 °C in the final phase of the treatment (right-hand side of the image).

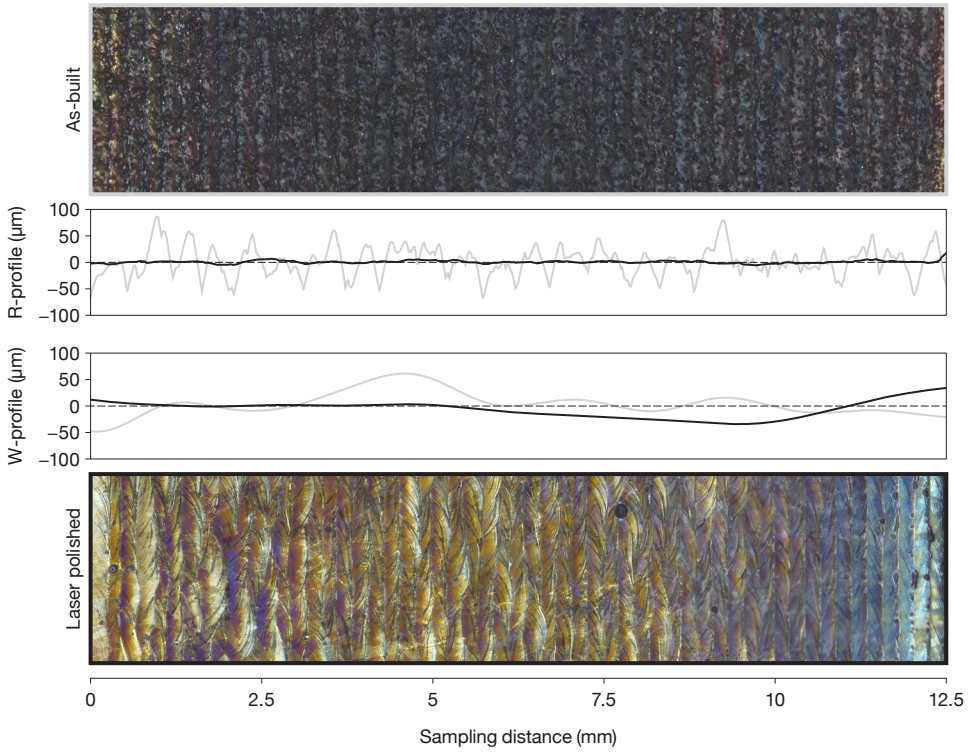

Fig. 4.17 As-built and LP lateral surfaces. R-profile and W-profile reported for completeness.

Nevertheless, the LP treatment led to a notable improvement in surface quality, despite the presence of oxidation. Table 4.5 presents the R and W-profile parameters for both the as-built and LPed surface. The initial value of Ra was reduced by 90%, a result that is consistent with the findings presented for the upper surfaces. However, given that the initial Ra value for the lateral surface was higher, the resulting Ra value following LP was also higher. Notwithstanding, the resulting Ra value is still comparable with that of rough machining, thereby being satisfactory for the purposes of this investigation. Similar considerations can be made for all other R and W-profile parameters, with no significant data to note.

Table 4.5 R-profile parameters and W-profile parameters of the lateral surface in as-built condition and after LP.

	Ra (µm)	Rz (µm)	Rsk (-)	Rku (-)	Wa (µm)	Wz (µm)
As-built	28 ± 0.86	155.08 ± 5.90	0.03 ± 0.08	2.66 ± 0.24	16.11 ± 2.84	82.83 ± 32.49
LPed	2.86 ± 0.59	14.83 ± 3.30	0.09 ± 0.04	3.60 ± 0.92	12.89 ± 3.75	58.54 ± 22.94

4.4 Conclusions

The present chapter introduced two additional phases that any structured experimental campaign should consider, the search for a new region of optimum, and the following optimisation campaign. Overall, the methodology employed throughout the entire experimental campaign could be adopted in different situations, such as when investigating different materials or substrates. It is crucial to reiterate that the empirical models delineated and the subsequent considerations are solely valid when referenced against 316L substrates, against which they have been tested. The most significant findings were summarised as follows:

- the search for a new region of optimum led to a new region of interest defined by a higher energy, namely higher LED and lower h_d compared to the values used during the exploratory campaign;
- the optimisation campaign led to the identification of an optimal set of process parameters, LED = $86\,\mathrm{J\,mm^{-1}}$ and $h_d = 0.32\,\mathrm{mm}$, granting an Ra minimum for LPed samples close to $2\,\mu\mathrm{m}$.
- the same optimal set of process parameters was tested on both upper and lateral surface of DEDed samples, certifying the good quality on both surfaces.
- additional experimental trials might be included to enhance the reliability, and predictive abilities, of the empirical models.

Chapter 5

Residual Stresses Induced by Laser Polishing

The viability of using LP for surface improvement of DEDed components has been demonstrated in detail in Chapters 3 and 4. However, it should be noted that the application of LP does not only affect the surface of the treated sample, it may also significantly alter the underlying material. Accordingly, this chapter discusses the residual stresses induced by LP in the utilised substrates; especially in the surrounding of the optimal set of process parameters defined in Chapter 4. Every type of manufacturing process, either casting, forging or machining, induces residual stress states in the resulting components. Residual stresses also play a major role in AMed components, particularly due to the high thermal gradients and rapid cooling times typical of AM processes [141]. Although residual stresses are inherently difficult to detect, as they have a null resultant on each section, they must be considered when evaluating the performance of a component [142]. The presence of large residual stresses can induce consistent distortions in the component, preventing it to attain the required geometrical accuracy [141]. In addition, residual stresses can be highly detrimental in terms of stress corrosion and fatigue life of both single components and welded joints [142, 143]. Consequently, residual stress measurement was the first activity carried out to ascertain the collateral effects of LP on the substrates.

Section 5.1 addresses formation mechanisms of residual stresses induced by manufacturing processes, with a particular emphasis on the LP of AMed components.

Section 5.2 presents the available scientific literature on LP of AMed components. Section 5.3 outlines the hole drilling method used for measuring the residual stress states along the vertical section of LP samples. Section 5.4 introduces the new dimensions of the platforms and of the substrates used for LP. These samples were specifically designed for the current investigation, aiming at the most efficient material use. Section 5.5 presents the results of the experimental activity performed to measure the residual stress state in LPed samples. Useful insights were provided on the influence of LED on residual stress states after LP. Finally, Section 5.6 draws the conclusions and defines future outlooks on the topic.

5.1 Residual Stress Formation During Laser Polishing

It has been demonstrated that LP treatments result in the induction of residual stresses in treated components. The mechanisms underlying the formation of residual stresses have been extensively discussed in the literature. LP locally re-melts the uppermost layer of a component by the creation of consecutive melt pools along the scanned path. Upon melting, the material expands, yet remains constrained by the surrounding non-molten material. At this juncture, the high temperature of the molten pool and of the surrounding material serve to relief any potential induced stress. Conversely, as soon as the melt pool solidifies, the molten material contracts, thereby inducing a tensile residual stress along the remelted track. This time, the lower temperatures are insufficient to relax the induced residual stresses [144, 145], which remain in the material in the aforementioned residual stress state, as in Figure 5.1A. Furthermore, additional mechanisms may influence the residual stress state along the polished track. For instance, when working with high-carbon steels, the rapid cooling of the melt pool can ignite the martensitic transformation of the austenite. The transformation of austenite into martensite entails an expansion of the material, which is constrained by the surrounding one. This results in the formation of compressive residual stresses in the end [144, 145], as represented in Figure 5.1B. The aforementioned phenomena, namely material shrinkage and phase transformation, contribute to the generation of a complex residual stress state within the material.

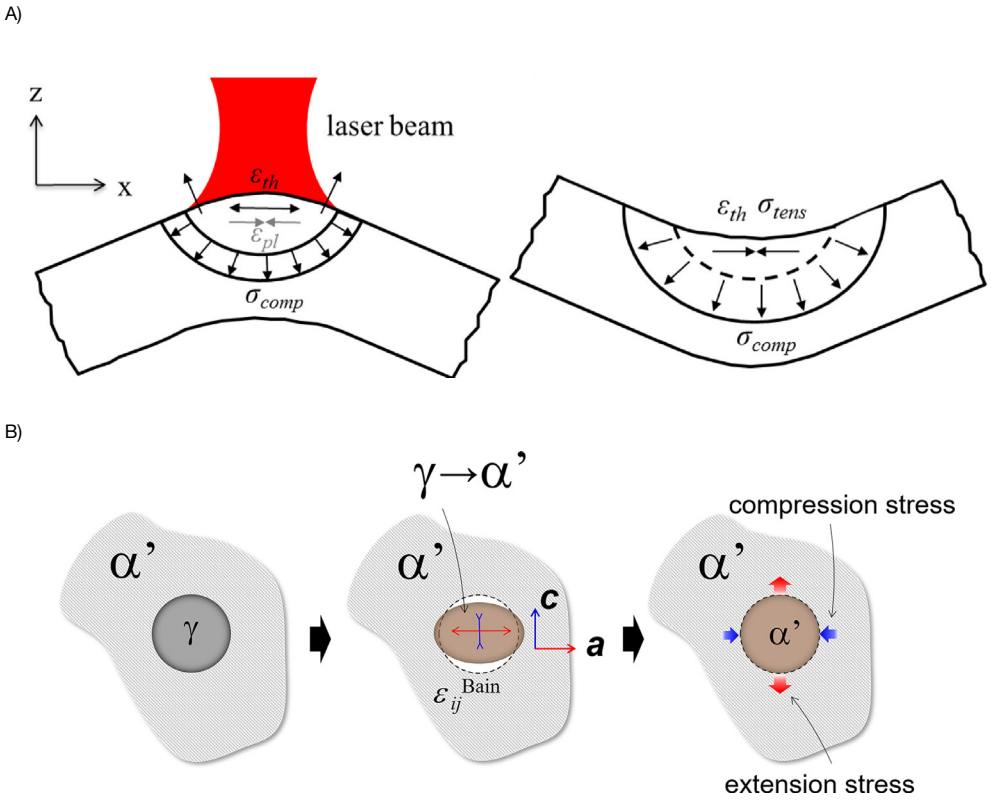

Fig. 5.1 Schematic illustration of the formation mechanism of residual stresses. A) Tensile residual stresses induced by material shrinkage [146]. B) Compressive residual stresses induced by martensitic transformation [147].

5.2 Overview of the Literature on Residual Stresses Induced by Laser Polishing

Being aware of the complexity of the mechanisms involved, several empirical studies attempted to give a description of the residual stress states induced by LP treatments. Preußner et al. [145] observed the appearance of high residual stresses after the LP of hot-work tool steel. They observed that low laser powers resulted in strong tensile stresses on samples surfaces. However, as laser power increased, residual stresses decreased and eventually shifted to compressive stresses. This was explained by the different importance that the shrinkage and the phase transformation mechanisms had throughout the experiments. Xu et al. [148] laser polished 718H samples and subsequently laser annealed them to mitigate the expected residual stresses. Consistent tensile stresses, about 600 MPa, manifested on all samples after LP, confirming the need of subsequent heat treatments. Therefore, the laser annealing

was carried out and resulted in almost null residual stresses on sample surfaces, lower than 50 MPa.

The residual stress state coming from LP treatments was also studied on AMed components, thus closer to the specific sphere of interest of this work. Gusarov, Pavlov, and Smurov [149] proposed a numerical model for residual stress estimation during DED and LP. They observed a proportionality between residual stresses and temperature gradient. Furthermore, they also observed that a higher interaction time between laser and component led to lower residual stresses and cracking. This behaviour is in good agreement with their previous claim, as a longer interaction time helps increasing the overall temperature of the component and reducing thermal gradients. Tian et al. [150] measured the residual stresses induced by LP on a Ti6Al4V component realised by PBF-EB. They confirmed the presence of high tensile residual stresses on the surface of LPed components, and observed a strong anisotropy of residual stresses, being twice as high along the polishing direction. As in the work of Gusarov, Pavlov, and Smurov, a stress relief phase was able to completely remove the residual stress state in the component, suggesting the possibility of easily dealing with eventual residual stresses also in AM components. Lee et al. [151] LPed samples manufactured by PBF-LB and measured their fatigue performances. They observed that samples that underwent a stress relief treatment after LP performed better than those sample that did not. Thus, although they did not directly measured the residual stress state inside LPed samples, they were able to confidently conclude about its presence due the different fatigue performances of the samples. Cho, Shin, and Shim [109] proposed the only work related to residual stress measurement on DEDed components treated by LP. They observed strong tensile residual stress on top of the LPed AISI 316L samples, also in this case strongly dependant on the considered direction.

Although the limited review here proposed was not intended to be exhaustive on the topic, some meaningful guidelines can still be drawn. LP treatments always induce tensile stresses on the surface of the component, whose intensity depends on the balance between material shrinkage and phase transformation, and on the direction considered. It can be reasonably assumed that these conclusions remain applicable regardless of the manufacturing process employed in the production of the component. However, the conducted investigations were limited to a near-surface description of residual stress states, as no information was provided about the distribution of residual stresses below the surface of the material. This is strictly

related to the utilisation of X-ray diffraction (XRD) for residual stress measurement. In fact, XRD is only capable of analysing the stress state on the surface, whereas other measurement techniques, such as the hole-drilling method, may provide more additional information about the stress state below the surface of the component. Consequently, the following section provides a detailed description of the hole-drilling method for residual stress measurement.

5.3 The Hole-Drilling Strain-Gauge Method

Numerous methods are today available for the measurement of residual stress states across the section of a component, not being limited to surface values. This section presents the hole-drilling method, which is one of the most widespread method across industry due to its simplicity and reliability [144, 142]. The hole-drilling procedure is based on the drilling of a hole at the surface location that is to be characterised. The drilling process removes a portion of the material of the component, thereby breaking the internal residual stress equilibrium. The redistribution of the residual stresses around the hole results in the deformation of the same material. If the residual stresses were tensile ones, the diameter of the hole would be larger than the nominal diameter. Conversely, the presence of compressive residual stresses results in a smaller hole than the nominal one. The hole-drilling procedure is therefore considered as semi-destructive, as it induces a localised damage in the component without precluding its correct functioning. The deformation of the hole induced by the residual stress state are typically very small and require the use of appropriate instrumentation to be detected and registered during the hole-drilling procedure. A strain gauge rosette is typically used to quantify the deformation of the material in the surroundings of the hole, as schematically illustrated in Figure 5.2. The strain gauge rosette deforms in a coherent manner with the material, and its deformation is detected by an external instrument as a change in resistivity.

The hole-drilling procedure for residual stress measurement is extensively described in the ASTM E837-20 standard [152]. It is essential to verify several hypothesis prior to the adoption of the hole-drilling technique. Firstly, it should be noted that this technique is only suitable for isotropic materials, whose constitutive equations do not depend on the considered direction. Secondly, the hole-drilling technique is limited to materials with a linear elastic behaviour. Accordingly, all

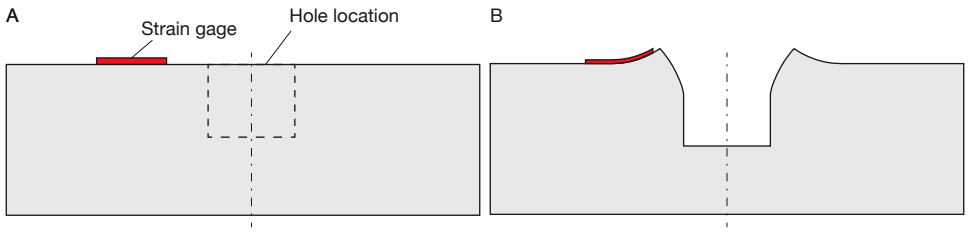

Fig. 5.2 Strain gauge method for residual stress measurement. A) Before hole drilling; B) after hole drilling.

materials exhibiting a nonlinear behaviour, such as rubber, elastomers and soft biological tissues, must be excluded beforehand. Metallic materials typically exhibits a primary linear elastic behaviour, which is then followed by a nonlinear one as they exceed their yield limit. It is therefore recommended that the hole-drilling procedure should be considered only when the expected residual stresses do not exceed the 80% of the yielding strength of the material, avoiding the occurrence of local yielding in the surroundings of the hole caused by local deformation. In the event that the hole-drilling procedure results in stresses higher than 80% of the yielding strength of the material, the results should be considered from a qualitative standpoint only, and not quantitatively. This is because computed stresses that exceed the 80% threshold tend to be overestimated, providing a trivial description of the stress state. Finally, the hole-drilling procedure should be applied only when the stresses do not vary consistently across the hole diameter. This requirement is relatively straightforward, as the hole-drilling procedure results in an average value that is measured across the diameter of the hole. In order to achieve the greatest possible representativeness of the result, it is essential for the stresses to be nearly constant inside the hole.

Once the initial requirements have been fulfilled, it is necessary to direct one's attention to the workpiece that is to be drilled. In particular, the area where the strain-gauge rosette is applied must be flat and free from visible defects. Moreover, the thickness of the workpiece may also be considered, as it influences the type of hole to be drilled. The thickness threshold distinguishing between through holes and blind holes depends on the type of strain-gauge rosette used for the measurement. The ASTM 837-20 [152] provides and extensive description of all possible scenarios.

Following the definition of the type of hole required by the procedure, the drilling procedure is carried out in a series of j steps. In the most generic case of non-uniform stresses, the strain relief is measured by the strain-gauge rosette on the surface of the material at every k step. The stress measured at a generic k step, for $1 < k < j$,

depends on all the residual stresses that existed in the material removed during the previous drilling steps, as formally expressed by Equation 5.1.

$$\begin{aligned}\varepsilon_j = \frac{1+\nu}{E}\sum_{k=1}^{j}\overline{a}_{jk}((\sigma_x+\sigma_y)/2)_k + \\ \frac{1}{E}\sum_{k=1}^{j}\overline{b}_{jk}((\sigma_x-\sigma_y)/2)_k\cos 2\theta + \\ \frac{1}{E}\sum_{k=1}^{j}\overline{b}_{jk}(\tau_{xy})_k\sin 2\theta\end{aligned} \tag{5.1}$$

where $\overline{a}_{jk}$ and $\overline{b}_{jk}$ are two calibration constants whose values are provided in the standard, and were defined through numerical simulations. Moreover, the index j refers to the drilling step being currently considered, whereas the index k represent the contribution of the previous drilling steps to the current one. Furthermore, $\overline{a}_{jk}$ and $\overline{b}_{jk}$ can be represented in their matrix form, as $\overline{\mathbf{a}}$ and $\overline{\mathbf{b}}$ respectively. The matrix notation offers the advantage of being extremely concise and suitable for the numerical solution of the problem.

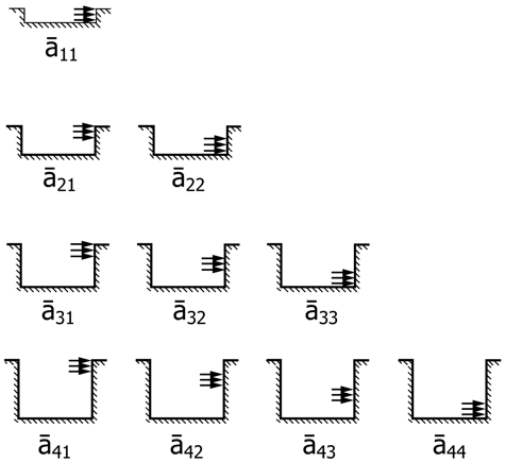

Fig. 5.3 Physical interpretation of the coefficients $\overline{\mathbf{a}}_{jk}$ and $\overline{\mathbf{b}}_{jk}$ [152].

Figure 5.3 provides a graphical representation of the meaning of the $\overline{a}_{jk}$ and $\overline{b}_{jk}$ coefficients. Upon completion of the drilling procedure, each strain gauge records a series of j steps, subsequently used for stress computation. The ASTM 837-20 standard proposes three coefficients, p, q, and t, which are defined as follows:

$$p_j = (\varepsilon_3 + \varepsilon_1)_j/2 \tag{5.2}$$

$$q_j = (\varepsilon_3 - \varepsilon_1)_j/2 \tag{5.3}$$

$$t_j = (\varepsilon_3 + \varepsilon_1 - 2\varepsilon_2)_j/2 \tag{5.4}$$

where the j index indicates the drilling step to which the parameter is referred to. If all drilling steps are considered simultaneously, also these coefficients can be expressed in their matrix form, as $\mathbf{p}$, $\mathbf{q}$, and $\mathbf{t}$. Consequently, the problem can be expressed as follows:

$$\bar{\mathbf{a}}\mathbf{P} = \frac{E}{1+\nu}\mathbf{p} \tag{5.5}$$

$$\bar{\mathbf{b}}\mathbf{Q} = E\mathbf{q} \tag{5.6}$$

$$\bar{\mathbf{b}}\mathbf{T} = E\mathbf{t} \tag{5.7}$$

in which $\mathbf{P}$, $\mathbf{Q}$ and $\mathbf{T}$ are the unknown matrices to be determined. $\mathbf{P}$, $\mathbf{Q}$ and $\mathbf{T}$ are defined in turn as:

$$P_k = ((\sigma_y)_k + (\sigma_x)_k)/2 \tag{5.8}$$

$$Q_k = ((\sigma_y)_k - (\sigma_x)_k)/2 \tag{5.9}$$

$$T_k = (\tau_{xy})_k \tag{5.10}$$

Equations 5.8 - 5.10 allow the straightforward definition of σ_x, σ_y and τ_{xy}, namely the Cartesian stresses. It can be often useful to express the residual stress state in terms of principal stresses and direction:

$$(\sigma_{max})_k, (\sigma_{min})_k = P_k \pm \sqrt{Q_k^2 + T_k^2} \tag{5.11}$$

$$\beta_k = \frac{1}{2} \arctan\left(\frac{-T_k}{-Q_k}\right) \tag{5.12}$$

Finally, σ_{max} and β can be used to synthetically describe the residual stress state in the component. In particular, β indicates the angle between the gauge 1 of the rosette and the direction of σ_{max}. A positive value of β indicates a clockwise angle, whereas a negative value of β indicates a counterclockwise angle. The previous brief rationale aimed to provide an overview of the principal considerations and computational steps that should be addressed during a hole-drilling strain gauge procedure. Further considerations about errors and compensation procedures were not reported for the sake of brevity.

5.4 Sample Definition and Instrumentation

The present section focuses on the analysis of the residual stress state induced by LP in DEDed samples. Each LP treatment was performed on a separate platform, avoiding any possible superimposition between residual stress states of different LP treatments. Thus, $(50 \times 50 \times 10)$ mm^3 platforms were cut from wider AISI 316L plates. On each platform a $(24 \times 40 \times 2)$ mm^3 sample was deposited. The dimension of the sample in the xy plane ensured the possibility of hosting a LP treatment large enough to accommodate two residual stress measurements, one serving as backup. The z dimension was maintained at 2 mm to make the sample representative of bulk DEDed components. Figure 5.4 reports the dimensions of the sample used for residual stress measurements. Four samples were deposited, comprising one representing the as-built condition which was used as reference, and three samples that were LPed with the same h_d and different LEDs. The process parameters were selected on the basis of the optimal set of process parameters defined in Chapter 4. Consequently, the h_d was maintained at 0.32 mm and the LED was varied on the same three levels used for the optimisation campaign, namely 76 J mm^{-1}, 81 J mm^{-1} and 86 J mm^{-1}.

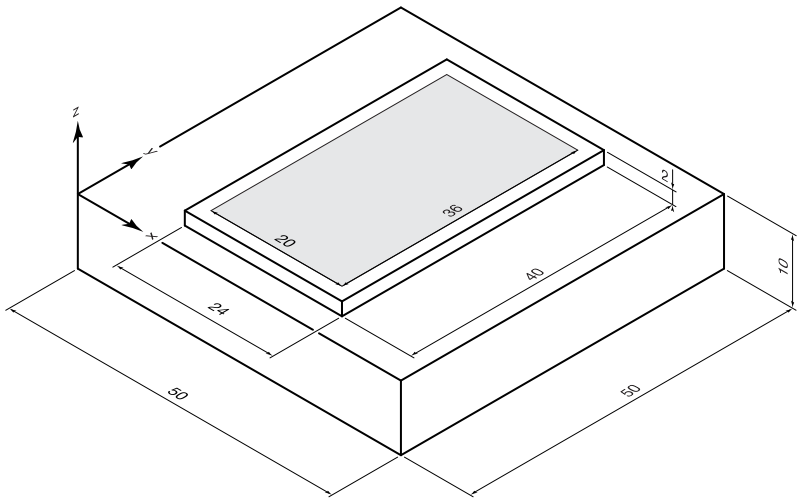

Fig. 5.4 Dimensions of the DEDed samples and of the LP surface.

In the present investigation, the strain gauge rosette employed was the 1-RY61-1.5/120R3, produced by HBM (Darmstadt, Germany). Each rosette was glued onto the sample as in Figure 5.5. The pneumatic system used for the drilling of the hole into the strain gauge was the MTS3000 - Restan, by SINT technology (Calenzano, Italy). The MTS3000 employs an air turbine to drive the mini-end which is used for the drilling operation. More in detail, the end mill was a 1-SINTCTT2/1 carbide inverted-cone end mill, by SINT technology. The signals from the rosette were acquired and amplified by the QuantumX MX440, by HBM. The data obtained from the QuantumX were gathered in a desktop computer using the RSM 7.13 software package, developed by SINT technologies, and later processed using the EVAL 8 software environment, also created by SINT technologies. The EVAL software follows the procedure outlined in the Section 5.2 Data elaboration resulted in the computation of σ_{min}, σ_{max} and β as a function of the depth under the surface of the sample.

5.5 Results and Discussion

Residual stress measurements were performed on the already introduced four samples, one left untreated for representing the as-built condition, and three LP treatments with fixed h_d and increasing LED.

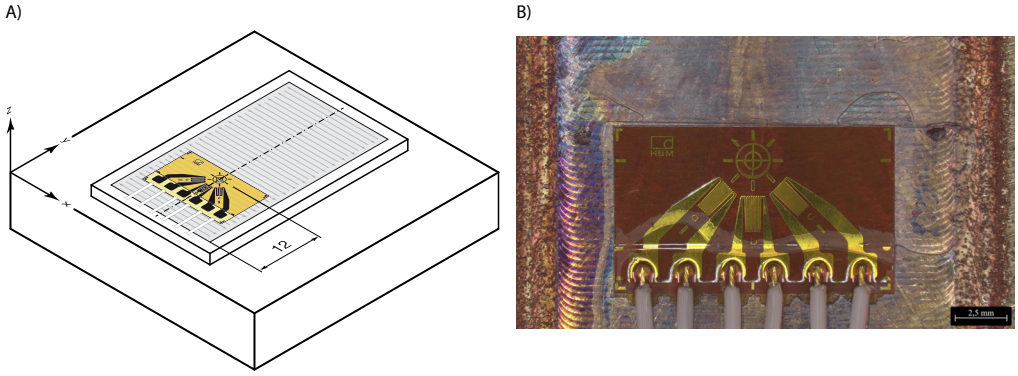

Fig. 5.5 A) Strain gauge placement on the LPed sample; B) image captured of the real strain gauge rosette glued on the surface of the LPed sample.

Figure 5.6 presents the outcomes of the residual stress measurement performed on the sample in as-built condition. The σ_{max} curve highlights contained stresses in the sub-superficial area. At a depth of 0.025 mm, the computed value of σ_{max} is equal to only 35 MPa. This value then increases rapidly with increasing depth, reaching a plateau of 350 MPa at a depth of 0.15 mm and remaining constant thereafter. Another noteworthy aspect is illustrated by the graph representing the β angle in relation to the measurement depth. It is here recalled that the β angle is the angle contained between the direction of the first strain gauge and the direction of the σ_{max}. In this case the β angle is constant and equal to 30°. It is also noteworthy that the as-built measurement only considered a depth of 0.5 mm, which is the depth of a single deposited layer. Therefore, a β angle that remains almost constant across a single layer seems a quite reasonable finding.

Figure 5.7 presents the findings of the residual stress measurement for the LPed samples. In order to facilitate interpretation, the results of all three samples have been superimposed. It is relatively straightforward to notice that the three σ_{max} curves exhibit a high degree of overlap, with minimal discernible differences. All three σ_{max} curves start at 0.025 mm with a pronounced tensile stress, between 138 MPa for LED equal to 76 J mm^{-1}, and 211 MPa for LED equal to 81 J mm^{-1}. As the measurement depth increases, the values of the maximum principal stresses grow in a similar manner, until they reach a value of approximately 400 MPa at the end of the measurement depth. The β angle remained at an almost constant value equal to 50° in the case of LED equal to 76 J mm^{-1} and 86 J mm^{-1}. However, the β angle exhibited a somewhat different behaviour in the case of LED equal to 81 J mm^{-1}. In fact, for LED equal to 81 J mm^{-1}, β was equal to 50° until 0.2 mm, then dropped

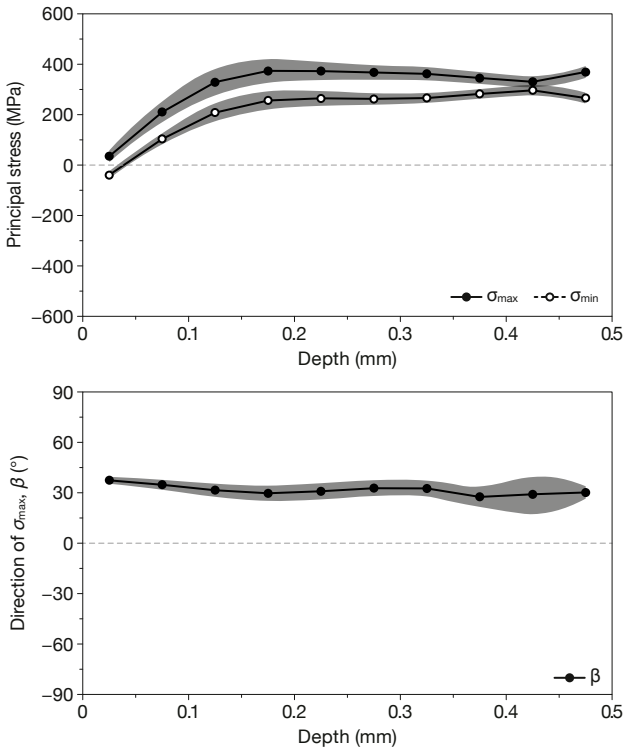

Fig. 5.6 Residual stresses measured on the as-built sample. σ_{min} and σ_{max} as a function of the depth, and β as a function of the depth.

to 40° until 0.7 mm, and finally dropped to $-60°$ at the end of the measurement. However, the different behaviour exhibited by the β angle referred to the 81 J mm^{-1} could be attributed to stochastic oscillations occurred during the trial, rather than being indicative of the internal residual stress state of the component.

A comparison of Figure 5.6 and Figure 5.7 provides some useful considerations. The application of LP treatments resulted in a significant residual stress increase, limited to the sub-superficial region. The increase in residual stress caused by LP was evident up to a depth of 0.4 mm, where the tensile stress values reached the plateau of 400 MPa. Consequently, no significant differences were detected between LP treatments performed with varying LED. This represents a promising outcome, as it permits the utilisation of LP treatments with diverse LED configurations.

The β angle was almost constant at 50° for all three LP treatments. It is important to recall here two important details:

1. the strain gauge rosettes were glued on the samples taking care that the second strain gauge, designated as B, was oriented perpendicular to the LP tracks;

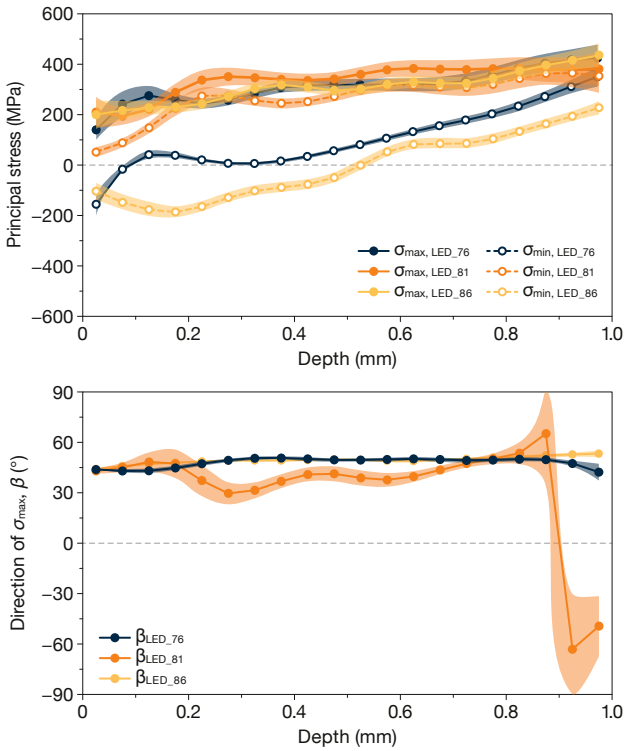

Fig. 5.7 Residual stresses measured on the LPed samples.

2. the first strain gauge, namely the A one, is oriented at 45° with respect to the second one.

Therefore, a positive 50° angle indicates that the principal stress is almost oriented along the direction of the polishing tracks. This evidence suggests that during the solidification of the melt pool, the solidification inside the same LP track had a greater influence on residual stress than the solidification across consecutive LP tracks. This piece of information could be extremely useful in the future, especially if one would like to give a specific direction to the principal stress during LP.

It can be concluded that the residual stress state after LP does not significantly differ from the residual stress state in the as-built condition, indicating that tensile stresses are present in the same order of magnitude. Given the potential detrimental impact of tensile stress on the mechanical performance of a component, as already discussed in Section 5.2, stress relief heat treatment should be considered also for LPed samples. Considering that the same stress relief heat treatments would have been required by DEDed components in their as-built conditions, LP treatments do not introduce any additional step in the manufacturing chain of a DEDed component.

5.6 Conclusions

Chapter 4 presents evidence that laser polishing can enhance the surface quality of DEDed components. The experimental campaign led to the definition of an optimal set of process parameters, minimising the roughness for both the upper and lateral surfaces of DEDed 316L components. However, questions emerged regarding the potential collateral effects that LP may induce in the components, such as the presence of undesired residual stresses. To address this, the current chapter proposed an experimental investigation aiming to quantify the residual stress state in LPed 316L components. The experimental trials highlighted the impact of LP treatment on the stress state of the polished samples:

- the application of different LED, specifically 71, 76 and 81 $\mathrm{J\,mm^{-1}}$ did not result in significantly different stress levels, with the stresses observed being almost equivalent between each other;
- the LP treatment modified the residual stress state in the subsurface region, where high tensile stresses were induced;
- despite the modification in the sub-superficial region, the residual stress state induced by LP does not excessively differ from that found in as-built samples;

Further activity should focus on investigating the effect of stress relief heat treatments on the residual stresses induced by LP. This could confirm the possibility of treating the sample finished using LP as normal DEDed components. Moreover, additional alloys should be investigated to ascertain whether and to what extent these material-specific results can be generalized.

Chapter 6

Microhardness Modifications Induced by Laser Polishing

The collateral effects that Laser Polishing induces in the substrates have already been presented in Chapter 5 in terms of residual stresses. However, substrate modifications are not limited to residual stresses, and typically also interest the microstructure of the same substrate. Microstructural analyses are usually conducted by cutting the samples, polishing the resulting sections with progressively finer abrasives, and finally treating them with chemical agents. Subsequently, qualitative evaluations are conducted upon the images captured with optical and electron microscopes, requiring a high degree of knowledge in material science, together with the specific instrumentation. Consequently, this option was considered outside the scope of the current investigation, being more focused on the technological aspects of the process. However, significant pieces of information on eventual microstructural modifications can be also obtained in other manners. For instance, the microindentation hardness evaluated on the cross section of the substrate is closely related to the microstructure of the same cross section. Accordingly, quantitative information can be obtained without the need for a proper microstructural evaluation. This option was considered viable for the current investigation, being able to provide additional information on the collateral effects induced by the LP treatments in the samples.

This Chapter presents the experimental activities performed to evaluate the microindentation hardness modifications along the cross section of the samples presented in Chapter 5. Section 6.1 outlines the mechanisms that are accountable for

microindentation hardness alteration during LP. Section 6.2 presents an overview of the scientific literature related to the microindentation hardness modifications induced by LP in metallic materials. Section 6.3 describes the indentation method and the reference standard. Section 6.4 outlines the procedure used for preparing the samples and the instrumentation employed. Section 6.5 contains the results of the experimental activity, and proposes a potential interpretation. Finally, Section 6.6 draws the conclusions of the topic, and outlines the future activities required for a comprehensive characterisation of LP collateral effects.

6.1 Mechanisms of Microhardness Modifications during Laser Polishing

The hardness of a material is a property that pertains to its tendency to resist localised plastic deformation, whether in the form of indentation or scratch. The concept of material hardness is "empirical in nature", as reported in the pertinent international standard, the ASTM-384 [153]. However, material hardness can provide valuable insight into its tensile strength [154], toughness, wear resistance and even machinability. Consequently, material hardness remains a subject of extensive investigation, and it is regarded as a useful indicator to be monitored during experimental activities. The hardness of a material is directly correlated with the freedom of motion of the dislocations within its microstructure, similarly to what can be observed for the tensile strength. Since a comprehensive explanation of the correlation between dislocation motion, microstructural defects and material strength was considered to be beyond the scope of the current investigation, it is here recalled that a lower freedom of motion of dislocations is usually correlated with higher material strength and hardness. The movement of dislocations within the microstructure of a material can be hindered by several factors, mostly related to the extent of the deformation of the lattice structure in question. LP operations of DEDed components involve the remelting of the outermost deposited material layer, with the potential of deeply impact the properties of the same material. In fact, the material that is molten during the LP treatment typically solidifies with different cooling rates compared to those observed during the previous deposition phase.

For instance, faster cooling rates typically result in the formation of finer microstructures, characterised by the presence of smaller grains and features [155]. It should be noted that the dimensions of the grains within the material can exert a significant influence on its hardness. A reduction in grain size implies an increase in the number of grain boundaries, which in turn necessitates a higher amount of energy to be crossed by dislocations, thereby limiting their freedom of motion. This functional correlation holds true for grain sizes in the order of magnitude of the micrometers. However, nanocrystalline materials may behave differently for grain sizes below the 30 nm threshold [156].

In addition to influencing the grain size, the singular cooling rates occurring during LP operations may also induce the precipitation of second phases [155]. When second phases are segregated from the primary phase, the original lattice structure is somehow distorted, creating an obstacle for the motion of the dislocations [155]. The amount of deformation is contingent upon the type of precipitates, and therefore depends on the combination of material and cooling rate.

Finally, LP treatments may also result in phase transformations. During the heating phase, the temperature of the material is typically increased up to the level where the alloying elements are all brought into solid solution. During the subsequent cooling phase, the fast cooling rates freeze the alloying elements within the lattice structure, thereby creating a supersaturated solution. This process, which is typically referred to as martensitic transformation, is always associated with pronounced lattice distortions caused by the alloying elements in the supersaturated solution. This ultimately leads to the enhancement in material hardness at the end of the process.

6.2 Overview of the Literature on Microhardness Modifications Induced by Laser Polishing

This section presents a selection of meaningful works that have investigated the variations of microindentation hardness caused by LP treatments, with a particular emphasis on LP of in AMed samples. As previously discussed in Section 6.1, LP treatments can alter the microstructure of the substrate, whether by grain refinement,

precipitates formation or martensitic transformation, with a meaningful impact on its hardness.

In their study, Chen et al. [105] observed the effect of LP treatments on 316L samples manufactured by PBF-LB. Microindentation hardness tests were performed on the cross sections of LPed samples, resulting in a general increase in the hardness value. In particular, the effect of the treatment was still detectable up to a depth of 80 µm. The observed microindentation hardness enhancements were primarily correlated with the finer grain size of the remelted layer, caused by the rapid cooling rate of the LP treatment. Cho, Shin, and Shim [109] measured the microindentation hardness modifications caused by LP in 316L samples manufactured by DED-LB. Similarly to what was concluded by Chen et al., LPed samples demonstrated an increased microindentation hardness value in the subsuperficial region, extending up to 50 µm. The microindentation hardness value increase was once more found to be correlated with the presence of a finer microstructure, outcome of the rapid cooling rates occurring during the LP treatment. However, Cho, Shin, and Shim also highlighted a reduction in microindentation hardness following a LP treatment performed with high energy density, namely high laser power and low hatching distance. This behaviour is in good agreement with the previous considerations, as the sample that underwent the high-energy LP treatment was also characterised by the formation of coarser grains. Zhihao et al. [157] proposed an investigation on LP of IN718 samples produced by PBF-LB. Their observations revealed a substantial increase in microindentation hardness near the free surface of the sample, up to a depth of 120 µm. This microindentation hardness increase was found to be correlated with a finer grain size in the remelted region, and with the appearance of fine second phases, γ'', which strengthened the alloy through precipitation hardening. In a study conducted by Hodgir, Singh, and Mujumdar [108], the authors employed LP for finishing CPM-9V samples deposited by DED. The microindentation hardness was measured across the sections of the samples and higher values were observed following the LP treatments. The raise in microindentation hardness was attributed to the martensitic transformation that the material underwent during LP, and to the precipitation of fine vanadium carbides, which had already been observed in CPM-PV claddings [158]. Finally, Temmler et al. [100] observed a drastic increase in nanoindentation hardness following the LP of H11 samples, primarily related to the martensitic transformation occurring under the fast cooling rates typical of LP treatments. While nanoindentation hardness was proven to yield higher values than

microindentation hardness [159], this investigation substantiated the drastic hardness enhancement associated with martensitic transformations.

Although the few examples reported are not meant to be exhaustive on the topic, they provide useful empirical validation to the potential of LP in altering the hardness of the materials undergoing the treatments.

6.3 The Indentation Method

The first attempt at describing the relative hardness of materials was performed by Mohs in the 19^{th} century [155], who ordered the materials according to their capability of leaving a scratch onto each other. This approach was purely qualitative and had to be overcome to provide a quantitative and unambiguous scale for material hardness measurements. Nowadays, the procedure to be followed for indentation hardness measurements in metallic materials is outlined in the ASTM E92-23 standard [160], which details the entire methodology, from the geometry of the indenter up to the computation of the hardness value. The central concept of indentation hardness measurements is the measure of the area of the indentation left on the material under a certain test load. In general, a large indentation area can be correlated with low hardness values, whereas small indentation areas with high hardness values. More in detail, the ASTM E384-7 [153] is specifically referred to microindentation hardness measurements in which the test force ranges from 1 to 1000 gf, thereby representing a special case of the more general condition described in the ASTM E92-23. Thus, the present section outlines the framework presented in the ASTM E384-7.

The first, and most important, element described in the ASTM E384-7 is the indenter. Two possible geometries are considered, namely the Vickers indenter and the Knoop indenter. Vickers indenters are square-based pyramids, made in diamond, with a face angle equal to 136°. Vickers indenters typically produce indentations with similar geometries, regardless from the test force used. In this case, the microindentation hardness computed would be the same for all test values, ensuring that the diagonals of the indentation overcome the 20 µm value. A schematic representation of a Vickers indenter and of the indentation left onto the material is provided in Figure 6.1. Conversely, Knoop indenters are rhombic-based pyramids, always in diamond, with face angles equal to $172°30'$ and 130°. Since Knoop

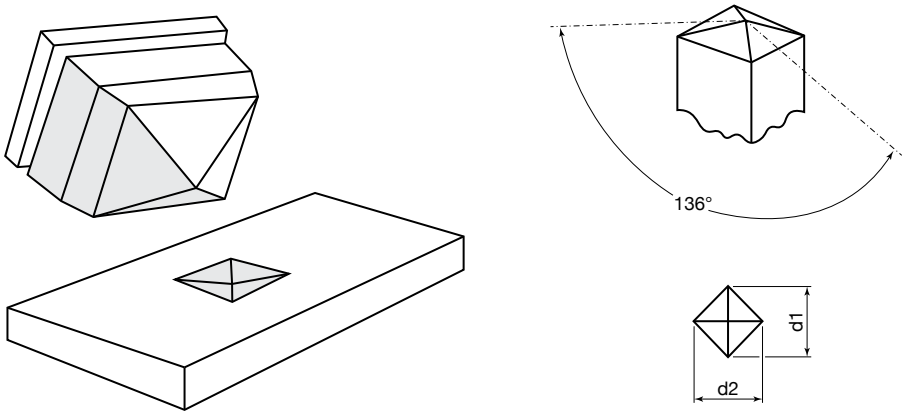

Fig. 6.1 Geometry of the Vickers Indenter. Adapted from the standard [153].

indenters presents a strongly asymmetrical shape, they can be fruitfully employed for measuring microindentation hardness on thin layers and coatings. In both cases, the test force should be applied for 10 to 15 s, with an approaching velocity in the range of 15 to 70 $\mu m\,s^{-1}$.

Apart from the indenter, the test specimen should also comply with the standard for ensuring accuracy of the measurement. The surface to be tested must be polished and free of defects that could interfere with the indentation. A deep chemical etching of the surface is not recommended since it could obscure the edges of the indentation, preventing from an accurate definition of the size of the same indentation.

Finally, the experimental apparatus should also include an optical portion for measuring the diagonals of the indentation left on the material. The resolution of the device should be equal to 0.1 µm in a range from 1 to 200 µm. Typically, two magnifications are required by the procedure, a 100x and a 400x magnifications. The first lens is demanded for the identification of the focal plane on the surface of test sample. Subsequently, the higher magnification lens can be used for the definition of a finer focal plane and for measuring the diagonals of the indentation. At the end of the procedure, the Vickers microindentation hardness can be computed as in Equation 6.1:

$$HV = 1854.5 \times P/d^2 \tag{6.1}$$

where P is the test force, expressed in gf, and d is the mean diagonal length of the indentation, expressed in µm.

6.4 Sample Preparation and Instrumentation

This section discusses the samples and the instrumentation employed for the measurements of microindentation hardness. In particular, the same samples already presented in Chapter 5 were employed also in this phase, subsequent to the completion of the residual stress measurements.

Figure 6.2 depicts the plane along which the sample were cut, exposing the surface where the microindentations were to be performed. Later, the samples were further cut for allowing easier mounting operations. Cutting operations were performed using the Baoma DK7732, a W-EDM system, produced by Suzhou Baoma (Suzhou, China), equipped with a Molybdenum wire with a diameter equal to 0.18 mm.

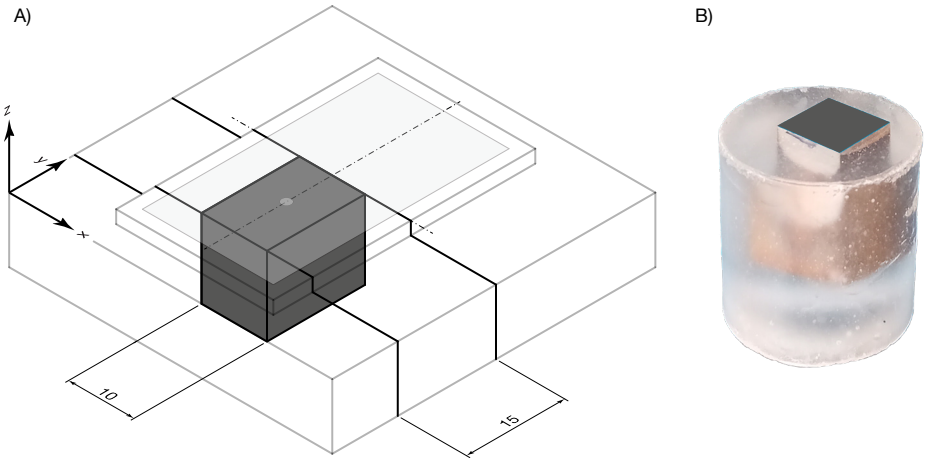

Fig. 6.2 Preparation of the samples for microindentation hardness measurement. A) Cuts performed with the W-EDM. B) Englobed Sample.

The mounting operations were performed using the KM-U cold resin produced by PRESI (Grenoble, France). Therefore, the sections of the englobed samples were polished with progressively finer abrasive papers, produced by the same PRESI, starting with a grit number equal to 800 and completing the work with a grit number of 4000. Once the surfaces were deemed to be smooth enough, the subsequent microindentations were carried out using the DVH-1000Z Digital Micro Vickers Durometer produced by United Test (Beijing, China). The DVH-1000Z is equipped with a Vickers indenter, has two objectives allowing magnifications of 100x and 400x, and an automatic motorized turret for switching between objectives and indenter. Moreover, the DVH-1000Z provides eight levels of test force, from 10 gf

up to 1000 gf, and a testing field that spans from 1 HV up to 2967 HV. Sixteen microindentations were performed on the cross section of each sample, with a test force equal to 300 gf and a 25 µm spacing between them.

6.5 Results and Discussion

This section presents the outcomes of the microindentation hardness tests performed on the cross sections of the as-built sample and of the three LPed samples. Prior to presenting the quantitative results, it is worth recalling that the 316L, the material employed for sample deposition, is an austenitic stainless steel, meaning that the martensitic transformation does not occur even when high cooling rates are involved. Additionally, the 316L does not form precipitates through the cooling process, eliminating the possibility of precipitation hardening. Therefore, the grain size is the sole microstructural feature that could potentially influence the hardness of the alloy. Since the LP treatments were performed with varying LED, different cooling rates were expected, eventually leading to different grain sizes.

Figure 6.3 depicts the microindentation hardness profiles of the four tested samples. The microindentation tests performed on the sample in its as-built condition resulted in hardness values ranging from 240 HV to 280 HV, with a mean value of 260 HV. These results are in good agreement with the findings of the investigations presented in Section 6.2 [109, 105]. Moving to the LPed samples, the sample finished with LED equal to 76 $J\,mm^{-1}$ did not exhibit a notable deviation from the values recorded for the as-built condition, especially in the subsuperficial region. It is worth recalling that the LED employed during the deposition phase had a value of 50 $J\,mm^{-1}$, thereby lower than the LED used in the LP treatment. This could be a contributing factor in explaining why the LPed sample did not highlight a significant increase in microindentation hardness. Since the energy employed was similar, the cooling rates under LP and deposition are expected to be comparable. Similar cooling rates yield similar grain sizes, eliminating the possibility of grain refinement induced hardening. Interestingly, LP treatments performed with LED equal to 81 $J\,mm^{-1}$ and 86 $J\,mm^{-1}$ resulted in microindentation hardness values that were lower than those registered during the test on the as-built sample. Both profiles exhibited a mean value of 220 MPa, maintaining a range between 200 and 240 MPa. The observed reduction in microindentation hardness can be attributed to the higher LED employed during

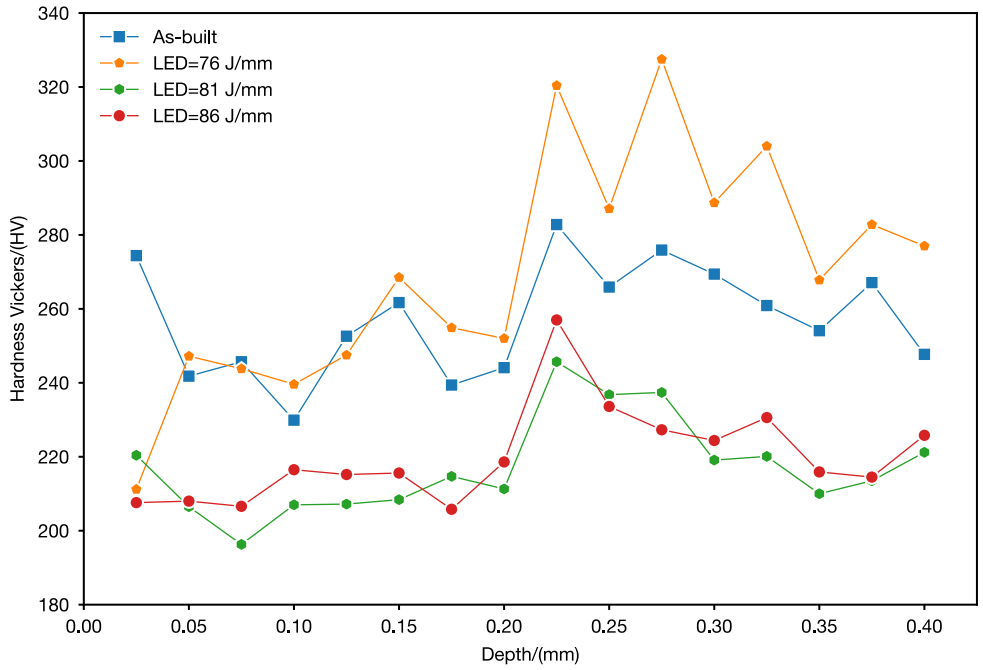

Fig. 6.3 Profiles of microindentation hardness evaluated on the cross section of LPed samples.

the treatment, which in turn resulted in reduced cooling rates and potentially in a coarser microstructure. This conclusion is once more in good agreement with the work by Cho, Shin, and Shim [109], in which the authors observed a reduction in hardness values following LP with high energy density.

The experimental trials covered a depth of 0.4 mm below the LP surface. However, the microindentation hardness profiles of the LPed samples did not converge towards the profile of the as-built sample at the investigated depth. This behaviour indicates that the depth of the remelted layer was at least equal to the investigated depth, which was equal to 0.4 mm. It would be beneficial for future investigations to consider a deeper investigation length in order to observe the microindentation hardness trends of LPed samples converge towards the as-built value and eventually superimpose.

6.6 Conclusions

The present Chapter aimed at providing another piece of information about the collateral effects that LP treatments induce in the substrates. Therefore, microindentation hardness tests were performed on the cross sections of the same LPed samples employed in Chapter 5 for residual stress measurements. The outcomes of the microindentation tests highlighted that:

- the sample left in its as-built condition was characterized by an average value of 260 HV, generally belonging to the range between 240 and 280 HV;
- the energy conveyed to the substrate during the LP treatment seems to have had a primary influence on the microindentation hardness of the final sample;
- the microindentation tests performed on the sample finished with LED equal to $76\,\mathrm{J\,mm^{-1}}$ resulted in hardness values close to the as-built condition, probably due to similar cooling rates between the deposition and the finishing phase;
- the microindentation tests performed on the sample finished with LED equal to $81\,\mathrm{J\,mm^{-1}}$ and $81\,\mathrm{J\,mm^{-1}}$ showed similar trends, generally with lower values than the ones measured on the as-built condition, probably caused by slower cooling rates under the LP treatments.

Additional experimental activities should be performed in the future to improve the quality of the findings. The two improvements considered to have a primary role in this scenario are:

- the introduction of a metallographic analysis to be paired with the microindentation tests in order to highlight the microstructure of the samples, and provide a comprehensive description of the effects of LP treatments on the substrates;
- microindentation tests should be performed on several parallel profiles on the cross sections of the samples in order to describe their entirety, and to estimate the variability of the hardness in the samples.

Chapter 7

Numerical Modelling of Laser Polishing Treatments

Experimental activities, as conducted in this work, represent the initial step required in the process of characterising an industrial process. Despite the information provided is certainly valuable, this comes at a cost of significant time and resources that are required. Following the completion of the initial experimental campaign, it is worth considering the introduction of simulative tools with the objective of enhancing the comprehension of the phenomenon under investigation, while simultaneously reducing the time and costs associated with the experimentation. As the complexity of industrial processes grows, it is evident that analytical solutions can only address extremely simplified models, which are typically far from real-life scenarios. Conversely, numerical models represent a viable alternative for closely simulating industrial processes, with the potential for consistent savings in machinery and materials.

This chapter proposes the utilisation of a conductive model to simulate the temperature distribution within the substrate during LP operations. Therefore, the conductive model was conceived as a tool to complete the body of knowledge granted by the experimental activity, without pushing the boundary of the current state of the art. Section 7.1 presents the scientific literature dedicated to the numerical modelling of LP. Section 7.2 outlines the heat conduction equation, together with the boundary and initial conditions required for its solution. Section 7.3 outlines the main features of the software package used and of the numerical model developed, with

emphasis on material properties, boundary conditions, and mesh size. Section 7.4 provides an empirical validation of the aforementioned model. It initially describes the experimental setup utilised, and subsequently compares empirical and numerical results. Finally, Section 7.5 draws the conclusions on the topic and outlines the future outlooks.

7.1 Review of LP Numerical Models

Over the past decade, the number of published studies related to the numerical modelling of LP has exhibited a constant grew, aligning with the growth in the number of published studies on LP itself, as displayed in Figure 7.1. This positive trend may be attributed to a number of potential factors. At first, the increase of the available computational power of commercial computers enabled the broader utilisation of simulative tools, obviating the necessity for high-end instrumentation. Secondly, following an initial phase of experimental investigation, the existing body of knowledge available on LP processes may have reached a level of maturity sufficient to support the development of numerical simulations on the topic. The majority of the published studies on numerical modelling of LP processes aims at predicting the resulting surface pattern after the treatment. Therefore, the vast majority of the published studies employ computational fluid mechanics (CFD) models, which consider both conduction and convection heat transfer phenomena inside the melt pool.

Nüsser et al. [161] proposed a review on LP defects and discussed possible reasons for each one of them. A number of defects, including ripples, bulges and undercuts, were found to be associated to the convective motions of the molten material during LP treatments. Marimuthu et al. [102] employed CFD simulations to predict the final surface roughness of LPed components fabricated by PBF-LB/M. It was concluded that the input energy was the primary parameter controlling the process, and that a reduction in the speed of the molten material within the melt pool resulted in a corresponding reduction in surface roughness. Similarly, Mohajerani et al. [162] employed a convective model to estimate the geometry of the melt pool during LP of tool steels. The value of absorbivity used in their model was calibrated by comparing the results of the model with experimental evidence. In a follow-up study, Mohajerani et al. [163] also established a positive correlation between the

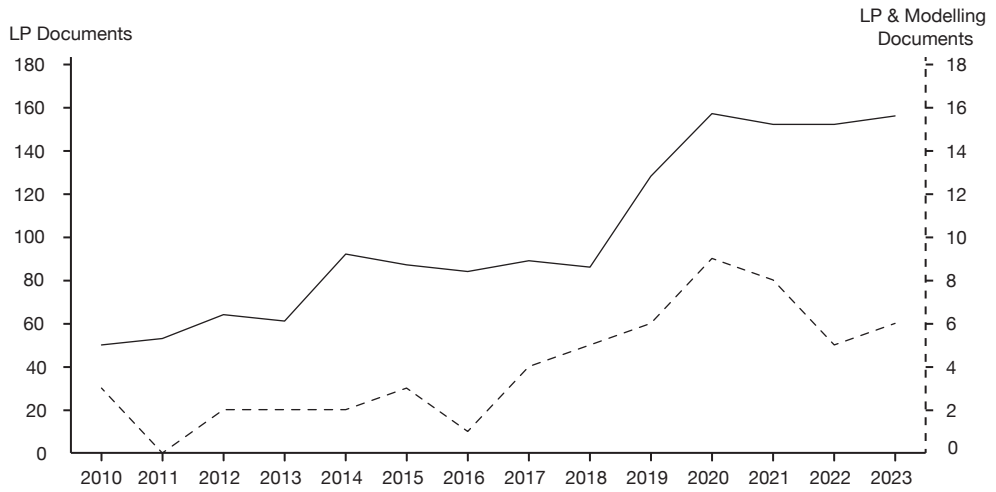

Fig. 7.1 Number of published academic documents with *LP* and *LP numerical modelling* as keywords. Data from Scopus.

absorbivity used in the model and the energy input for LP. In their study, Zhang, Zhou, and Shen [164] investigated the influence of capillary forces, associated with surface tension, and thermocapillary forces, related to the gradient of surface tension, on the geometry of the melt pool and on the resulting surface quality. Capillary forces dominated the creation phase of the melt pool, whereas thermocapillary forces assume a prominent role only after the complete development of the same melt pool. Xu et al. [165] proposed a melting and transition regimes model that correlated high thermocapillary flows with the formation of bulges following LP, as well as thicker remelted layers. Wang et al. [120] used a CFD model to understand the influence of the atmosphere in which the LP process takes place. Additionally, they succeeded in the integration of chemical reactions into their model, thereby predicting the presence of different inclusions for different gas atmospheres.

Although CFD models have been profitably used to achieve an in-depth understanding of the phenomena occurring during LP treatments, their broader implementation remains severely hindered. CFD simulations require a considerable investment of computational resources and can endure for several days. These factors justify the reason behind the extensive reliance on conductive models in both academic and industrial contexts. Soffel et al. [166] compared the results of a pure conductive model and of a conductive-convective model with experimental evidence. Although the convective model predicted the geometry of the melt pool with higher accuracy, the conductive model exhibited satisfactory performance. The conductive model

exhibited a tendency to overestimate the depth of the melt pool and underestimate the width of the melt pool. However, it offered a notable advantage in terms of computational efficiency, requiring only one minute to provide a solution, in contrast to the sixteen hours required by the convective model. Similarly, Meylan et al. [167] used a pure conductive model to estimate the temperature distribution during LP operations on tool steels. Their simulations also resulted in an overestimation of the depth of the molten pool and an underestimation of its width. Therefore, if the biases induced by conductive models are known beforehand, conductive models may be extremely resource efficient in the predicting the temperature distribution in the substrate.

7.2 Heat Conduction Equation

In the present work a pure conductive model was opted for the definition of the temperature distribution during LP operations. A pure conductive model relies upon the solution of the heat conduction equation, derived from the enthalpy equation, and represented in its local form by Equation 7.1. The heat conduction equation relates the temperature change in time with the heat flux across the boundary of the system, and with the heat generated inside the same body.

$$\rho c_p \frac{\partial T}{\partial t} - \nabla \cdot (k \nabla T) = \Gamma \tag{7.1}$$

In Equation 7.1, ρ is the density of the material, c_p is the specific heat of the material, and k is the thermal conductivity. Γ is the internal heat source of the model, for instance it may be related to chemical reactions, or to the heat generated by Joule effect. Equation 7.1, as all differential equations, cannot provide a unique solution on its own, as it needs to be completed by a set of initial and boundary conditions.

7.2.1 Boundary Conditions

Boundary conditions can be divided in three main categories depending on the type of constraint they are imposing. Being Ω the domain of the model, $\partial\Omega$ represents its boundary, namely the surface where the boundary conditions are eventually applied.

At first, Dirichlet boundary conditions impose an exact value of the solution of the differential equation. Dirichlet boundary conditions are often used in thermal problems when a surface, or part of it, is maintained at constant temperature, or in fluid-dynamic problems to model the no-slip condition of a viscous fluid near a fixed wall. Equation 7.2 formalises the Dirichlet boundary condition.

$$if \quad T \in \partial\Omega_D \quad then \quad T = T_D(t,x) \tag{7.2}$$

Differently from Dirichlet boundary conditions, Neuman boundary conditions impose a constant value to the flux across the model boundary. In thermal simulations, an adiabatic surface is a perfect example of a Neuman boundary condition, as the value of thermal flux is set to zero. Equation 7.3 reports a possible Neuman boundary condition for the heat conduction problem here considered.

$$if \quad T \in \partial\Omega_N \quad then \quad \frac{\partial T}{\partial n} = \hat{n} \cdot \nabla T = -\frac{q_n(t,x)}{k} \tag{7.3}$$

Finally, Robin boundary conditions are obtained by a linear combination of the two previous conditions. Robin boundary conditions relate the flux across the boundary of the model to the value of the solution on the same boundary. Equation 7.4 models a convective boundary condition as a Robin boundary condition; which represents one of the most frequent use of Robin boundary conditions.

$$if \quad T \in \partial\Omega_R \quad then \quad \frac{\partial T}{\partial n} = \hat{n} \cdot \nabla T = -\frac{h(T_\infty - T(t,x))}{k} \tag{7.4}$$

7.2.2 Initial Conditions

The previous subsection focused on the description of the boundary condition used for solving the heat conduction equation, Equation 7.1. However, the boundary conditions are not the only conditions required for the unique definition of the solution of the heat condition equations. Initial conditions are of the same importance, as they attribute a starting value to the response variable, namely the temperature, at the beginning of the investigated phenomenon. Equation 7.5 describes this concept:

$$if \quad t = t_0 \quad then \quad T(t,x) = T(t_0,x) = T_0 \tag{7.5}$$

where t_0 is the time at which the observation starts, and T_0 is the temperature assumed for each x in the model at time t_0. If the initial condition is not explicated the heat conduction equation cannot be uniquely solved.

7.3 Numerical Model Proposed

The present section outlines the numerical model developed for simulating LP treatments. As previously stated, the numerical model here proposed is a solely thermal model, limited to the computation of the temperature field during LP treatments. The software environment selected for the development of the numerical model was Abaqus FEA, a finite element analysis software developed by Dassault Systems (Vélizy-Villacoublay, France). Abaqus FEA is a well-known software suite for finite element analysis, both in the context of conventional manufacturing and of AM [168, 169, 170]. Abaqus provides a user-friendly environment for modelling the desired geometry and preparing the simulation with the necessary preprocessing. Abaqus provides a Direct solver, the one used in this investigation, which uses the Backward Euler method to discretise the main equations presented in Section 7.2 with respect to time. Additionally, the Direct Solver employs the Newton-Raphson method to address the non-linearities inherent to the model. The Newton-Raphson method requires the solution of a set of linear equations at each iteration, which Abaqus solves employing the Gauss elimination method for sparse matrices.

7.3.1 Geometry of the Part

The model comprised a platform measuring $(100 \times 100 \times 8)$ mm^3, with a substrate of $(60 \times 30 \times 2)$ mm^3 on its upper surface. The dimensions of the substrate were the maintained in accordance with those of the substrates employed in Chapters 3 and 4, in order to accommodate up to two LP treatments.

7.3.2 Material Properties

The material considered in the numerical model for both the platform and the substrate was the 316L, which is the same material used in the previous experimental campaign. The main material properties required by the heat transfer model, and

already expressed in the heat transfer equation, were the material density, the specific heat and the thermal conductivity, as depicted in Figure 7.2 as a function of temperature. The units of measurement used to represent the material properties in Figure 7.2 were selected in order to obtain a consistent system of units. The building of a consistent system of units is of primary importance in Abaqus, as no units of measurement are explicitly set in the software.

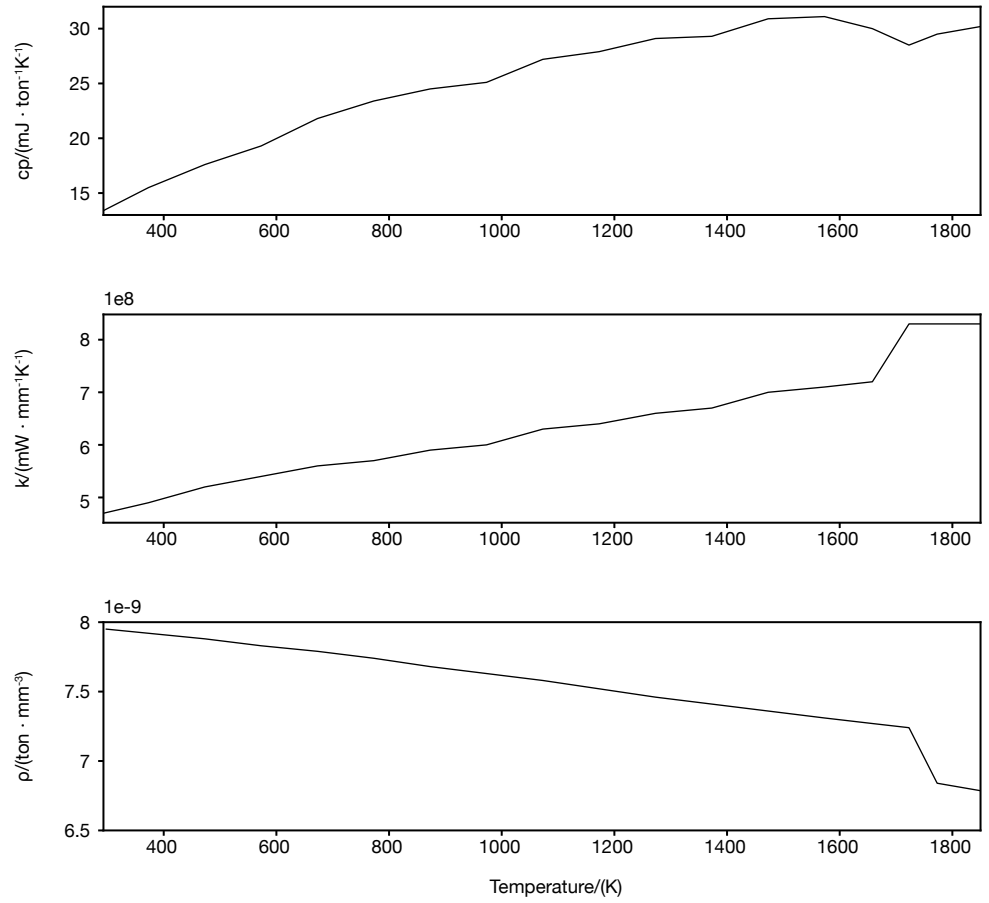

Fig. 7.2 Thermal properties of 316L as a function of the temperature.

7.3.3 Boundary Conditions

As previously outlined, the selection of the most appropriate boundary conditions can have a substantial impact on the accuracy of the model, and must be performed considering the physic phenomenon to be modelled. It might be useful to recall that the system model previously described is not an isolated system. Consequently,

it exchanges energy with the surrounding environment, primarily in the form of thermal energy, through conduction, convection and radiation.

Conduction

Starting from the heat exchanged by conduction between the system and the surroundings, no conductive heat transfer was included in the model. The decision of excluding the contribution of conduction between the platform and the roto-tiling table of the machine was primarily driven by the higher computational expense that would have resulted by incorporating of the roto-tilting table into the model.

Convection

It is of great importance to correctly model the convective heat exchange between the system and the surrounding environment. Equation 7.4 already presented the convective heat transfer across the boundary of a system as a particular instance of the Robin boundary condition. Another possible representation of the convection equation is provided by Equation 7.6, which is typically implemented in numerical simulations:

$$\dot{q} = h(T_\infty - T(t,x)) \tag{7.6}$$

where h is the convective heat transfer coefficient, whose value is usually used to distinguish between natural and forced convection. Low h values refer to natural convection, whereas high h values are typical of forced convection. Accordingly, a clear distinction was made in the model between surfaces subjected to natural convection and surfaces subjected to forced convection. Figure 7.3 shows the surfaces on which the two different conditions were applied. Natural convection was applied to all the free surfaces of the system that were not directly interested by the LP treatment. Consequently, the only surface interested by forced convection was the upper surface of the sample, the one actually undergoing the LP treatment and protected by the shielding gas flow rate. The convective heat transfer coefficients for both natural and forced convection are reported in Table 7.1.

However, during LP treatments the forced convection does not exert an influence on the whole upper surface simultaneously. Given the intrinsic relationship between

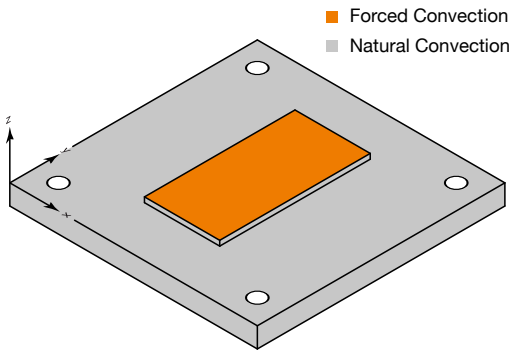

Fig. 7.3 Surfaces subjected to natural convection and to force convection.

forced convection and the shielding gas flow rate, and therefore with the position of the laser beam, it is essential to apply a varying convection boundary condition on the upper surface, in accordance with the actual motion of the laser beam throughout the LP treatment. Abaqus provides the possibility of implementing variable convective heat transfer conditions during the simulation step. Accordingly, the FILM subroutine was employed to impose a force convection coefficient within a radius of 4 mm from the centre of the laser beam, as reported in Annex B. In order to prevent an abrupt transition in the value of the convection coefficient, from its forced value to its natural value, the force convection coefficient was modelled as a Gaussian curve. The maximum value of the Gaussian curve was set equal to the force convection coefficient, namely $0.1\,\mathrm{mW\,mm^{-2}\,K^{-1}}$, while its value at a distance of 4 mm was set equal to the natural convection coefficient, namely $0.02\,\mathrm{mW\,mm^{-2}\,K^{-1}}$. This approach ensures a continuous and smooth transition between the two regimes.

Table 7.1 Coefficients required by Abaqus CAE for correctly modelling the heat transfer boundary conditions.

Natural Convection Coefficient $\left(\mathrm{mW\,mm^{-2}\,K^{-1}}\right)$	Forced Convection Coefficient $\left(\mathrm{mW\,mm^{-2}\,K^{-1}}\right)$	Absorbivity (-)	Emissivity (-)
0.02	0.1	0.32	0.6

Radiation

Radiative heat exchange does not require the presence of a medium for the transfer of thermal energy between the system and its surrounding environment. The efficacy of radiation heat exchanges only depends on the absolute temperatures of the system and its surroundings, as explained by the Stefan-Boltzmann Equation:

$$\dot{q} = \varepsilon\sigma\left(T^4(t,x) - T_\infty^4\right) \tag{7.7}$$

where ε represents the emissivity of the system, while σ denotes the Stefan-Boltzmann constant. Since the radiation heat flux is proportional to the fourth power of the temperature of the body, its contribution is negligible in close proximity to the temperature of the surroundings, and becomes more significant at high temperature values. If σ is a constant with a value that is uniquely defined in the literature, the definition of the emissivity of a system is consistently more complex, and typically require the use of thermocouples and infrared cameras. The emissivity is defined as the amount of radiation emitted by a body as thermal radiation. The value of the emissivity is strongly dependent upon the material considered, its optical properties, and its temperature. In order to provide a simplified description of the phenomenon, a constant value of emissivity equal to 0.6 was incorporated into the model, as reported in Table 7.1. The radiation boundary condition was applied to all the free surfaces of the geometry.

Heat Source

The mathematical description of the heat source is of primary importance for the successful modelling of LP treatments. Firstly, it should be noted that laser sources can be represented both as body heat sources and as surface heat sources. When the laser is modelled as a body heat source, it enters the heat conduction equation via the Γ term, which is the right-hand side of Equation 7.1. Conversely, if the laser is modelled as a surface heat source it enters the equation as a special case of the Neuman boundary condition, as it imposes a constant value of heat flux across the model boundary. For instance, when modelling the deposition of new material during DED-LB processes, it is common practice to use a body heat source for representing the role of the laser [116, 171]. In the context of DED-LB processes, the elements of

the model mesh are progressively activated to mimic the deposition itself. After the completion of a layer, the processes continues with the deposition of the following one, involving a constant change of the surface exposed to the laser. This renders the application of the heat source to the surface of the sample an extremely complex and computationally expensive process. Therefore, the laser source is typically modelled as a volumetric heat source. It is essential to accurately define the depth of the volume defining the body heat flux, which is typically guided by previous experimental results.

However, LP treatments do not involve the activation of new elements throughout the process, exposing the same surface to the laser source. This LP feature allows for the straightforward modelling of the laser source as a surface heat flux, with a closer resemblance to the real-case scenario. Further attention should also be paid to the definition of the laser intensity distribution on the irradiated surface. Previous experimental investigations have demonstrated that the lasers used in DED systems can be represented by top-hat distributions in their focal planes [172], as schematically represented in Figure 7.4. A top-hat distribution implies a nearly constant power within the radius of the laser spot, with an abrupt decrease in power outside of it.

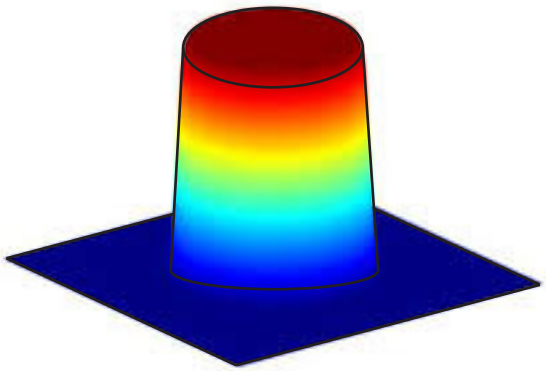

Fig. 7.4 Cylindrical laser distribution.

In conclusion, the current work modelled the laser as a surface heat source applied on the upper surface of the geometry, and distributed according to a top-hat distribution within the beam diameter. However, as for the convective heat transfer

coefficient, the heat flux on the upper surface of the geometry strongly depends upon the position of the laser beam itself. Once more, Abaqus provides the DFLUX subroutine, which has been specifically introduced to simulate moving heat sources, as outlined in the Annex B [173]. The DFLUX subroutine allows for the definition of a moving heat source, whose intensity depends upon position and time, as described in Equation 7.8.

$$I(r,t) = \begin{cases} \frac{P}{\pi \cdot r_l^2} & if \quad r \leq r_l \\ 0 & if \quad r > r_l \end{cases} \tag{7.8}$$

7.3.4 Initial Conditions

As with boundary condition, the initial conditions are a fundamental component of the solution of any differential equation. In the absence of information regarding the initial state of the system, it is not possible for the numerical model to make any predictions regarding the effect of the subsequent thermal treatment. It is reasonable to assume that the temperature of the entire system would be uniform prior to the start of the LP treatment. Accordingly, the temperature of the system was set to 25 °C.

7.3.5 Model Mesh

The size of the mesh used for the discretisation of the model is another crucial factor that heavily impacts the accuracy of the results. In certain instances, the use of coarse meshes may be advantageous, as they facilitate rapid results at a reduced computational cost. However, the utilisation of excessively coarse meshes may result in the generation of erroneous or inaccurate outcomes. Conversely, more refined discretizations typically results in more accurate numerical solutions, at a cost of a greater computational efforts. Therefore, the objective of a mesh convergence analysis is the definition of the optimal mesh size, ensuring the most effective trade-off between the desired level of accuracy and the required computational resources. In the context of mechanical FE simulations, mesh convergence analyses progressively reduce the element size, with concurrent monitoring of the displacement of a specific point within the model. The reduction of the average element size implies an increase

in the number of elements, which in turn lead to an increase in the compliance of the model. Consequently, the increase in the number of elements results in a progressive increase in the displacement of the monitored point. The procedure is stopped when a further reduction of the mesh size does not result in a significant change in the displacement of the point.

In the context of thermal transient simulations, such as LP simulations, defining a suitable response to monitor while simultaneously reducing the element size can be more challenging than in the case of mechanical FE simulations. This more complex scenario has compelled experimenters to get more creative and to identify alternative methods for conducting mesh convergence analyses in thermal simulations. For instance, Soffel et al. [166] used the temperature profiles within the heat source centre for their mesh convergence analysis, with the objective of obtaining a smooth description of the shape of the heat source itself. Using a different approach, Mohajerani et al. [162] monitored the temperature profile along the longitudinal axis of the polished track, reducing the mesh size until no significant differences were observed. Both this strategies are worth considering to define the dimensions of mesh elements in the xy plane, which represents the superior surface of the sample. However, it is essential to incorporate the necessity of adjusting the dimension of the mesh element along the z-direction, which is the direction in which the laser source is applied.

In the present investigation, both approaches were applied simultaneously to analyse the convergence of the mesh in all three dimensions. Moreover, in order to reduce the time required, the mesh convergence analysis was performed on single LP tracks. Figure 7.5 displays the results of the aforementioned mesh convergence analyses. Five mesh sizes were investigated, starting from 1 mm down to 0.05 mm. Figure 7.5.A depicts the temperature profiles computed along the axis of the polishing track, namely the y direction. The use of extremely coarse meshes, comprising 1 mm and 0.5 mm elements, resulted in a poor description of temperature profiles, which tended to sensibly overestimate the maximum temperature reached. Conversely, the 0.25 mm and, even more so, the 0.10 mm meshes were able to properly describe the temperature evolution along the polishing track, without the occurrence of any sharp temperature transitions. The finest mesh, comprising 0.05 mm elements, did not reveal significant differences in comparison to the 0.10 mm one. Therefore,the 0.25 mm solution was considered the optimal compromise between precision and computational cost. Similar trends can be observed in Figure 7.5.B, where the

Table 7.2 Coefficients required by Abaqus for an automatic time increment management.

Step Time (s)	Maximum Number of Increments (-)	Initial Increment (s)	Minimum Increment (s)	Maximum Increment (s)	Maximum Temp. Change per Increment (°C)
157.35	100 000	0.001	3.26e-5	1	5000

temperature profiles are crossing the laser spot along the x direction. The 0.25 mm elements mesh resulted in an adequate description of the temperature profile, suggesting no need for finer element meshes along the x direction Finally, the same procedure was also conducted below the LPed surface, namely along the z direction. In this case, the temperature profiles were extremely close to one another and did not result in significant temperature changes below the 0.25 mm threshold.

7.3.6 Time Increment

The final aspect of the numerical model that requires clarification pertains to the selection of the time increment employed. At this juncture, Abaqus presented the option of opting for a variable time increment, automatically varied to ensure the convergence of the model. Table 7.2 collects the coefficients used during the this delicate phase. Consequently, as Abaqus itself varied the time increments to ensure the convergence of the method, no convergence analysis was performed regarding the time discretisation.

7.4 Experimental Validation of the Model

The numerical model presented in the previous section had to be validated against experimental evidence. There are multiple approaches that could be employed to validate a thermal model. At first, the model could be used to ascertain the geometrical features of remelted tracks, specifically their depth and width. Accordingly, this option requires the micrographic analysis of the sections of the LP samples, which could be a long and intricate procedure. A second option involves the comparison between the temperatures computed by the numerical model and some experimen-

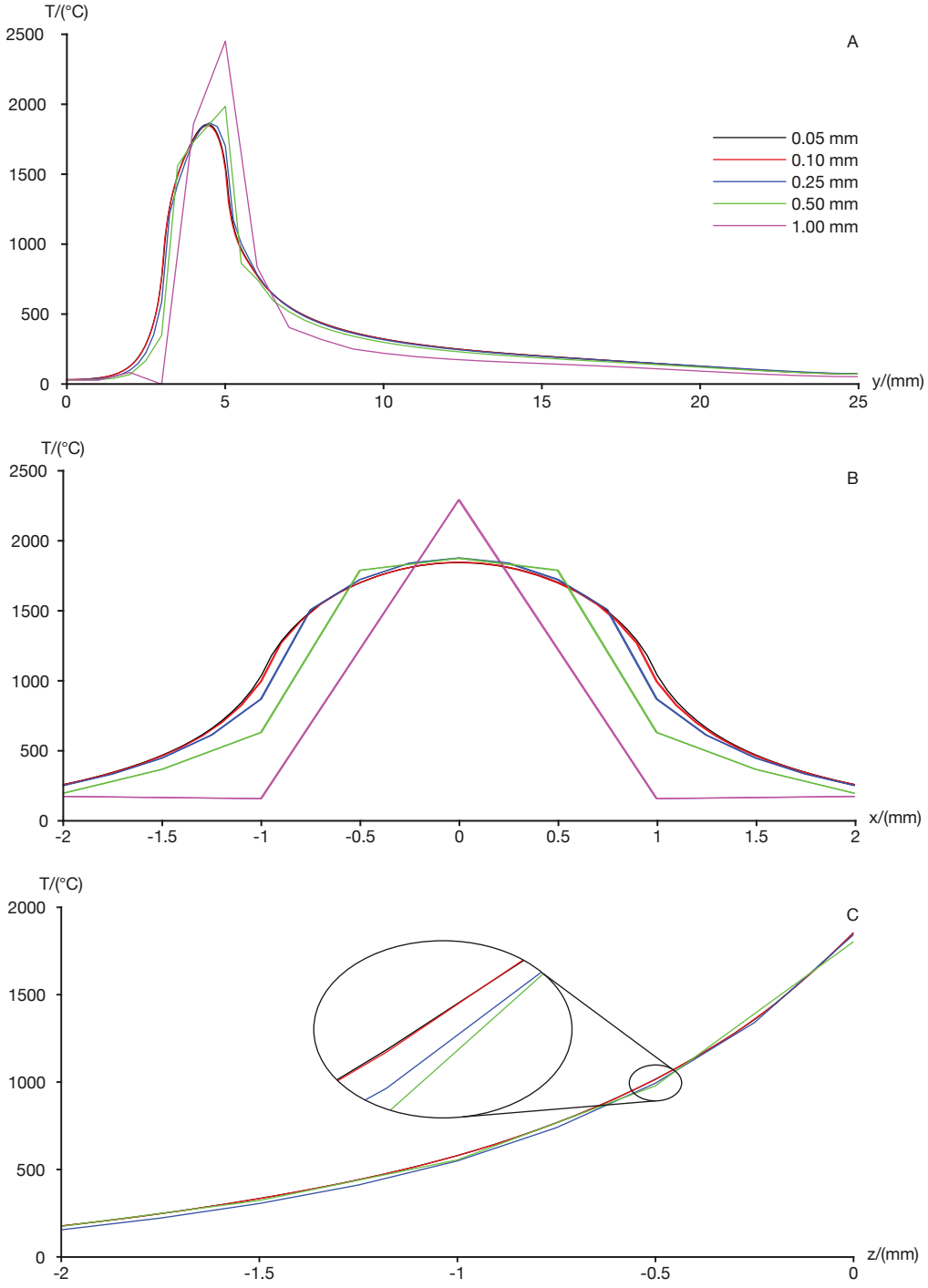

Fig. 7.5 Temperature profile used for the mesh convergence analysis: A) along the polishing track middle line; B) temperature profile of the heat source; C) temperature profile below the LPed surface.

tally measured data at predefined locations. In this scenario, thermocouples may be used to perform the empirical measurement of the temperature reached during the LP treatment. This second option presents several consistent advantages over the first proposed one, primarily related to the ease and speed of implementation. Therefore, the current section presents the quantification of the accuracy of the model, tested against empirical data acquired using thermocouples.

7.4.1 Working Principle of Thermocouples

Thermocouples are measuring instruments that are widely used in industry for temperature measurement, primarily due to their robustness and cost-effectiveness. The operational principle of the thermocouples is based upon the Seebeck effect, which states that the existence of a temperature difference between the exposed ends of an electrical circuit induces an electromotive force within the circuit. The functional relationship between temperature difference and voltage is described by Equation 7.9:

$$V = S(T_1 - T_0) \tag{7.9}$$

where S is the Seebeck coefficient ($\mu V\,^{\circ}C^{-1}$) which depends on the physical properties of the material. If two wires of differing materials are employed to delineate the electrical circuit, designated as A and B, the net electromotive force generated within the circuit will be equal to the sum of the individual electromotive forces produced by each wire, as described in Equation 7.10. By rearranging the terms on the right-hand side of Equation 7.10, Equation 7.11 can be obtained with ease. Equation 7.11 is the fundamental relation in thermocouple thermometry, as it relates the temperature differences between the junctions of the two wires to the electromotive force.

$$V = S_A(T_1 - T_0) + S_B(T_0 - T_1) \tag{7.10}$$

$$V = S_A(T_1 - T_0) - S_B(T_1 - T_0) = (S_A - S_B)(T_1 - T_0) = S_{AB}(T_1 - T_0) \tag{7.11}$$

In a real case scenario, the value of V is measured using a voltmeter and the temperature T_0 is measured using a third measurement device. This way, knowing the value of S_{AB} for the specific material combination of the thermocouple it is possible to compute the value of T_1 by simply reversing Equation 7.11. However, the functional relation between V and T is typically nonlinear, as described in Equation 7.12.

$$T = a_0 + a_1 V + a_2 V^2 \dots a_n V^n \tag{7.12}$$

Companies that manufacture thermocouples typically provide tables containing the coefficients a_0, a_1, ..., a_N, allowing the construction of the curve representing the temperature as a function of the voltage.

7.4.2 Experimental Equipment

This subsection outlines the experimental equipment used for in-line temperature monitoring during LP treatments. The selected platform has dimensions of $(100 \times 100 \times 8)$ mm^3, consistent with the geometry modelled for the numerical model presented in 6.3. A substrate measuring $(60 \times 30 \times 2)$ mm^3 was deposited on top of the platform, again for close resemblance to the numerical model. The platform and the substrate were realised in 316L. The thermocouples employed in the investigation were the GG-K-30-SLE thermocouples, produced by Omega (Norwalk, CT, USA). The GG-K-30-SLE thermocouples have a maximum working temperature of 482 °C with a tolerance of 1.1 °C, or the 0.4% of the measure temperature. The identifier of the thermocouple contains significant information:

- The first two letters refer to the insulating material employed for the thermocouples. The double G indicates the use of fibreglass for the insulation of the single metallic wires, and for the outer envelope which collects the two metallic wires.
- The third letter refers to the combination of metals used for the two metallic wires. The K indicates the use of chromel® and alumel®, nickel-based alloys that are registered trademarks of Concept Alloys Inc. (Whitmore Lake, MI, USA).

- The numerical value represents the gauge of the metallic wires, in accordance with the American Wire Gauge (AWG) system, as described in the ASTM B258-18 [174] standard. AWG equal to 30 signifies a wire diameter of 0.254 mm.
- Finally, the acronym SLE stands for *Specific Limit Error* and indicates a higher accuracy of the thermocouple, as previously documented in relation to its tolerance.

Therefore, four thermocouples were spot welded on the platform, in accordance with the positions reported in Figure 7.6. Three thermocouples were welded on the upper surface of the platform, whereas the fourth thermocouple, thermocouple D in Figure 7.6, was welded on the rear of the platform, directly behind the planned LPed area. Figure 7.6 also highlights the raster strategy used for the LP operation.

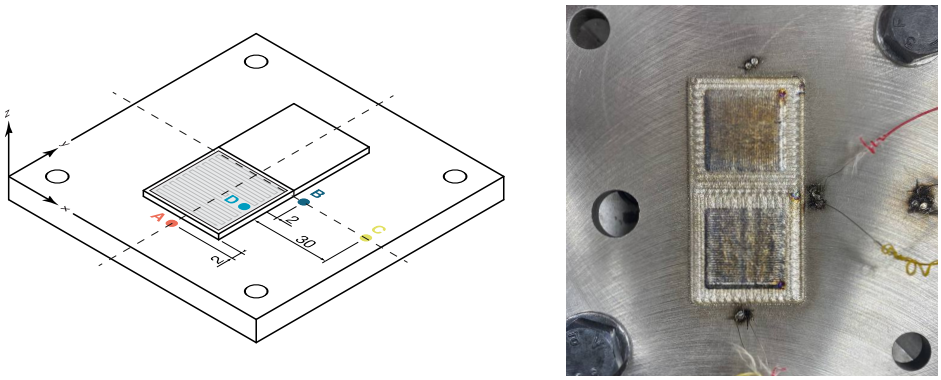

Fig. 7.6 Thermocouples placement for measuring temperatures LP treatments.

The SCM-TCK adaptor, manufactured by HBM, was employed to bridge the signal passage between the thermocouples and the QuantumX 440, which was previously presented in the context of residual stress measurement in Chapter 5. Additionally, the SCM-TCK adaptor converted the tension signal into a temperature signal, using settings tailored to K thermocouples. The Quantum X sampled the signals at a frequency of 100 Hz, with the objective of reducing their dimensions. The signals were then acquired using LabVIEW, a software developed by National Instruments (Austin, TX, USA). The interface between the QuantumX and LabVIEW was managed by specific drivers provided by the same National Instruments.

7.4.3 Comparison of Numerical and Experimental Data

Figure 7.7 depicts the curves of the temperatures reached during the LP treatment in the four locations highlighted in Figure 7.6. More in detail, solid lines refers to temperature measurement performed by thermocouples, whereas dashed lines refers to the temperature profiles computed by Abaqus. Various considerations could be done on the basis of the information provided by Figure 7.7. At first, the temperature profiles computed by Abaqus tend to overestimate the temperature measured by the thermocouples. This common trend can be observed for thermocouples A, B and C, all placed on the upper surface of the platform. However, the curve related to thermocouple D presents a different behaviour as the numerical outcomes slightly underestimate empirical values.

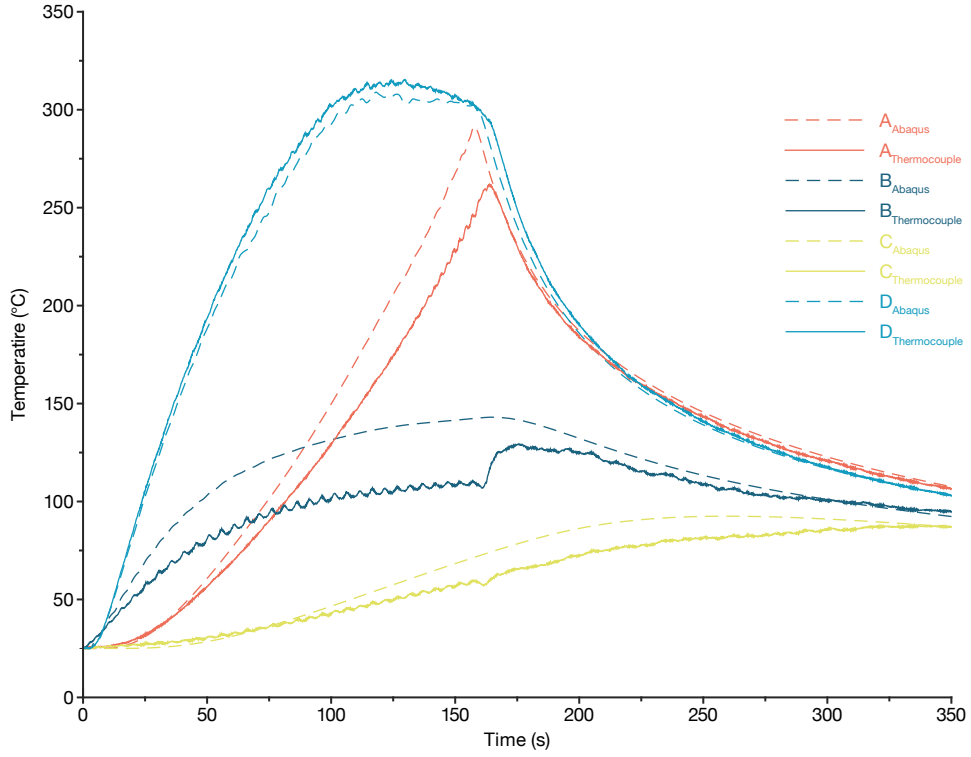

Fig. 7.7 Comparison between experimental data from thermocouples (solid lines) and numerical data computed using Abaqus (dashed lines).

Starting from thermocouple A, Abaqus predicted a maximum temperature close to 290 °C, in front of a measured temperature of 261 °C, with a prediction error equal to the 11.5% of the measured value. Moreover, it is interesting to notice that the

error primarily interests the time interval of the proper LP treatment, whereas the behaviour of the subsequent following phase is more closely predicted.

At location B, Abaqus incurred in the largest prediction error, around 33% of the measured value. In this case, the prediction error does not solely affect the maximum predicted temperature as the entire temperature curve is notably overestimating the temperature measured by the thermocouple. A closer look at the temperature curve measured by the thermocouple reveals several local temperature peaks and a base temperature increase. Moreover, the thermocouple registered an unexpected raise in temperature at the end of the LP treatment, clearly visible from the corresponding curve. These features were not predicted by Abaqus, which conversely resulted in smoother curve, free of sudden temperature changes. Also in this case, Abaqus was able to model the subsequent cooling phase with good precision.

Location C was the furthest from the LPed area, datum that is reflected by the lower temperatures measured by the thermocouple. The features that characterise the temperature curve are in close resemblance to the features already discussed at location B. A monotonically increasing temperature signal was superimposed with a periodic signal, representing the cyclic approaches and departures of the laser to the location of measurement. This time, the temperature peaks were less pronounced due to the greater distance between the location of the measurement and the LPed area. However, in this case Abaqus provided a better estimate than the one provided for location B, namely the maximum error was equal to the 15% of the value measured by the thermocouple.

Finally, location D, the only one on the back of the platform, was the only location where the model provided a very accurate prediction of the experimental results. Here, the maximum prediction error was slightly lower than the 4% of the experimental value, certifying the goodness of the results. The higher accuracy of the model at location D could be most probably related the closer resemblance of the modelled heat convection to the real occurring heat exchange. This insight indicates that different heat convection conditions might be more adequate on different surfaces of the model. Accordingly, more advanced versions of the numerical model here outlined should also impose different heat convection coefficients between the surfaces not directly interested by the laser beam.

7.5 Conclusions

Numerical simulations represent the state-of-the-art solution for understanding the temperature distribution during thermal processes such as laser polishing. After the experimental campaign presented in the previous chapters, this chapter outlined the nucleus of a numerical model to predict the temperatures reached in the substrate during LP treatments. The conclusions that were drawn were here reported for the sake of the reader:

- Abaqus, a general purpose FE software, was employed for simulating the LP treatments, avoiding any commercial solution tailored for the case. It was able to simulate the moving heat source and the varying heat convection coefficient in Abaqus by using the subroutines DFLUX and FILM respectively;
- the proposed model was a pure-conductive thermal model, that only focused on the computation of the temperature map. Despite the simplicity of the model, the predicted temperatures were still relatively accurate, being close to the experimental results measured using thermocouples;
- the accuracy of the results was strongly dependent on the considered location onto the platform. On the back of the platform the model resulted in a optimal temperature prediction, with minimal error equal to the 4% of the measure value, whereas on other locations the predicted temperature overshooted the measured one by a third, around 34% of the measured value. This is a clear signal that the boundary condition imposed in the model should be further refined for an improved representation of the real heat exchange mechanisms between the substrate and the surroundings.

Future activities on the model should focus on improving the accuracy of the model by refining the exchange mechanisms between system and environment, and on performing thermo-mechanical simulations, being able to predict also the residual stress state induced by the LP treatment.

Chapter 8

Conclusions and Future Outlooks

Directed Energy Deposition is a family of industrial processes with a rapidly growing market. Directed Energy Deposition can be employed to build metallic components from scratch, repair expensive components, deposit additional features on already existing components, and also for cladding operations. However, a widespread adoption of Directed Energy Deposition in the manufacturing sector is still hindered by various limitations, one of which is the poor surface quality of deposited components. The problem of the poor surface quality in deposited components is typically addressed through the adoption of finishing processes subsequent to the deposition phase. In this context, mechanical finishing processes are the most commonly used, as they allow the removal of the outermost deposited layer, resulting in optimal surface quality in terms of both roughness and waviness. However, mechanical finishing processes may prove to be challenging when used on components deposited by Directed Energy Deposition. Since the components deposited by Directed Energy Deposition typically exhibit higher mechanical strength, they often require higher cutting forces and powers, induce a faster wear of the tool, and may present difficulties in accessing the finishing area due to the encumbrance of the same tool.

Therefore, the objective of this thesis was to investigate the potential of utilising a laser source for the finishing of components deposited by Directed Energy Deposition. Laser Polishing does not require the presence of any physical tool, resolving the issues related to cutting forces, tool wear and accessibility. Moreover, in a Directed

Energy Deposition system the same laser beam could be employed for both the deposition and finishing stages, with potential savings in terms of cost of the required equipment. Chapter 1 presented the research questions that this work was meant to address. In this final chapter, the answers to these questions were eventually articulated, with additional care for the future outlooks of the work.

RQ1: Can a comprehensive experimental campaign lead to a robust empirical model, helping to predict the resulting surface roughness of future laser polishing treatments?

The initial part of this work comprised an extensive experimental campaign, primarily devoted to the definition of an empirical model for predicting the outcomes of LP treatments. Two models were derived from the optimisation campaign: the Ra model and the Wa model. The Ra model was able to correctly predict the location of the Ra minimum, close to 2 µm. This claim was subsequently validated by additional empirical evidence. Conversely, the Wa model did not provide the same level of accuracy but was still helpful in defining the potential areas of Wa minimum location. In summary, it can be confidently asserted that the empirical model defined in this work, despite its limitations, can be profitably used to predict the outcome of LP operations.

RQ2: Are the collateral effects of laser polishing treatments acceptable? Could laser polishing lead to unexpected improvements of material characteristics?

Laser Polishing inevitably leads to collateral effects in the substrate undergoing the treatment. In this work, particular attention was paid to the residual stress state induced in the substrate and to microindentation hardness alterations. In was found that the residual stresses induced by Laser Polishing are independent of the energy employed, within the limits of the investigated domain. After Laser Polishing, the residual stresses exhibited higher tensile values in the sub-superficial region, close to 200 MPa, compared to those observed in as-built components. However, the differences in residual stress states between the finished and as-built components became almost negligible already at a depth of 0.4 mm. It was therefore concluded that the Laser Polishing treatments did not significantly alter the residual stress state of the samples deposited by Directed Energy Deposition. Microindentation hardness tests highlighted the influence of different LEDs on the hardness values measured on

the cross sections of the substrates. LP treatments performed with energies lower than the ones used during the deposition phase could bring to lower microindentation hardness values. Conversely, if the energy used through the LP treatment is significantly higher than the one used for deposition, the final microindentation hardness values could also be lower than in the as-built condition. Therefore, it should be safe to state the necessity of subsequent heat treatments to relief the induced residual stresses and act on the microstructure of the substrate, if needed. Accordingly, the same stress relief heat treatments are expected to successfully distend also the sub-superficial tensile stresses induced by Laser Polishing treatments. Moreover, shot peening treatments could be also considered following the Laser Polishing ones. This could be a highly beneficial approach in contexts where compressive residual stresses are desired in the sub-superficial region, with the aim of improving the fatigue life of Laser Polished components.

RQ3: Can a numerical model help the understanding of the temperature distribution inside the sample during laser polishing treatments?

The numerical model outlined in the final chapter of this work was helpful in providing both qualitative and quantitative information about the temperatures reached by the substrate during Laser Polishing treatments. The numerical simulations were able to predict the temperatures reached at different locations of the substrate with an acceptable degree of accuracy, with a minimum discrepancy of 4% from the experimentally measured value. Additional attention should be paid to further refinements of the model, improving the modelling of the heat exchange between the system and the environment, and implementing the mechanical behaviour of the system in the model. An accurate thermomechanical model could be used to predict the depth of the remelted layer, the depth of the eventual heat-affected zone and the residual stresses induced in the substrate.

RQ4: What is the real industrial potential of Laser Polishing? In which context could Laser Polishing be profitably used?

As previously asserted, the good quality of the surfaces that underwent laser polishing treatments must be further discussed to understand their possible industrial applications. An Ra value between 2 to 3 µm is comparable to roughing machining operations, not too far from the threshold of 1 µm of finishing machining operations.

Moreover, also the Wa value around 9 µm must be considered to correctly understand the potential uses of Laser Polishing on an industrial scale. As previously outline in Figure 2.7, in Section 2.3, contained roughness values and high waviness values are acceptable for independent surfaces and in mating surfaces without relative displacement, particularly in the absence of sealing requirements. Conversely, the use of Laser Polishing for finishing surfaces with relative displacement, with or without lubrication, remains outside of the possible field of applications, especially given the current limitations in surface waviness. In this context, two main strategies could be adopted to further improve the quality of the resulting surfaces and reach the threshold of Ra equal to 1 µm, while also sensibly reducing surface waviness. A first potential solution is to perform a second laser polishing treatment with different process parameters. The optimal set of process parameters identified during the experimental campaign involved a significant quantity of thermal energy to remelt the uppermost deposited layer, which was still in the as-built condition. A second Laser Polishing phase, performed with a reduced thermal energy input, could further smooth the surface and improve its quality. The solution presented above is consistent with most finishing processes, in which the roughing phases and the subsequent finishing phases are performed using different process parameters, as in the aforementioned case of milling processes. A second potential solution to further improve the final quality of the deposited surface could be the introduction of an additional finishing operation different from the Laser Polishing one. At the beginning of this investigation, Laser Polishing was selected over other finishing techniques since it could be performed using the same laser that is used for the deposition. This approach reduces the need for additional instrumentation, such as 5-axis milling machines, with potential savings across the entire manufacturing chain. Therefore, the idea of introducing additional machinery appears to be in contrast with the fundamental objective of the work. However, some of the finishing techniques presented in Chapter 2 may still be worthy of consideration due to their simplicity and relatively low cost. For instance, barrel finishing and vibro finishing could be considered for the scope as they require minimal training of the operator and are available at a limited initial cost. Therefore, the introduction of a barrel finishing phase subsequent to the Laser Polishing one could potentially improve the quality of the surface without an excessive impact on the final cost of the component.

References

[1] ASTM international. *Additive manufacturing – General principles – Fundamentals and vocabulary*. en. Standard ISO/ASTM 52900:2021. West Conshohocken, PA, 2021.

[2] Ciraud Leone. *Concentrated beam particle melting - at focal point of several beams*. French patent FR2166526A5. Dec. 1971.

[3] Baker Ralph. *Method of making decorative articles*. US Patent 1,533,300. Apr. 1925.

[4] JJ Beaman et al. "Additive manufacturing review: Early past to current practice". In: *Journal of Manufacturing Science and Engineering* 142.11 (2020), p. 110812.

[5] Terry Wohlers et al. "History of additive manufacturing". In: (2016).

[6] Carlos MS Vicente et al. "Large-format additive manufacturing of polymer extrusion-based deposition systems: review and applications". In: *Progress in Additive Manufacturing* (2023), pp. 1–24.

[7] Pouya Moghimian et al. "Emerging functional metals in additive manufacturing". In: *Advanced Engineering Materials* (2023), p. 2201800.

[8] Jinxing Sun et al. "A review on additive manufacturing of ceramic matrix composites". In: *Journal of Materials Science & Technology* 138 (2023), pp. 1–16.

[9] Kumar Kanishka and Bappa Acherjee. "Revolutionizing manufacturing: A comprehensive overview of additive manufacturing processes, materials, developments, and challenges". In: *Journal of Manufacturing Processes* 107 (2023), pp. 574–619.

[10] Ismail Fidan et al. "Recent inventions in additive manufacturing: Holistic review". In: *Inventions* 8.4 (2023), p. 103.

[11] Ageel Abdulaziz Alogla, Ateyah Alzahrani, and Ahmad Alghamdi. "The Role of Additive Manufacturing in Reducing Demand Volatility in Aerospace: A Conceptual Framework". In: *Aerospace* 10.4 (2023), p. 381.

[12] Zia Ullah Arif et al. "Additive manufacturing of sustainable biomaterials for biomedical applications". In: *Asian Journal of Pharmaceutical Sciences* (2023), p. 100812.

[13] Rishi Parvanda and Prateek Kala. “Trends, opportunities, and challenges in the integration of the additive manufacturing with Industry 4.0”. In: *Progress in Additive Manufacturing* 8.3 (2023), pp. 587–614.

[14] Flaviana Calignano and Vincenza Mercurio. “An overview of the impact of additive manufacturing on supply chain, reshoring, and sustainability”. In: *Cleaner Logistics and Supply Chain* 7 (2023), p. 100103.

[15] Mohammadreza Akbari. “Data-driven review of additive manufacturing on supply chains: Regionalization, key research themes and future directions”. In: *Computers & Industrial Engineering* 184 (2023), p. 109600.

[16] Ifeyinwa Juliet Orji and Frank Ojadi. “Assessing the effect of supply chain collaboration on the critical barriers to additive manufacturing implementation in supply chains”. In: *Journal of Engineering and Technology Management* 68 (2023), p. 101749.

[17] Gabriele Piscopo et al. “An overview of the process mechanisms in the laser powder directed energy deposition”. In: *Applied Sciences* 13.1 (2022), p. 117.

[18] David Svetlizky et al. “Directed energy deposition (DED) additive manufacturing: Physical characteristics, defects, challenges and applications”. In: *Materials Today* 49 (2021), pp. 271–295.

[19] Ian Gibson Ian Gibson. *Additive manufacturing technologies 3D printing, rapid prototyping, and direct digital manufacturing*. 2015.

[20] Gabriele Piscopo and Luca Iuliano. “Current research and industrial application of laser powder directed energy deposition”. In: *The International Journal of Advanced Manufacturing Technology* 119.11-12 (2022), pp. 6893–6917.

[21] Sciaky INC. https://www.sciaky.com/largest-metal-3d-printer-available. Accessed: 6th of March 2024.

[22] Jibing Wang et al. “A comparative study of Cu–15Ni–8Sn alloy prepared by L-DED and L-PBF: Microstructure and properties”. In: *Materials Science and Engineering: A* 840 (2022), p. 142934.

[23] Farzaneh Kaji et al. “Robotic laser directed energy deposition-based additive manufacturing of tubular components with variable overhang angles: Adaptive trajectory planning and characterization”. In: *Additive Manufacturing* 61 (2023), p. 103366.

[24] Abdollah Saboori et al. “Application of directed energy deposition-based additive manufacturing in repair”. In: *Applied Sciences* 9.16 (2019), p. 3316.

[25] Maija Leino, Joonas Pekkarinen, and Risto Soukka. “The role of laser additive manufacturing methods of metals in repair, refurbishment and remanufacturing–enabling circular economy”. In: *Physics Procedia* 83 (2016), pp. 752–760.

[26] Rolf Steinhilper and Ulrike Hudelmaier. “Erfolgreiches Produktrecycling zur erneuten Verwendung oder Verwertung: ein Leitfaden für Unternehmer”. In: *(No Title)* (1993).

[27] Johan Vogt Duberg, Erik Sundin, and Ou Tang. "Assessing the profitability of remanufacturing initiation: a literature review". In: *Journal of Remanufacturing* (2023), pp. 1–24.

[28] Ali Nikseresht, Davood Golmohammadi, and Mostafa Zandieh. "Sustainable green logistics and remanufacturing: A bibliometric analysis and future research directions". In: *The International Journal of Logistics Management* (2023).

[29] Ajay K Sinha and P Hanumantha Rao. "Integration of Lean Techniques with Remanufacturing Operations for Process Improvement". In: *Materials Today: Proceedings* (2023).

[30] United Nations (UN). *Transforming Our World: The 2030 Agenda for Sustainable Development.* https://sdgs.un.org/2030agenda. 2015.

[31] Sajjad Barzegar-Mohammadi et al. "Effects of TIG dressing, PWHT and temper bead techniques on microstructure and fatigue strength of fillet welded steel patch repairs: an experimental investigation". In: *Journal of Materials Research and Technology* 22 (2023), pp. 3442–3462.

[32] N Jeyaprakash, Adisu Haile, and M Arunprasath. "The parameters and equipments used in TIG welding: A review". In: *The International Journal of Engineering and Science (IJES)* 4.2 (2015), pp. 11–20.

[33] Amirhossein Mashhuriazar et al. "Investigating the effects of repair welding on microstructure, mechanical properties, and corrosion behavior of IN-939 superalloy". In: *Journal of Materials Engineering and Performance* 32.15 (2023), pp. 7016–7028.

[34] Jennifer Bennett et al. "Repairing automotive dies with directed energy deposition: industrial application and life cycle analysis". In: *Journal of Manufacturing Science and Engineering* 141.2 (2019), p. 021019.

[35] J Michael Wilson et al. "Remanufacturing of turbine blades by laser direct deposition with its energy and environmental impact analysis". In: *Journal of Cleaner Production* 80 (2014), pp. 170–178.

[36] Joana R Gouveia et al. "Life cycle assessment and cost analysis of additive manufacturing repair processes in the mold industry". In: *Sustainability* 14.4 (2022), p. 2105.

[37] Matthieu Rauch, Jean-Yves Hascoët, and Manjaiah Mallaiah. "Repairing Ti-6Al-4V aeronautical components with DED additive manufacturing". In: *MATEC Web of Conferences*. Vol. 321. EDP Sciences. 2020, p. 03017.

[38] Wook Jin Oh et al. "Repairing additive-manufactured 316L stainless steel using direct energy deposition". In: *Optics & Laser Technology* 117 (2019), pp. 6–17.

[39] Wook Jin Oh, Yong Son, and Shim Do Sik. "Effect of in-situ heat treatments on deposition characteristics and mechanical properties for repairs using laser melting deposition". In: *Journal of Manufacturing Processes* 58 (2020), pp. 1019–1033.

[40] Michael Liu et al. “A review of the anomalies in directed energy deposition (DED) processes & potential solutions-part quality & defects”. In: *Procedia Manufacturing* 53 (2021), pp. 507–518.

[41] Mojtaba Izadi et al. “A review of laser engineered net shaping (LENS) build and process parameters of metallic parts”. In: *Rapid prototyping journal* 26.6 (2020), pp. 1059–1078.

[42] Gabriele Piscopo, Alessandro Salmi, and Eleonora Atzeni. “Investigation of dimensional and geometrical tolerances of laser powder directed energy deposition process”. In: *Precision Engineering* 85 (2024), pp. 217–225.

[43] Youyu Su et al. “Pore defects and corrosion behavior of AISI 316L stainless steel fabricated by laser directed energy deposition under closed-loop control”. In: *Surface and Coatings Technology* 463 (2023), p. 129527. ISSN: 0257-8972. DOI: https://doi.org/10.1016/j.surfcoat.2023.129527. URL: https://www.sciencedirect.com/science/article/pii/S025789722300302X.

[44] Eden Binega et al. “Online geometry monitoring during directed energy deposition additive manufacturing using laser line scanning”. In: *Precision Engineering* 73 (2022), pp. 104–114.

[45] Pegah Pourabdollah et al. “A novel approach for the numerical analysis of in situ distortion in a component made by the directed energy deposition additive manufacturing process”. In: *The International Journal of Advanced Manufacturing Technology* 124.5-6 (2023), pp. 1925–1938.

[46] Yunfei Huang et al. “Cracking mechanism in laser directed energy deposition of melt growth alumina/aluminum titanate ceramics”. In: *Journal of the American Ceramic Society* 106.7 (2023), pp. 4358–4370.

[47] Gabriele Piscopo, Alessandro Salmi, and Eleonora Atzeni. “Influence of high-productivity process parameters on the surface quality and residual stress state of AISI 316L components produced by directed energy deposition”. In: *Journal of Materials Engineering and Performance* 30.9 (2021), pp. 6691–6702.

[48] Gabriele Piscopo et al. “On the effect of deposition patterns on the residual stress, roughness and microstructure of AISI 316L samples produced by directed energy deposition”. In: *Progress in Digital and Physical Manufacturing: Proceedings of ProDPM’19*. Springer. 2020, pp. 206–212.

[49] Hamed Kalami and Jill Urbanic. “Exploration of surface roughness measurement solutions for additive manufactured components built by multi-axis tool paths”. In: *Additive Manufacturing* 38 (2021), p. 101822.

[50] PS Maiya and DE Busch. “Effect of surface roughness on low-cycle fatigue behavior of type 304 stainless steel”. In: *Metallurgical Transactions A* 6 (1975), pp. 1761–1766.

[51] G Nicoletto et al. “Surface roughness and directional fatigue behavior of as-built EBM and DMLS Ti6Al4V”. In: *International journal of fatigue* 116 (2018), pp. 140–148.

[52] Joy Gockel et al. “The influence of additive manufacturing processing parameters on surface roughness and fatigue life”. In: *International Journal of Fatigue* 124 (2019), pp. 380–388.

[53] Seyed Kiomars Moheimani, Luca Iuliano, and Abdollah Saboori. “The role of substrate preheating on the microstructure, roughness, and mechanical performance of AISI 316L produced by directed energy deposition additive manufacturing”. In: *The International Journal of Advanced Manufacturing Technology* 119.11 (2022), pp. 7159–7174.

[54] Kandice SB Ribeiro, Fábio E Mariani, and Reginaldo T Coelho. “A study of different deposition strategies in direct energy deposition (DED) processes”. In: *Procedia Manufacturing* 48 (2020), pp. 663–670.

[55] Renat V Gavariev and Igor A Savin. “Improvement of surface quality of casting produced by casting under pressure”. In: *Solid State Phenomena* 265 (2017), pp. 988–993.

[56] Adriaan B Spierings, Nikolaus Herres, and Gideon Levy. “Influence of the particle size distribution on surface quality and mechanical properties in AM steel parts”. In: *Rapid Prototyping Journal* 17.3 (2011), pp. 195–202.

[57] Andrew Rowe et al. “Effects of abrasive waterjet machining on the quality of the surface generated on a carbon fibre reinforced polymer composite”. In: *Machines* 11.7 (2023), p. 749.

[58] Buxin Zhang et al. “A review of surface quality control technology for robotic abrasive belt grinding of aero-engine blades”. In: *Measurement* (2023), p. 113381.

[59] Yassmin Seid Ahmed and Hoda ElMaraghy. “Offline digital twin for simulation and assessment of product surface quality”. In: *The International Journal of Advanced Manufacturing Technology* 127.5 (2023), pp. 2595–2615.

[60] ISO. *Geometric Product Specification (GPS) — Surface texture: Profile*. en. Standard ISO 21920-2:2022. Geneva, Switzerland, 2022.

[61] ISO. *Geometric Product Specification (GPS) — Surface texture: Profile method — Terms, definitions and surface texture parameters*. en. Standard ISO 4287:1998 + A1:2009. Geneva, Switzerland, 1998.

[62] M Leary. “Surface roughness optimisation for selective laser melting (SLM): accommodating relevant and irrelevant surfaces”. In: *Laser additive manufacturing*. Elsevier, 2017, pp. 99–118.

[63] ISO. *Geometric Product Specification (GPS) — Surface texture: Profile method — Motif parameters*. en. Standard ISO 12085:1997. Geneva, Switzerland, 1997.

[64] Francesco Giuseppe Biondani, Giuliano Bissacco, Lukáš Pilnỳ, et al. “Analysis and characterization of machined surfaces with aesthetic functionality”. In: *International Journal of Automation Technology* 13.2 (2019), pp. 261–269.

[65] Muhammad Arif Mahmood et al. “Post-processing techniques to enhance the quality of metallic parts produced by additive manufacturing”. In: *Metals* 12.1 (2022), p. 77.

[66] Christina Fuchs et al. “Determining the machining allowance for WAAM parts”. In: *Production Engineering* 14.5 (2020), pp. 629–637.

[67] Niechen Chen, Prashant Barnawal, and Matthew Charles Frank. “Automated post machining process planning for a new hybrid manufacturing method of additive manufacturing and rapid machining”. In: *Rapid Prototyping Journal* 24.7 (2018), pp. 1077–1090.

[68] Paolo C Priarone et al. “The role of re-design for additive manufacturing on the process environmental performance”. In: *Procedia Cirp* 69 (2018), pp. 124–129.

[69] Alessandro Salmi et al. “An integrated design methodology for components produced by laser powder bed fusion (L-PBF) process”. In: *Virtual and Physical Prototyping* 13.3 (2018), pp. 191–202.

[70] Jiho Jung et al. “Effect of line energy on microstructures and mechanical properties of Co-Cr-Mo alloy single-track fabricated by DED method”. In: *Journal of Alloys and Compounds* 946 (2023), p. 169381.

[71] Syamak Hossein Nedjad, Mehmet Yildiz, and Abdollah Saboori. “Solidification behaviour of austenitic stainless steels during welding and directed energy deposition”. In: *Science and Technology of Welding and Joining* 28.1 (2023), pp. 1–17.

[72] Abdollah Saboori et al. “An investigation on the effect of powder recycling on the microstructure and mechanical properties of AISI 316L produced by Directed Energy Deposition”. In: *Materials Science and Engineering: A* 766 (2019), p. 138360.

[73] Yuchao Bai, Akshay Chaudhari, and Hao Wang. “Investigation on the microstructure and machinability of ASTM A131 steel manufactured by directed energy deposition”. In: *Journal of Materials Processing Technology* 276 (2020), p. 116410.

[74] JG Lopes et al. “Effect of milling parameters on HSLA steel parts produced by Wire and Arc Additive Manufacturing (WAAM)”. In: *Journal of Manufacturing Processes* 59 (2020), pp. 739–749.

[75] Achref Kallel et al. “Analysis of the surface integrity induced by face milling of Laser Metal Deposited Ti-6Al-4V”. In: *Procedia CIRP* 87 (2020), pp. 345–350.

[76] Sebastian Greco et al. “Hybrid manufacturing: influence of material properties during micro milling of different additively manufactured AISI 316L”. In: *Production Engineering* 16.6 (2022), pp. 797–809.

[77] Panagiotis Stavropoulos, Thanassis Souflas, and Harry Bikas. “Hybrid manufacturing processes: an experimental machinability investigation of DED produced parts”. In: *Procedia CIRP* 101 (2021), pp. 218–221.

[78] Thanassis Souflas et al. “A comparative study of dry and cryogenic milling for Directed Energy Deposited IN718 components: effect on process and part quality”. In: *The International Journal of Advanced Manufacturing Technology* (2022), pp. 1–14.

[79] Anthony T Beaucamp et al. “Finishing of additively manufactured titanium alloy by shape adaptive grinding (SAG)”. In: *Surface Topography: Metrology and Properties* 3.2 (2015), p. 024001.

[80] Wu-Le Zhu et al. “Theoretical and experimental investigation of material removal mechanism in compliant shape adaptive grinding process”. In: *International Journal of Machine Tools and Manufacture* 142 (2019), pp. 76–97.

[81] Eleonora Atzeni et al. “Performance assessment of a vibro-finishing technology for additively manufactured components”. In: *Procedia CIRP* 88 (2020), pp. 427–432.

[82] Stephanie Prochaska and Owen Hildreth. “Effect of chemically accelerated vibratory finishing on the corrosion behavior of Laser Powder Bed Fusion 316L stainless steel”. In: *Journal of Materials Processing Technology* 305 (2022), p. 117596.

[83] Eleonora Atzeni et al. “The technology, economy, and environmental sustainability of isotropic superfinishing applied to electron-beam melted Ti-6Al-4V components”. In: *The International Journal of Advanced Manufacturing Technology* 117 (2021), pp. 437–453.

[84] Sangil Han et al. “Effect of abrasive flow machining (AFM) finish of selective laser melting (SLM) internal channels on fatigue performance”. In: *Journal of Manufacturing Processes* 59 (2020), pp. 248–257.

[85] Jiang Guo et al. “Internal surface quality enhancement of selective laser melted inconel 718 by abrasive flow machining”. In: *Journal of Manufacturing Science and Engineering* 142.10 (2020), p. 101003.

[86] Jingsi Wang, Jiaqi Zhu, and Pay Jun Liew. “Material removal in ultrasonic abrasive polishing of additive manufactured components”. In: *Applied Sciences* 9.24 (2019), p. 5359.

[87] Kai Liang Tan and Song Huat Yeo. “Surface modification of additive manufactured components by ultrasonic cavitation abrasive finishing”. In: *Wear* 378 (2017), pp. 90–95.

[88] Xiao Teng et al. “Study on magnetic abrasive finishing of AlSi10Mg alloy prepared by selective laser melting”. In: *The International Journal of Advanced Manufacturing Technology* 105 (2019), pp. 2513–2521.

[89] Neil Wilson et al. “Analysis of self-supporting conformal cooling channels additively manufactured by hybrid directed energy deposition for IM tooling”. In: *The International Journal of Advanced Manufacturing Technology* (2024), pp. 1–21.

[90] Paul Gradl, Angelo Cervone, and Piero Colonna. “Integral Channel Nozzles and Heat Exchangers using Additive Manufacturing Directed Energy Deposition NASA HR-1 Alloy”. In: *International Astronautical Congress (IAC)*. IAC-22, C4, 2, x73690. 2022.

[91] Jun Ge, Selvum Pillay, and Haibin Ning. “Post-process treatments for additive-manufactured metallic structures: a comprehensive review”. In: *Journal of Materials Engineering and Performance* 32.16 (2023), pp. 7073–7122.

[92] Haniyeh Fayazfar et al. “An overview of surface roughness enhancement of additively manufactured metal parts: a path towards removing the post-print bottleneck for complex geometries”. In: *The International Journal of Advanced Manufacturing Technology* 125.3 (2023), pp. 1061–1113.

[93] Jierui Mu et al. “Application of electrochemical polishing in surface treatment of additively manufactured structures: A review”. In: *Progress in Materials Science* (2023), p. 101109.

[94] Fabio Scherillo. “Chemical surface finishing of AlSi10Mg components made by additive manufacturing”. In: *Manufacturing letters* 19 (2019), pp. 5–9.

[95] Pawan Tyagi et al. “Reducing the roughness of internal surface of an additive manufacturing produced 316 steel component by chempolishing and electropolishing”. In: *Additive Manufacturing* 25 (2019), pp. 32–38.

[96] Zhang Baicheng et al. “Study of selective laser melting (SLM) Inconel 718 part surface improvement by electrochemical polishing”. In: *Materials & Design* 116 (2017), pp. 531–537.

[97] Chenhao Zhao, Ningsong Qu, and Xiaochuan Tang. “Removal of adhesive powders from additive-manufactured internal surface via electrochemical machining with flexible cathode”. In: *Precision Engineering* 67 (2021), pp. 438–452.

[98] Nikhil Nivrutti Kumbhar and AV Mulay. “Post processing methods used to improve surface finish of products which are manufactured by additive manufacturing technologies: a review”. In: *Journal of The Institution of Engineers (India): Series C* 99 (2018), pp. 481–487.

[99] Annamaria Gisario, Massimiliano Barletta, and Francesco Veniali. “Laser polishing: a review of a constantly growing technology in the surface finishing of components made by additive manufacturing”. In: *The International Journal of Advanced Manufacturing Technology* 120.3 (2022), pp. 1433–1472.

[100] A Temmler et al. “Influence of laser polishing on surface roughness and microstructural properties of the remelted surface boundary layer of tool steel H11”. In: *Materials & Design* 192 (2020), p. 108689.

[101] CP Ma, YC Guan, and Wei Zhou. “Laser polishing of additive manufactured Ti alloys”. In: *Optics and Lasers in Engineering* 93 (2017), pp. 171–177.

[102] Sundar Marimuthu et al. “Laser polishing of selective laser melted components”. In: *International Journal of Machine Tools and Manufacture* 95 (2015), pp. 97–104.

[103] B Richter et al. “Effect of initial surface features on laser polishing of Co-Cr-Mo alloy made by powder-bed fusion”. In: *Jom* 71 (2019), pp. 912–919.

[104] Muhannad A Obeidi et al. “Laser polishing of additive manufactured 316L stainless steel synthesized by selective laser melting”. In: *Materials* 12.6 (2019), p. 991.

[105] Lan Chen et al. “Effect of laser polishing on the microstructure and mechanical properties of stainless steel 316L fabricated by laser powder bed fusion”. In: *Materials Science and Engineering: A* 802 (2021), p. 140579.

[106] Benoit Rosa, Pascal Mognol, and Jean-Yves Hascoët. “Laser polishing of additive laser manufacturing surfaces”. In: *Journal of Laser Applications* 27.S2 (2015).

[107] Luiz Eduardo dos Santos Paes et al. “Understanding the behavior of laser surface remelting after directed energy deposition additive manufacturing through comparing the use of iron and Inconel powders”. In: *Journal of Manufacturing Processes* 70 (2021), pp. 494–507.

[108] Rajendra Hodgir, Ramesh K Singh, and Soham Mujumdar. “Experimental investigation of laser remelting in directed energy deposition (DED) of CPM-9V”. In: *Manufacturing Letters* 35 (2023), pp. 701–706.

[109] Seung Yeong Cho, Gwang Yong Shin, and Do Sik Shim. “Effect of laser remelting on the surface characteristics of 316L stainless steel fabricated via directed energy deposition”. In: *Journal of Materials Research and Technology* 15 (2021), pp. 5814–5832.

[110] Francesco Bruzzo et al. “Surface finishing by laser re-melting applied to robotized laser metal deposition”. In: *Optics and Lasers in Engineering* 137 (2021), p. 106391.

[111] Hong Shen et al. “Two-step laser based surface treatments of laser metal deposition manufactured Ti6Al4V components”. In: *Journal of Manufacturing Processes* 64 (2021), pp. 239–252.

[112] Yufan Liu et al. “Improving surface quality and superficial microstructure of LDED Inconel 718 superalloy processed by hybrid laser polishing”. In: *Journal of Materials Processing Technology* 300 (2022), p. 117428.

[113] Daniyar Syrlybayev et al. “The Post-Processing of Additive Manufactured Polymeric and Metallic Parts”. In: *Journal of Manufacturing and Materials Processing* 6.5 (2022), p. 116.

[114] Ambra Vandone, Stefano Baraldo, and Anna Valente. “Multisensor data fusion for additive manufacturing process control”. In: *IEEE Robotics and Automation Letters* 3.4 (2018), pp. 3279–3284.

[115] Gabriele Piscopo et al. “Analysis of single tracks of IN718 produced by laser powder directed energy deposition process”. In: *Procedia CIRP* 112 (2022), pp. 340–345.

[116] Mirna Poggi et al. “A Grey-Box Model of Laser Powder Directed Energy Deposition for Complex Scanning Strategy”. In: *Metals* 13.10 (2023), p. 1763.

[117] *Type 316L Austenitic Stainless Steel Powders for Additive Manufacturing*. DSM-0272.2. Oerlikon. 2022.

[118] Chunming Wang et al. “The influence of heat input on microstructure and mechanical properties for dissimilar welding of galvanized steel to 6061 aluminum alloy in a zero-gap lap joint configuration”. In: *Journal of Alloys and Compounds* 726 (2017), pp. 556–566.

[119] M Mahmoudi et al. “On the printability and transformation behavior of nickel-titanium shape memory alloys fabricated using laser powder-bed fusion additive manufacturing”. In: *Journal of Manufacturing Processes* 35 (2018), pp. 672–680.

[120] Wenjie Wang et al. “Surface morphology evolution mechanisms of laser polishing in ambient gas”. In: *International Journal of Mechanical Sciences* 250 (2023), p. 108302.

[121] Jilin Xu et al. “Investigation into the laser polishing of an austenitic stainless steel”. In: *Optics & Laser Technology* 163 (2023), p. 109378.

[122] Veronica Czitrom. “One-factor-at-a-time versus designed experiments”. In: *The American Statistician* 53.2 (1999), pp. 126–131.

[123] Douglas C Montgomery. *Design and analysis of experiments*. John wiley & sons, 2017.

[124] Jacqueline K Telford. “A brief introduction to design of experiments”. In: *Johns Hopkins apl technical digest* 27.3 (2007), pp. 224–232.

[125] Joan Fisher Box. “RA Fisher and the design of experiments, 1922–1926”. In: *The American Statistician* 34.1 (1980), pp. 1–7.

[126] Charles Sanders Peirce. *Illustrations of the Logic of Science*. Open Court, 2014.

[127] Jay T Lennon. “Replication, lies and lesser-known truths regarding experimental design in environmental microbiology”. In: *Environmental Microbiology* 13.6 (2011), pp. 1383–1386.

[128] Zoé Jardon et al. “Directed Energy Deposition roughness mitigation through laser remelting”. In: *Procedia CIRP* 111 (2022), pp. 180–184.

[129] ISO. *Geometric Product Specification (GPS) — Surface texture: Profile - Part3: Specification operators*. en. Standard ISO 21920-3:2021. Geneva, Switzerland, 2021.

[130] Luiz Eduardo dos Santos Paes et al. “Lack of fusion mitigation in directed energy deposition with laser (DED-L) additive manufacturing through laser remelting”. In: *Journal of Manufacturing Processes* 73 (2022), pp. 67–77.

[131] Jerrold H Zar. “Spearman rank correlation”. In: *Encyclopedia of biostatistics* 7 (2005).

[132] Laura Kreinest et al. “Structuring by laser remelting as a method for waviness reduction on additive manufactured parts”. In: *Procedia CIRP* 111 (2022), pp. 689–692.

[133] Vigdis By Kampenes et al. “A systematic review of effect size in software engineering experiments”. In: *Information and Software Technology* 49.11-12 (2007), pp. 1073–1086.

[134] Roger Bakeman. “Recommended effect size statistics for repeated measures designs”. In: *Behavior research methods* 37 (2005), pp. 379–384.

[135] John TE Richardson. “Eta squared and partial eta squared as measures of effect size in educational research”. In: *Educational research review* 6.2 (2011), pp. 135–147.

[136] Bastian Meylan, Ivan Calderon, and Kilian Wasmer. “Optimization of Process Parameters for the Laser Polishing of Hardened Tool Steel”. In: *Materials* 15.21 (2022), p. 7746.

[137] A Temmler et al. “Experimental investigation on surface structuring by laser remelting (WaveShape) on Inconel 718 using varying laser beam diameters and scan speeds”. In: *Applied Surface Science* 541 (2021), p. 147814.

[138] Raymond H Myers, Douglas C Montgomery, and Christine M Anderson-Cook. *Response surface methodology: process and product optimization using designed experiments*. John Wiley & Sons, 2016.

[139] George EP Box and Donald W Behnken. “Some new three level designs for the study of quantitative variables”. In: *Technometrics* 2.4 (1960), pp. 455–475.

[140] Paul G Mathews. *Design of Experiments with MINITAB*. Quality press, 2004.

[141] Chang Ye et al. “Effects of post-processing on the surface finish, porosity, residual stresses, and fatigue performance of additive manufactured metals: a review”. In: *Journal of Materials Engineering and Performance* 30 (2021), pp. 6407–6425.

[142] Gary S Schajer. *Practical residual stress measurement methods*. John Wiley & Sons, 2013.

[143] MN James et al. “Residual stresses and fatigue performance”. In: *Engineering Failure Analysis* 14.2 (2007), pp. 384–395.

[144] NS Rossini et al. “Methods of measuring residual stresses in components”. In: *Materials & Design* 35 (2012), pp. 572–588.

[145] Johannes Preußner et al. “Microstructure and residual stresses of laser remelted surfaces of a hot work tool steel”. In: *International journal of materials research* 105.4 (2014), pp. 328–336.

[146] Thomas Simson et al. “Residual stress measurements on AISI 316L samples manufactured by selective laser melting”. In: *Additive Manufacturing* 17 (2017), pp. 183–189. ISSN: 2214-8604. DOI: https://doi.org/10.1016/j.addma.2017.07.007. URL: https://www.sciencedirect.com/science/article/pii/S2214860417301604.

[147] Daisuke Fukui, Nobuo Nakada, and Susumu Onaka. "Internal residual stress originated from Bain strain and its effect on hardness in Fe–Ni martensite". In: *Acta Materialia* 196 (2020), pp. 660–668. ISSN: 1359-6454. DOI: https://doi.org/10.1016/j.actamat.2020.07.013. URL: https://www.sciencedirect.com/science/article/pii/S1359645420305115.

[148] Xiaomei Xu et al. "Laser Polishing and Annealing Injection Mold Using Dual-Beam Laser System". In: *Coatings* 12.12 (2022), p. 1822.

[149] AV Gusarov, M Pavlov, and I Smurov. "Residual stresses at laser surface remelting and additive manufacturing". In: *Physics Procedia* 12 (2011), pp. 248–254.

[150] Yingtao Tian et al. "Material interactions in laser polishing powder bed additive manufactured Ti6Al4V components". In: *Additive Manufacturing* 20 (2018), pp. 11–22.

[151] Seungjong Lee et al. "Laser polishing for improving fatigue performance of additive manufactured Ti-6Al-4V parts". In: *Optics & Laser Technology* 134 (2021), p. 106639.

[152] ASTM International. *Standard test Method for Determining Residual Stresses by the Hole-Drilling Strain-Gage Method*. en. Standard ASTM E837-20. West Conshohocken, USA, 2020.

[153] ASTM International. *Standard test Method for Microindentation Hardness of Materials*. en. Standard ASTM E384-17. West Conshohocken, USA, 2017.

[154] P. Zhang, S.X. Li, and Z.F. Zhang. "General relationship between strength and hardness". In: *Materials Science and Engineering: A* 529 (2011), pp. 62–73. ISSN: 0921-5093. DOI: https://doi.org/10.1016/j.msea.2011.08.061. URL: https://www.sciencedirect.com/science/article/pii/S0921509311009555.

[155] William D Callister Jr and David G Rethwisch. *Fundamentals of materials science and engineering: an integrated approach*. John Wiley & Sons, 2020.

[156] Sneha N. Naik and Stephen M. Walley. "The Hall–Petch and inverse Hall–Petch relations and the hardness of nanocrystalline metals". In: *Journal of Materials Science* 55.7 (2020), pp. 2661–2681. ISSN: 1573-4803. DOI: 10.1007/s10853-019-04160-w. URL: https://doi.org/10.1007/s10853-019-04160-w.

[157] Fang Zhihao et al. "Laser Polishing of Additive Manufactured Superalloy". In: *Procedia CIRP* 71 (2018). 4th CIRP Conference on Surface Integrity (CSI 2018), pp. 150–154. ISSN: 2212-8271. DOI: https://doi.org/10.1016/j.procir.2018.05.088. URL: https://www.sciencedirect.com/science/article/pii/S2212827118307169.

[158] Prakash Kattire et al. "Experimental characterization of laser cladding of CPM 9V on H13 tool steel for die repair applications". In: *Journal of Manufacturing Processes* 20 (2015). Additive Manufacturing, pp. 492–499. ISSN: 1526-6125. DOI: https://doi.org/10.1016/j.jmapro.2015.06.018. URL: https://www.sciencedirect.com/science/article/pii/S1526612515000638.

[159] Linmao Qian et al. “Comparison of nano-indentation hardness to microhardness”. In: *Surface and Coatings Technology* 195.2 (2005), pp. 264–271. ISSN: 0257-8972. DOI: https://doi.org/10.1016/j.surfcoat.2004.07.108. URL: https://www.sciencedirect.com/science/article/pii/S0257897204006802.

[160] ASTM International. *Standard Test Method for Vicker Hardness and Knoop Hardness of Metallic Materials*. en. Standard ASTM E92-23. West Conshohocken, USA, 2023.

[161] Christian Nüsser et al. “Process-and material-induced surface structures during laser polishing”. In: *Advanced Engineering Materials* 17.3 (2015), pp. 268–277.

[162] Shirzad Mohajerani et al. “Thermo-physical modelling of track width during laser polishing of H13 tool steel”. In: *Procedia Manufacturing* 10 (2017), pp. 708–719.

[163] Shirzad Mohajerani et al. “Thermophysical simulation and experimental verification of remelting lines during laser polishing of H13 tool steel”. In: *Lasers in Manufacturing and Materials Processing* 7 (2020), pp. 317–337.

[164] Chi Zhang, Jing Zhou, and Hong Shen. “Role of capillary and thermocapillary forces in laser polishing of metals”. In: *Journal of Manufacturing Science and Engineering* 139.4 (2017), p. 041019.

[165] Jilin Xu et al. “Study on the mechanism of surface topography evolution in melting and transition regimes of laser polishing”. In: *Optics & Laser Technology* 139 (2021), p. 106947.

[166] Fabian Soffel et al. “Laser remelting process simulation and optimization for additive manufacturing of Nickel-based super alloys”. In: *Materials* 15.1 (2021), p. 177.

[167] Bastian Meylan et al. “Thermal modelling and experimental validation in the perspective of tool steel laser polishing”. In: *Applied Sciences* 12.17 (2022), p. 8409.

[168] Liang Yan et al. “Application and Prospect of Wear Simulation Based on ABAQUS: A Review”. In: *Lubricants* 12.2 (2024). ISSN: 2075-4442. DOI: 10.3390/lubricants12020057. URL: https://www.mdpi.com/2075-4442/12/2/57.

[169] Balaji Soundararajan et al. “Review on modeling techniques for powder bed fusion processes based on physical principles”. In: *Additive Manufacturing* 47 (2021), p. 102336. ISSN: 2214-8604. DOI: https://doi.org/10.1016/j.addma.2021.102336. URL: https://www.sciencedirect.com/science/article/pii/S2214860421004942.

[170] Muhammad Qasim Zafar et al. “Finite element framework for electron beam melting process simulation”. In: *The International Journal of Advanced Manufacturing Technology* 109.7 (2020), pp. 2095–2112. ISSN: 1433-3015. DOI: 10.1007/s00170-020-05707-x. URL: https://doi.org/10.1007/s00170-020-05707-x.

[171] Y Jia et al. “A comprehensive comparison of modeling strategies and simulation techniques applied in powder-based metallic additive manufacturing processes”. In: *Journal of Manufacturing Processes* 110 (2024), pp. 1–29.

[172] Gabriele Piscopo, Eleonora Atzeni, and Alessandro Salmi. “A hybrid modeling of the physics-driven evolution of material addition and track generation in laser powder directed energy deposition”. In: *Materials* 12.17 (2019), p. 2819.

[173] Abaqus Verification Manual. https://https://classes.engineering.wustl.edu/2009/spring/mase5513/abaqus/docs/v6.6/books/ver/default.htm?startat=ch04s01abv246.html. Accessed: 12th of December 2024.

[174] ASTM International. *Standard Specification for Standard Nominal Diameters and Cross-Sectional Areas of AWG Sizes of Solid Round Wires Used as Electrical Conductors*. en. Standard ASTM B258-18. West Conshohocken, USA, 2018.

Appendix A

Bases of Inferential Statistics

The present Appendix collects some basic concepts of inferential statistics, necessary for understanding the choices made through the work. The textbooks *Design and Analysis of Experiments* [123], already cited in the work, and *Response Surface Methodology* [138] surely had a central role in the composition of this Appendix, proving a clear guide in the context of inferential statistics, from simple concepts to more sophisticated ones. The Appendix is further divided in three sections for an easier fruition. Section A.1 describes the basic preliminary concepts, such as mean, variance sampling distributions and simple comparative experiments. Section A.2 explains the analysis of variance, core element of every experimental activity, with in-depth description of every parameter. Finally Section A.3 provides the statistical instruments to evaluate the quality of the predictions provided by different experimental designs.

A.1 Basic Concepts

A.1.1 Preliminary Definitions

Experimental activities must always provide a quantitatively measurable response. In fact, the absence of a measurable feedback from the system under investigation would preclude any potential description of the same system. When the response of the system can be quantified, it can be considered a variable. The introduction

of uncontrollable measurement fluctuations results in an error in the measured variable, which consequently becomes a random variable. The most effective method to describe the behaviour of a random variable is through the use of probability distributions. Each probability distribution is described by a mean value and variance. The mean of a probability function, represented here as μ, is an indicator of the centre of the distribution. The mathematical formulation of the mean is presented for both a continuous variable, Equation A.1, and a discrete variable, Equation A.2.

$$\mu_{continuous} = \int_{-\infty}^{\infty} yf(y)dy \tag{A.1}$$

$$\mu_{discrete} = \sum_{all\ y} yp(y_i) \tag{A.2}$$

where $f(y)$ and $p(y)$ are the probability of the continuous y variable and of the discrete y variable respectively. The variance, σ^2, is an index of the dispersion of the probability function. A large variance indicates a considerable dispersion of the variable under investigation, covering a wider range of existence. Conversely, a low variance indicates the opposite, namely a narrow distribution with limited dispersion of data. Equation A.3 and Equation A.4 present the mathematical formulations of the variance for continuous and discrete variables respectively. The standard deviation, denoted by the symbol σ is another widely used indicator of the dispersion of the probability function, and it is computed as the square root of the variance. In practical applications, the standard deviation is often the preferred measure of dispersion, as it shares the same units of the response variable.

$$\sigma^2_{continuous} = \int_{-\infty}^{\infty} (y-\mu)^2 f(y)dy \tag{A.3}$$

$$\sigma^2_{discrete} = \sum_{all\ y} (y-\mu)^2 p(y_i) \tag{A.4}$$

A.1.2 Sampling Distributions

In statistics, a population represents the generalisation of a real group, it is the conceptual framework underlying the real observation under consideration. Inferential

statistics aims at understanding the characteristics of a population from a sample, which is typically a random sample drawn from the same population. A random sample is drawn from a population with the same probability of every other sample of the same population. A sample can be characterised by its mean and variance, similarly to what was outlined for probability distributions. The mean of a sample is given by Equation A.5:

$$\bar{y} = \frac{\sum_{i=1}^{n} y_i}{n} \tag{A.5}$$

and the sample variance by Equation A.6:

$$S^2 = \frac{\sum_{i=1}^{n} (y_i - \bar{y})^2}{n-1} \tag{A.6}$$

the numerator represents the sum of squares of the errors, namely the difference between single observations and mean value, and $n-1$ is the number of degree of freedom of the sample. The sample standard deviation is defined as squared root of the variance just outlined.

Normal Distribution

The study of sample distributions is of uttermost importance in the field of inferential statistics. The initial and most important sampling distribution here described is the normal distribution, mathematically defined according to Equation A.7, where y is the random variable under study, μ is the mean and σ^2 the variance. Several phenomena can be represented by normal distributions, particularly those that are governed by stochastic phenomena. A particular case of the normal distribution is the standard normal distribution, which is derived by setting $\mu = 0$ and $\sigma^2 = 1$.

$$f(y) = \frac{1}{\sigma\sqrt{2\pi}} e^{-\frac{1}{2}(\frac{y-\mu}{\sigma})^2} \tag{A.7}$$

χ^2 Distribution

A second distribution worth citing is the χ^2 distribution. Having n independent variables, all distributed according to standard normal distributions, the sum of their squares, x, will follow a χ^2 distribution, as per Equation A.8. Since x is defined as a sum of squares, it follows that its value is strictly positive. The significance of the χ^2 distribution lies in the fact that the sample variance follows a χ^2 distribution multiplied by a constant of proportionality, as highlighted by Equation A.9.

$$f(x) = \frac{1}{2^{k/2}\Gamma(\frac{k}{2})} x^{\frac{k}{2}-1} e^{-\frac{x}{2}} \tag{A.8}$$

$$S^2 = \frac{\sigma^2}{n-1}\chi^2_{n-1} \tag{A.9}$$

Fisher-Snedecor Distribution

Finally, the last sampling distribution presented is the Fisher distribution, or F-distribution, followed by the ratio in the right term of Equation A.10. Where χ^2_i and χ^2_j are two independent variables that follow the χ^2-distribution with i and j degrees of freedom.

$$F(i,j) = \frac{\chi^2_i / i}{\chi^2_j / j} \tag{A.10}$$

The probability distribution of an F-variable is described by Equation A.11. For instance, the F-distribution describes the distribution of the ratio between the variances of two samples drawn from the same population, with common variance σ^2.

$$f(F(i,j)) = \frac{\Gamma(\frac{u+v}{2})((\frac{u}{v})^{u/2} x^{u/2-1})}{\Gamma(\frac{u}{x})\Gamma(\frac{v}{2})((\frac{u}{v})x+1)^{(u+v)/2}} \tag{A.11}$$

A.2 Comparative Tests

A.2.1 Hypothesis Testing

A statistical hypothesis is the formalisation of a conjecture pertaining to the parameters of a probability distribution. When dealing with two or more distributions, the necessity of comparing them may arise, particularly in terms of their mean values. In this scenario, two main hypotheses can be formalised as in Equation A.12. The null hypothesis, represented by H_0, implies the equality of the two means, whereas the alternative hypothesis, represented by H_1, implies the difference of the same means. In general, hypothesis testing provides a procedure for determining whether to reject, or fail to reject, the null hypothesis.

$$\begin{aligned} H_0 &: \mu_1 = \mu_2 \\ H_1 &: \mu_1 \neq \mu_2 \end{aligned} \tag{A.12}$$

The procedure carried out to test the null hypothesis may also yield erroneous outcomes. For instance, a test may conclude that the means of the sample distribution are different, when in fact they are equal. This leads to the rejection of the null hypothesis even if the null hypothesis is true. This situation is referred to as type I error. Conversely, if the test fails to distinguish two means, thereby stating their equivalence when they stand different one from another, a type II error occurs. The probabilities of the occurrence of these two errors are designated as α and β respectively. Instead of referring to β, it is common to use its one's complement, called *Power* of the test. The power of a test is the probability of rejecting H_0 when H_0 is actually false.

A.2.2 Two-sample T-Test

The two-sample t-Test is an invaluable tool for pairwise comparisons of sample distributions, under the assumption of common variance. The test is performed according to Equation A.13, and the results are compared with the values assumed by the t-distribution for $\alpha/2$ and n_1+n_2-2 degrees of freedom. If $t_0 > t_{\alpha/2,n_1+n_2-2}$ then the null hypothesis must be rejected, concluding that the two samples have

different mean values. Conversely, if $t_0 < t_{\alpha/2,n_1+n_2-2}$ the test fails in rejecting the null hypothesis. Thus, for a given level of significance, the t-Test provides only a punctual information about the rejection, or not, of the null hypothesis, with no further statement on the degree of divergence the two samples are.

$$t_0 = \frac{\bar{y}_1 - \bar{y}_2}{S_p \sqrt{\frac{1}{n_1} + \frac{1}{n_2}}} \tag{A.13}$$

Where:

- $\bar{y}_1$ and $\bar{y}_2$ are the means of the two samples;
- n_1 and n_2 are the sizes of the two samples;
- S_p is an estimate of the common variances of the two samples, as per Equation A.14;
- α is the significance level assumed for the test.

$$S_p^2 = \frac{(n_1 - 1)S_1^2 + (n_2 - 1)S_2^2}{n_1 + n_2 - 2} \tag{A.14}$$

A.2.3 P-value Approach

The t-Test always results in the rejection, or non rejection, of the null hypothesis for a fixed level of significance. Sometimes this approach might be poorly descriptive of the scenario in place, since no additional information is provided about the amount of dissimilarities that led to the rejection of the null hypothesis (or to the closeness that led to the impossibility of rejecting the null hypothesis). Therefore, the p-value approach has been widely adopted to overcome this limitations. The p-value test provides the smallest level of significance that would result in rejecting the null hypothesis. For instance, a p-value equal to 0.05 implies that the null hypothesis can be rejected at a significance level of 0.05. It comes naturally to understand the higher flexibility of the p-value test, allowing the experimenter to be in closer contact with what is happening in the test.

A.2.4 Analysis of Variance - ANOVA

The t-test and the p-value approach have been presented for introducing the comparisons between two means. In most cases, industrial experiments are not limited to simple pairwise comparisons, but may involve several comparisons at the same time. These comparisons may result from either different processes, or from different levels of a single process parameter, here generically recalled as different treatments. The outcomes of an experiment may be organised as described in Equation A.15. In an experiment with a treatments and n observations per treatment, the term $y_{i,j}$ represents the generic experimental observation, μ is the overall mean of the observations, τ_i is the effect induced by the i-th treatment, and $\varepsilon_{i,j}$ is the random component associated with the generic observation.

$$\begin{aligned} y_{i,j} &= \mu + \tau_i + \varepsilon_{i,j} \\ i &= 1,2,\ldots,a \\ j &= 1,2,\ldots,n \end{aligned} \tag{A.15}$$

The test hypothesis for the considered scenario may be summarised as H_0 : $\mu_1 = \mu_2 = \cdots = \mu_a$ and $H_1 : \mu_i \neq \mu_j$ for at least one combination of i and j. The same hypothesis can be also written as $H_0 : \tau_1 = \tau_2 = \cdots = \tau_a = 0$ and $H_1 : \tau_i \neq 0$ for at least one i. Therefore, if a single effect is found to be significant, the null hypothesis must be rejected and the alternative hypothesis embraced. The name ANOVA, analysis of variance, derives from the decomposition of the total system variability in its subcomponents. The total variability of the system can be expressed as the sum of squares, SS_T, as reported in Equation A.16.

$$SS_T = \sum_{i=1}^{a} \sum_{j=1}^{n} (y_{i,j} - \bar{y}_{..})^2 \tag{A.16}$$

Therefore, the total sum of squares can be decomposed in two subcomponents, the sum of squares between treatments, and the sum of squares within the treatment, as per Equation A.17. The sum of squares between different treatment is a measure of the effects of the treatments. Conversely, the sum of squares within the single treatment is solely related to the contribution of random effects, and can be therefore

associated with the pure error component. Equation A.18 summarise the terms expressed by Equation A.17.

$$\sum_{i=1}^{a}\sum_{j=1}^{n}(y_{i,j}-\overline{y}_{..})^2 = n\sum_{i=1}^{a}(\overline{y}_{i.}-\overline{y}_{..}^2)+\sum_{i=1}^{a}\sum_{j=1}^{n}(y_{i,j}-\overline{y}_{i.})^2 \tag{A.17}$$

$$SS_T = SS_{Treatments} + SS_E \tag{A.18}$$

The Mean Squares, MS, are computed dividing the $SS_{Treatmens}$ and the SS_E by the correspondent degrees of freedom. Comparing the $MS_{Treatments}$ with the MS_E, the actual significance of the a-th treatment can be assessed. It is wort noticing that the ratio between $MS_{Treatments}$ and MS_E follows an F-distribution with $a-1$ and $n-a$ degree of freedoms, as per Equation A.19.

$$F_0 = \frac{MS_{Treatments}}{MS_E} \tag{A.19}$$

If $F_0 > F_{\alpha,a-1,N-a}$, then the a-th treatment can be considered significant at an α significance level, and the null hypothesis H_0 can be rejected. Moreover, there are other parameters used to describe the efficacy of the ANOVA model. The first one is the R^2 coefficient, computed as reported in Equation A.20. The R^2 coefficient expresses the percentage of the total system variability accounted by the model. Therefore, R^2 is always contained between 0 and 1, with values closer to one being preferred, as they indicate a better fit of the model to the actual system.

$$R^2 = \frac{SS_{Treatments}}{SS_T} = 1 - \frac{SS_E}{SS_T} \tag{A.20}$$

One intrinsic issue with the definition of the R^2 coefficient is that it always increases when new terms are introduced into the model. This behaviour can result in misleading outcomes if the terms introduced into the model are not actually statistically meaningful, as they artificially increase the R^2 coefficient without providing a better description of the system. Therefore, the R^2_{adj} was designed to also consider the presence of inactive terms in the ANOVA model. Equation A.21 highlights the difference between the two coefficients. In the R^2_{adj} definition, the term $(k+1)$ accounts for the number of terms considered in the model. Higher values of $(k+1)$ result in a lower R^2_{adj}, therefore considering the presence of non-significant terms.

$$R^2_{adj} = 1 - \frac{n-1}{n-(k+1)} \frac{SS_E}{SS_T} \tag{A.21}$$

Finally, it is possible to ascertain the extent to which the current model is capable of predicting new data. The coefficient R^2_{pred}, as defined in Equation A.22, fulfils this role. The term PRESS is the acronym for *Prediction error sum of squares* and it is computed as the sum of the squared prediction errors derived by predicting the n-th data with a model that includes all the other observations except the n-th one. A low PRESS value results in a high R^2_{pred} and in a good prediction ability of the model.

$$R^2_{pred} = 1 - \frac{PRESS}{SS_T} \tag{A.22}$$

A.3 Quality Assessment of Experimental Designs

The choice of the most suitable experimental design is a fundamental moment of any experimental campaign, having the potential to deeply affect the results obtained.

A.3.1 Orthogonality

Several criteria are available for the assessment of the efficacy of the selected design. The first criterion, knows as *D-optimality*, refers to designs exhibiting minimal variance in model parameters, being strictly related to the concept of orthogonality. A design is considered orthogonal if, and only if, the matrix **X'X** is a diagonal matrix; with **X** being the model matrix of the investigated design. If the matrix **X'X** is diagonal, then the columns of the **X** matrix are mutually orthogonal. This geometric conclusion ensures that the columns of the **X** matrix are linearly independent of one another. This further implies that the terms of the model resulting from the model matrix **X** are all linearly independent, and that can be independently computed. The orthogonality is particularly significant if the design is meant to fit a first-order model, as in the case of exploratory analyses. It ensures that the conclusion about the significance of one factor is completely independent of the influence of other factors considered.

Two-level factorial designs, with and without central points, are *D-optimal* designs, meaning they have linearly independent effects and allow minimal variance of the model parameters. For instance, Matrix A.23 is the model matrix of a generic 2^2 factorial designs, able to estimate both linear and interaction terms. It is straightforward to notice that the matrix columns are orthogonal, as also shown by Matrix A.24 being diagonal.

$$\mathbf{X} = \begin{bmatrix} 1 & -1 & -1 & 1 \\ 1 & -1 & 1 & -1 \\ 1 & 1 & -1 & -1 \\ 1 & 1 & 1 & 1 \end{bmatrix} \tag{A.23}$$

$$\mathbf{X'X} = \begin{bmatrix} 4 & 0 & 0 & 0 \\ 0 & 4 & 0 & 0 \\ 0 & 0 & 4 & 0 \\ 0 & 0 & 0 & 4 \end{bmatrix} \tag{A.24}$$

A.3.2 Rotatability

Another crucial aspect of experiment designs is the ability to finely predicting the variance of the response variable across the specified region of interest. Designs that fit first-order models are typically not focused on achieving a fine prediction of the response variable, being constructed to screen active factors from inactive ones. Conversely, this aspect acquire a major importance for designs that fir second-order models, whose main objective is the definition of an accurate model of the response variable.

Two main parameters can be computed for assessing the performance of the considered design in terms of predicted variance: the unscaled prediction variance, defined by Equation A.25, and the scaled prediction variance (SPV), as in Equation A.26. The scaled prediction variance also considers the number of experimental runs belonging to the design. This difference allows the use of SPV to compare the resource efficiencies of different design, despite their comparable predicted variance of the response variable.

$$UPV = Var[y(x)]/\sigma^2 \tag{A.25}$$

$$SPV = N \cdot Var[y(x)]/\sigma^2 \tag{A.26}$$

Both parameters may be used to evaluate the rotatability properties of the design. A design is defined as rotatable if the predicted variance of the response variable, at a specific location within the design space, is solely dependent on the distance between the centre of the design space and the considered point. Consequently, rotatable designs do not have preferential directions along which the predicted variance is minimal, ensuring that the response of the system is acquired with equal accuracy across the entire region of interest. The rotatability of a design can be easily assessed using the same definitions of UPV and SPV. The variance of the predicted response variable is defined by Equation A.27. Therefore, the SPV can be computed as $SPV(x) = Nx'_m(X'X)^{-1}x'_m$. If the SPV is solely a function of the polar distance from the centre of the region of interest, then the design can be considered rotatable.

$$Var[y(x)] = \sigma^2 x'_m(X'X)^{-1}x'_m \tag{A.27}$$

In the remaining part of the section a practical example of rotatability assessment has been reported to provide the reader with a practical guide on how to perform the assessment. A 3^2 design was selected as it was the chosen design during the optimisation campaign reported in Chapter 4. Therefore, given a 3^2 factorial design, the fitted model always has the form of $y = \beta_0 + \beta_1\, x_1 + \beta_2 x_2 + \beta_3 x_1^2 + \beta_4 x_2^2 + \beta_5 x_1 x_2$. The same can be deduced by the vector reported in Equation A.28. The model matrix **X** is shown in Equation A.29, and the product **X'X** in Equation A.30.

$$\mathbf{x_m} = \begin{bmatrix} 1 & x_1 & x_2 & x_1^2 & x_2^2 & x_1 x_2 \end{bmatrix} \tag{A.28}$$

$$\mathbf{X} = \begin{bmatrix} 1 & -1 & -1 & 1 & 1 & 1 \\ 1 & -1 & 0 & 1 & 0 & 0 \\ 1 & -1 & 1 & 1 & 1 & -1 \\ 1 & 0 & -1 & 0 & 1 & 0 \\ 1 & 0 & 0 & 0 & 0 & 0 \\ 1 & 0 & 1 & 0 & 1 & 0 \\ 1 & 1 & -1 & 1 & 1 & -1 \\ 1 & 1 & 0 & 1 & 0 & 0 \\ 1 & 1 & 1 & 1 & 1 & 1 \end{bmatrix} \tag{A.29}$$

$$\mathbf{X'X} = \begin{bmatrix} 9 & 0 & 0 & 6 & 6 & 0 \\ 0 & 6 & 0 & 0 & 0 & 0 \\ 0 & 0 & 6 & 0 & 0 & 0 \\ 6 & 0 & 0 & 6 & 4 & 0 \\ 6 & 0 & 0 & 4 & 6 & 0 \\ 0 & 0 & 0 & 0 & 0 & 4 \end{bmatrix} \tag{A.30}$$

Matrix **X'X** is symmetric but not diagonal, confirming the non orthogonality of the design. This aspect is often overlooked for designs fitting second order models, as higher importance is given to their rotatability. After additional computations, the SPV for the 3^2 design is reported in Equation A.31. Although the design is clearly non-rotatable, the most critical parts of the region of interests are the corners, where both x_1 and x_2 have high absolute values at the same time. In most of the central part of the region of interest the SPV remains in an acceptable range, being non-critical for most applications.

$$SPV = N \cdot \mathbf{x_m}'(\mathbf{X}'\mathbf{X})^{-1}\mathbf{x_m} = 5 + 2.25x_1^2x_2^2 \tag{A.31}$$

Appendix B

Abaqus Subroutines

B.1 FILM User-Defined Subroutine

```
      SUBROUTINE FILM(H,SINK,TEMP,KSTEP,KINC,TIME,NOEL,NPT,
     1 COORDS,JLTYP,FIELD,NFIELD,SNAME,NODE,AREA)
C
      INCLUDE 'ABA_PARAM.INC'
C
      DIMENSION H(2),TIME(2),COORDS(3), FIELD(NFIELD)
      CHARACTER*80 SNAME

        real r,v,pi
        real X0,Y0,Z0,T
        real Dist, X_center, Y_center

        !Position of the current node
        X = COORDS(1)
        Y = COORDS(2)
        Z = COORDS(3)
        T = TIME(2)

        X0   = -10
        Y0   = 25
        Z0   = 0
```

```
    Dist = 0.0

    pi   = 3.1415927
    r    = 4
    !Travelling speed of the deposition head
    v    = 8.133
    !Convective heat transfer coefficient
    h(1) = 0
    !Rate of change of the coefficient
    h(2) = 0
    !Temperature of the surrounding environment
    sink = 25

    ![...]

    YT = Y_center - Y
    XT = X_center - X

    Dist = SQRT((YT*YT)+(XT*XT))

    if (Dist < r) then
        !Forced convection
        h(1) = 1/(4*SQRT(2*pi))*EXP(-Dist*Dist/10)
    else if (Dist > r) then
        !Natural convection
        h(1) = 0.020
    end if

RETURN
END
```

B.2 DFLUX User-Defined Subroutine

```
      SUBROUTINE DFLUX(FLUX,SOL,KSTEP,KINC,TIME,NOEL,NPT,COORDS,
     1 JLTYP,TEMP,PRESS,SNAME)
C
      INCLUDE 'ABA_PARAM.INC'
C
      DIMENSION FLUX(2), TIME(2), COORDS(3)

      CHARACTER*80 SNAME

        real p,eta,pi,q,r,v
        real X0,Y0,Z0,T
        real Dist, X_center, Y_center

        X = COORDS(1)
        Y = COORDS(2)
        Z = COORDS(3)
        T = TIME(2)

        X0   = -10
        Y0   =  25
        Z0   =  0
        Dist = 0.0

        pi   =  3.1415927
        !Laser Beam Ray
        r    =  1.
        !Travelling speed of the deposition head
        v    =   8.133
        !Laser Power
        p    =  700000
        !Absorbivity
        eta =   0.32
        !Heat flux
        q    =   eta*p/(pi*r*r)
```

```
      ![...]

      YT = Y_center - Y
      XT = X_center - X

      FLUX(1) = 0
      Dist    = YT*YT + XT*XT

      if (Dist < r) then
         !Heat Flux Inside the Laser Beam
         FLUX(1) = q
      elde if

      FLUX(2) = 0.0

    RETURN
    END
```

Appendix C

Experimental campaign complete dataset

This Appendix collects all the datasets related to the experimental campaign. Section C.1 covers the exploratory campaign, Section C.2 presents the data referred to the steepest descend method, and Section C.3 collects the dataset from the optimization campaign. Through all the phases of the campaigns, 3 replicates were performed of every factorial point. The value of each replica is obtained in turn as the average of the five replicated measurements performed on each surface.

C.1 Exploratory campaign dataset

Table C.1 Exploratory campaign results for $Ra_{\perp}$ and $Ra_{\parallel}$.

Treat. N.	LED ($\mathrm{J\,mm^{-1}}$)	h_d (mm)	S_d (mm)	V_{Ar} ($\mathrm{L\,min^{-1}}$)	$Ra_{\perp}$ (µm)	$Ra_{\parallel}$ (µm)
					3.4	2.9
1	21	1	8	2	3.9	2.9
					3.4	3.2
					3.8	2.5
2	21	1	8	10	4.2	2.1
					3.8	2.0

Table C.1 – Continued from previous page.

Treat. N.	LED ($J\,mm^{-1}$)	h_d (mm)	S_d (mm)	V_{Ar} ($L\,min^{-1}$)	$Ra_{\perp}$ (µm)	$Ra_{\parallel}$ (µm)
					3.4	3.3
3	21	1	28	2	3.3	4.1
					3.1	2.8
					3.5	2.6
4	21	1	28	10	3.5	3.3
					3.3	2.9
					8.5	2.4
5	21	2	8	2	9.2	2.5
					8.4	2.5
					7.7	2.9
6	21	2	8	10	7.5	2.6
					7.8	2.2
					9.7	5.0
7	21	2	28	2	9.8	4.3
					8.9	4.5
					11.1	3.1
8	21	2	28	10	11.7	3.4
					10.9	2.6
					2.9	3.6
9	70	1	8	2	2.8	3.8
					2.4	3.1
					2.9	1.8
10	70	1	8	10	2.7	2.0
					2.8	2.6
					5.0	4.0
11	70	1	28	2	4.8	3.6
					4.5	3.7
					4.9	2.6
12	70	1	28	10	4.8	2.6

Table C.1 – Continued from previous page.

Treat. N.	LED ($J\,mm^{-1}$)	h_d (mm)	S_d (mm)	V_{Ar} ($L\,min^{-1}$)	$Ra_\perp$ (µm)	$Ra_\parallel$ (µm)
					4.5	2.3
					4.5	2.5
13	70	2	8	2	5.8	2.5
					5.9	2.6
					6.1	2.9
14	70	2	8	10	5.1	2.7
					5.4	2.8
					5.9	3.9
15	70	2	28	2	4.5	4.0
					4.3	3.8
					4.1	2.8
16	70	2	28	10	4.9	2.7
					4.7	2.2
					4.0	2.7
					4.5	3.3
17	45.5	1.5	18	6	3.0	3.1
					3.1	2.4
					2.4	2.2

Table C.2 Exploratory campaign results for $Rz_\perp$ and $Rz_\parallel$.

Treat. N.	LED ($J\,mm^{-1}$)	h_d (mm)	S_d (mm)	V_{Ar} ($L\,min^{-1}$)	$Rz_\perp$ (µm)	$Rz_\parallel$ (µm)
					15.7	14.2
1	21	1	8	2	18.7	12.6
					16.9	13.4
					17.2	15.2
2	21	1	8	10	19.0	15.3
					17.1	13.9

Table C.2 – Continued from previous page.

Treat. N.	LED ($J\,mm^{-1}$)	h_d (mm)	S_d (mm)	V_{Ar} ($L\,min^{-1}$)	$Rz_{\perp}$ (µm)	$Rz_{\parallel}$ (µm)
					18.2	12.1
3	21	1	28	2	17.8	11.7
					17.6	12.1
					18.4	11.6
4	21	1	28	10	18.6	12.6
					18.2	12.8
					52.8	15.5
5	21	2	8	2	56.7	17.4
					50.3	13.3
					51.0	17.1
6	21	2	8	10	47.0	15.3
					47.4	14.9
					61.5	20.6
7	21	2	28	2	61.9	19.1
					56.4	21.1
					69.7	17.3
8	21	2	28	10	72.7	18.1
					71.4	17.3
					13.2	10.6
9	70	1	8	2	13.1	8.8
					11.7	9.5
					13.5	9.1
10	70	1	8	10	12.5	8.3
					14.2	11.5
					23.8	14.6
11	70	1	28	2	23.5	12.7
					21.3	11.8
					24.0	15.0
12	70	1	28	10	22.0	14.1

Table C.2 – Continued from previous page.

Treat. N.	LED ($J\,mm^{-1}$)	h_d (mm)	S_d (mm)	V_{Ar} ($L\,min^{-1}$)	$Rz_\perp$ (µm)	$Rz_\parallel$ (µm)
					21.8	14.4
					34.1	11.6
13	70	2	8	2	31.5	13.7
					30.0	12.6
					40.8	11.1
14	70	2	8	10	25.6	11.3
					32.2	10.1
					26.2	15.9
15	70	2	28	2	23.7	15.9
					25.3	14.1
					22.4	12.5
16	70	2	28	10	25.5	14.1
					27.3	11.9
					18.1	13.9
					20.8	14.0
17	45.5	1.5	18	6	15.1	13.3
					14.4	10.8
					14.2	11.8

Table C.3 Exploratory campaign results for $Rsk_\perp$ and $Rsk_\parallel$.

Treat. N.	LED ($J\,mm^{-1}$)	h_d (mm)	S_d (mm)	V_{Ar} ($L\,min^{-1}$)	$Rsk_\perp$ (µm)	$Rsk_\parallel$ (µm)
					-0.04	0.15
1	21	1	8	2	0.01	-0.04
					0.07	-0.19
					0.16	0.02
2	21	1	8	10	-0.17	-0.31
					0.10	-0.03

Table C.3 – Continued from previous page.

Treat. N.	LED ($J\,mm^{-1}$)	h_d (mm)	S_d (mm)	V_{Ar} ($L\,min^{-1}$)	$Rsk_{\perp}$ (µm)	$Rsk_{\parallel}$ (µm)
					0.11	0.31
3	21	1	28	2	-0.07	-0.22
					0.24	-0.04
					0.00	-0.31
4	21	1	28	10	0.11	0.35
					-0.15	0.67
					0.08	0.21
5	21	2	8	2	0.05	-0.13
					0.01	-0.02
					0.23	-0.12
6	21	2	8	10	-0.18	-0.26
					0.62	-0.19
					0.01	0.28
7	21	2	28	2	0.58	0.03
					0.23	-0.19
					0.17	0.13
8	21	2	28	10	0.19	0.17
					0.11	0.09
					-0.06	-0.07
9	70	1	8	2	-0.11	-0.08
					-0.10	-0.14
					0.07	-0.05
10	70	1	8	10	0.01	-0.28
					-0.02	-0.18
					0.10	-0.09
11	70	1	28	2	-0.08	0.02
					0.08	-0.05
					-0.07	0.16
12	70	1	28	10	0.20	-0.10

Table C.3 – Continued from previous page.

Treat. N.	LED ($J\,mm^{-1}$)	h_d (mm)	S_d (mm)	V_{Ar} ($L\,min^{-1}$)	$Rsk_{\perp}$ (µm)	$Rsk_{\parallel}$ (µm)
					0.04	0.24
					-0.12	0.37
13	70	2	8	2	-0.04	0.03
					-0.11	0.55
					0.11	-0.30
14	70	2	8	10	0.01	-0.16
					-0.02	-0.05
					0.26	-0.09
15	70	2	28	2	-0.23	0.02
					-0.11	-0.09
					-0.12	-0.11
16	70	2	28	10	-0.34	0.01
					-0.02	0.02
					0.02	0.04
					0.08	-0.12
17	45.5	1.5	18	6	-0.03	-0.07
					0.12	0.07
					0.00	-0.16

Table C.4 Exploratory campaign results for $Rku_{\perp}$ and $Rku_{\parallel}$.

Treat. N.	LED ($J\,mm^{-1}$)	h_d (mm)	S_d (mm)	V_{Ar} ($L\,min^{-1}$)	$Rku_{\perp}$ (µm)	$Rku_{\parallel}$ (µm)
					2.4	2.4
1	21	1	8	2	1.9	2.1
					2.3	2.1
					2.3	2.2
2	21	1	8	10	2.3	2.1
					2.1	2.3

Table C.4 – Continued from previous page.

Treat. N.	LED ($J\,mm^{-1}$)	h_d (mm)	S_d (mm)	V_{Ar} ($L\,min^{-1}$)	$Rku_{\perp}$ (µm)	$Rku_{\parallel}$ (µm)
					3.1	3.4
3	21	1	28	2	2.5	2.1
					3.3	3.4
					3.2	2.3
4	21	1	28	10	3.1	2.5
					2.9	3.3
					3.3	2.4
5	21	2	8	2	3.1	2.2
					2.6	2.3
					4.9	2.9
6	21	2	8	10	5.3	2.9
					3.7	2.0
					5.0	2.2
7	21	2	28	2	5.9	1.8
					4.5	2.5
					3.7	2.4
8	21	2	28	10	4.7	2.5
					5.8	2.1
					2.5	2.3
9	70	1	8	2	2.6	1.9
					2.4	2.4
					2.7	2.7
10	70	1	8	10	2.4	1.9
					3.0	2.1
					2.4	2.6
11	70	1	28	2	2.5	2.8
					2.1	2.8
					2.3	2.4
12	70	1	28	10	2.4	3.3

Table C.4 – Continued from previous page.

Treat. N.	LED ($J\,mm^{-1}$)	h_d (mm)	S_d (mm)	V_{Ar} ($L\,min^{-1}$)	$Rku_{\perp}$ (µm)	$Rku_{\parallel}$ (µm)
					2.5	3.1
					5.8	3.1
13	70	2	8	2	4.1	2.0
					3.1	2.3
					4.8	2.3
14	70	2	8	10	5.5	2.8
					4.6	2.2
					2.2	2.1
15	70	2	28	2	2.7	2.7
					3.5	3.0
					3.4	2.5
16	70	2	28	10	2.9	2.7
					2.8	2.7
					9.5	4.0
					2.5	2.1
17	45.5	1.5	18	6	2.9	2.1
					4.2	2.2
					3.2	3.1

Table C.5 Exploratory campaign results for $Wa_{\perp}$ and $Wa_{\parallel}$.

Treat. N.	LED ($J\,mm^{-1}$)	h_d (mm)	S_d (mm)	V_{Ar} ($L\,min^{-1}$)	$Wa_{\perp}$ (µm)	$Wa_{\parallel}$ (µm)
					9.3	9.9
1	21	1	8	2	10.2	9.4
					8.0	15.0
					9.6	12.7
2	21	1	8	10	11.0	10.9
					9.7	11.8
					7.6	7.1
3	21	1	28	2		

Table C.5 – Continued from previous page.

Treat. N.	LED ($J\,mm^{-1}$)	h_d (mm)	S_d (mm)	V_{Ar} ($L\,min^{-1}$)	$Wa_\perp$ (µm)	$Wa_\parallel$ (µm)
					9.3	9.0
					8.6	17.7
					10.1	10.6
4	21	1	28	10	7.0	11.4
					6.0	8.6
					9.7	9.4
5	21	2	8	2	10.7	9.1
					11.9	7.9
					12.6	8.8
6	21	2	8	10	10.0	10.6
					10.1	11.8
					8.2	10.3
7	21	2	28	2	11.1	11.3
					8.9	10.7
					10.1	11.2
8	21	2	28	10	9.8	13.2
					10.0	13.4
					8.0	15.6
9	70	1	8	2	8.4	15.0
					6.4	8.6
					12.7	12.1
10	70	1	8	10	7.9	8.9
					9.5	9.5
					6.3	9.7
11	70	1	28	2	8.0	12.5
					7.0	9.2
					6.3	11.2
12	70	1	28	10	6.5	7.4
					9.3	12.6

Table C.5 – Continued from previous page.

Treat. N.	LED ($J\,mm^{-1}$)	h_d (mm)	S_d (mm)	V_{Ar} ($L\,min^{-1}$)	$Wa_\perp$ (µm)	$Wa_\parallel$ (µm)
					7.4	10.9
13	70	2	8	2	12.1	9.5
					13.2	9.5
					9.0	8.6
14	70	2	8	10	23.9	7.6
					8.1	16.5
					10.5	8.4
15	70	2	28	2	8.8	11.3
					8.7	15.8
					9.2	7.8
16	70	2	28	10	9.8	10.7
					14.7	8.9
					13.0	8.1
					14.9	12.1
17	45.5	1.5	18	6	8.9	14.2
					6.9	7.6
					8.6	9.0

Table C.6 Exploratory campaign results for $Wz_\perp$ and $Wz_\parallel$.

Treat. N.	LED ($J\,mm^{-1}$)	h_d (mm)	S_d (mm)	V_{Ar} ($L\,min^{-1}$)	$Wz_\perp$ (µm)	$Wz_\parallel$ (µm)
					40.2	47.1
1	21	1	8	2	44.3	44.8
					33.6	74.0
					41.7	56.6
2	21	1	8	10	43.2	51.1
					39.6	53.7
					32.6	32.8
3	21	1	28	2	37.9	42.1

Table C.6 – Continued from previous page.

Treat. N.	LED ($J\,mm^{-1}$)	h_d (mm)	S_d (mm)	V_{Ar} ($L\,min^{-1}$)	$Wz_{\perp}$ (µm)	$Wz_{\parallel}$ (µm)
					41.1	78.2
					48.8	46.2
4	21	1	28	10	31.3	46.1
					26.7	41.2
					44.9	39.9
5	21	2	8	2	48.5	45.7
					53.4	35.3
					46.9	39.8
6	21	2	8	10	40.4	52.5
					47.7	55.7
					37.1	45.2
7	21	2	28	2	49.8	52.9
					44.2	47.9
					44.0	46.6
8	21	2	28	10	44.2	60.1
					42.5	60.2
					36.8	60.0
9	70	1	8	2	37.4	57.1
					27.7	39.7
					57.1	47.5
10	70	1	8	10	31.6	39.4
					39.6	41.2
					27.3	42.3
11	70	1	28	2	36.8	47.9.
					29.1	37.9
					33.0	46.8
12	70	1	28	10	28.1	31.1
					39.4	52.3
					32.6	52.5
13	70	2	8	2		

Table C.6 – Continued from previous page.

Treat. N.	LED ($J\,mm^{-1}$)	h_d (mm)	S_d (mm)	V_{Ar} ($L\,min^{-1}$)	$Wz_{\perp}$ (µm)	$Wz_{\parallel}$ (µm)
					55.7	44.1
					56.7	40.4
					44.8	38.2
14	70	2	8	10	101.1	37.8
					40.7	69.5
					45.7	37.9
15	70	2	28	2	34.0	50.9
					36.5	73.8
					37.9	34.5
16	70	2	28	10	45.5	42.1
					65.1	43.9
					51.5	34.9
					61.0	52.6
17	45.5	1.5	18	6	39.4	59.5
					29.9	32.8
					36.8	39.0

C.2 Steepest descent dataset

Table C.7 Steepest descent results for $Ra_{\perp}$ and $Ra_{\parallel}$.

Step. N.	LED ($J\,mm^{-1}$)	h_d (mm)	$Ra_{\perp}$ (µm)	$Ra_{\parallel}$ (µm)
			3.2	2.5
1	59	1.00	3.5	2.7
			2.9	2.7
			2.7	2.4
2	66	0.75	3.0	2.3
			2.9	2.2

Table C.7 – Continued from previous page.

Treat. N.	LED ($J\,mm^{-1}$)	h_d (mm)	$Ra_\perp$ (µm)	$Ra_\parallel$ (µm)
			2.7	2.2
3	73	0.5	2.3	2.0
			2.2	1.9
			2.3	2.1
4	80	0.25	2.2	2.1
			2.0	2.0

Table C.8 Steepest descent results for $Rz_\perp$ and $Rz_\parallel$.

Step. N.	LED ($J\,mm^{-1}$)	h_d (mm)	$Rz_\perp$ (µm)	$Rz_\parallel$ (µm)
			19.3	9.2
1	59	1.00	16.3	10.4
			13.2	10.7
			12.6	10.1
2	66	0.75	10.6	8.9
			11.2	8.4
			13.5	9.4
3	73	0.5	10.9	10.3
			9.2	9.6
			10.6	8.2
4	80	0.25	12.2	9.6
			12.0	7.7

Table C.9 Steepest descent results for $Rsk_\perp$ and $Rsk_\parallel$.

Step. N.	LED ($J\,mm^{-1}$)	h_d (mm)	$Rsk_\perp$ (µm)	$Rsk_\parallel$ (µm)
			-0.02	-0.05
1	59	1.00	-0.04	0.19

Table C.9 – Continued from previous page.

Treat. N.	LED ($J\,mm^{-1}$)	h_d (mm)	$Rsk_\perp$ (µm)	$Rsk_\parallel$ (µm)
			-0.05	-0.04
			-0.10	0.07
2	66	0.75	-0.03	-0.06
			-0.05	-0.03
			0.05	-0.08
3	73	0.5	-0.06	0.24
			-0.01	0.24
			0.06	0.05
4	80	0.25	-0.02	0.16
			-0.10	-0.13

Table C.10 Steepest descent results for $Rku_\perp$ and $Rku_\parallel$.

Step. N.	LED ($J\,mm^{-1}$)	h_d (mm)	$Rku_\perp$ (µm)	$Rku_\parallel$ (µm)
			2.4	2.25
1	59	1.00	2.4	2.20
			2.4	2.04
			2.7	2.77
2	66	0.75	2.6	2.60
			2.6	2.55
			2.5	2.32
3	73	0.5	2.3	2.16
			2.6	2.82
			2.4	2.79
4	80	0.25	2.5	2.53
			2.3	2.44

Table C.11 Steepest descent results for $Wa_{\perp}$ and $Wa_{\parallel}$.

Step. N.	LED ($J\,mm^{-1}$)	h_d (mm)	$Wa_{\perp}$ (µm)	$Wa_{\parallel}$ (µm)
1	59	1.00	9.4	11.2
			7.9	11.3
			8.1	12.5
2	66	0.75	10.9	12.0
			9.0	8.8
			12.0	8.7
3	73	0.5	9.8	10.4
			6.3	13.0
			9.4	12.5
4	80	0.25	8.1	8.8
			7.2	10.9
			9.5	7.6

Table C.12 Steepest descent results for $Wz_{\perp}$ and $Wz_{\parallel}$.

Step. N.	LED ($J\,mm^{-1}$)	h_d (mm)	$Wz_{\perp}$ (µm)	$Wz_{\parallel}$ (µm)
1	59	1.00	39.3	24.7
			35.8	24.7
			33.3	26.1
2	66	0.75	51.8	24.7
			39.6	18.9
			52.1	19.5
3	73	0.5	40.5	21.8
			27.0	27.3
			39.7	23.3
4	80	0.25	36.6	20.5
			32.3	20.1
			40.1	31.2

C.3 Optimization campaign dataset

Table C.13 Optimization campaign results for $Ra_{\perp}$ and $Ra_{\parallel}$.

Treat. N.	LED ($J\,mm^{-1}$)	h_d (mm)	$Ra_{\perp}$ (µm)	$Ra_{\parallel}$ (µm)
			2.7	2.6
1	76	0.1	2.3	2.5
			2.5	2.5
			1.9	1.8
2	76	0.25	2.2	2.0
			2.1	1.7
			2.5	2.1
3	76	0.4	2.2	1.9
			2.3	1.9
			2.4	2.6
4	81	0.1	2.3	2.7
			2.7	3.1
			2.5	2.0
5	81	0.25	2.2	2.0
			2.0	2.0
			2.4	2.1
6	81	0.40	2.3	2.0
			2.0	2.0
			2.8	2.8
7	86	0.10	2.7	3.0
			2.7	2.6
			2.2	1.8
8	86	0.25	1.9	1.9
			2.0	1.9
			2.4	2.2
9	86	0.40	1.9	2.0
			2.2	1.9

Table C.14 Optimization campaign results for $Rz_{\perp}$ and $Rz_{\parallel}$.

Treat. N.	LED ($J\,mm^{-1}$)	h_d (mm)	$Rz_{\perp}$ (µm)	$Rz_{\parallel}$ (µm)
1	76	0.1	13.0	13.5
			12.0	12.7
			12.2	13.1
2	76	0.25	9.0	7.8
			11.0	9.1
			10.2	8.0
3	76	0.4	12.0	9.4
			11.2	9.1
			11.4	9.0
4	81	0.1	15.7	13.4
			11.3	13.7
			12.7	15.5
5	81	0.25	12.5	10.0
			10.2	9.1
			9.7	9.3
6	81	0.40	11.7	9.2
			11.3	8.8
			8.9	8.8
7	86	0.10	13.0	12.3
			12.8	11.3
			20.0	13.2
8	86	0.25	10.9	8.4
			9.7	8.9
			9.5	9.1
9	86	0.40	11.3	9.9
			9.7	9.2
			10.9	9.9

Table C.15 Optimization campaign results for $Rsk_{\perp}$ and $Rsk_{\parallel}$.

Treat. N.	LED ($J\,mm^{-1}$)	h_d (mm)	$Rsk_{\perp}$ (µm)	$Rsk_{\parallel}$ (µm)
			-0.06	-0.12
1	76	0.1	-0.34	-0.16
			0.17	-0.06
			-0.09	0.08
2	76	0.25	-0.07	0.11
			0.04	0.02
			-0.19	-0.03
3	76	0.4	-0.06	0.04
			0.15	-0.07
			0.07	-0.09
4	81	0.1	0.12	-0.05
			-0.08	0.00
			0.10	0.07
5	81	0.25	0.20	-0.09
			0.01	-0.05
			0.26	0.87
6	81	0.40	-0.19	0.00
			0.24	-0.03
			-0.02	-0.06
7	86	0.10	-0.18	-0.12
			0.10	-0.03
			-0.19	0.02
8	86	0.25	-0.02	-0.05
			0.04	0.00
			0.12	-0.10
9	86	0.40	-0.02	-0.04
			0.08	-0.01

Table C.16 Optimization campaign results for $Rku_{\perp}$ and $Rku_{\parallel}$.

Treat. N.	LED ($J\,mm^{-1}$)	h_d (mm)	$Rku_{\perp}$ (µm)	$Rku_{\parallel}$ (µm)
			3.2	2.7
1	76	0.1	2.4	2.6
			2.7	2.7
			2.7	2.5
2	76	0.25	2.4	2.4
			2.5	2.6
			2.3	2.5
3	76	0.4	2.8	2.7
			2.7	2.5
			2.6	2.6
4	81	0.1	2.4	2.6
			2.7	2.7
			2.5	2.7
5	81	0.25	2.4	2.5
			2.5	2.5
			2.9	1.7
6	81	0.40	2.9	2.3
			2.5	2.3
			2.3	2.5
7	86	0.10	2.8	2.5
			3.0	2.7
			2.3	2.4
8	86	0.25	2.5	2.4
			2.6	2.6
			2.1	2.6
9	86	0.40	2.4	2.7
			2.8	2.5

Table C.17 Optimization campaign results for $Wa_{\perp}$ and $Wa_{\parallel}$.

Treat. N.	LED ($J\,mm^{-1}$)	h_d (mm)	$Wa_{\perp}$ (µm)	$Wa_{\parallel}$ (µm)
			10.0	11.6
1	76	0.1	7.2	8.5
			9.0	9.2
			7.5	9.9
2	76	0.25	7.4	10.6
			9.1	4.5
			11.1	7.4
3	76	0.4	11.1	9.6
			7.6	9.5
			8.5	7.5
4	81	0.1	10.2	8.5
			8.9	7.2
			11.2	8.3
5	81	0.25	7.6	7.2
			6.9	8.3
			10.1	11.0
6	81	0.40	10.1	8.6
			11.0	11.8
			9.3	13.7
7	86	0.10	8.6	5.7
			8.6	6.8
			7.4	12.4
8	86	0.25	5.8	11.2
			7.9	6.8
			9.0	6.5
9	86	0.40	8.2	9.0
			10.1	9.2

Table C.18 Optimization campaign results for $Wz_{\perp}$ and $Wz_{\parallel}$.

Treat. N.	LED ($J\,mm^{-1}$)	h_d (mm)	$Wz_{\perp}$ (µm)	$Wz_{\parallel}$ (µm)
			46.6	47.3
1	76	0.1	27.7	28.8
			36.6	36.6
			31.7	35.4
2	76	0.25	35.7	45.9
			40.0	20.1
			44.3	34.9
3	76	0.4	44.2	44.8
			34.9	36.8
			39.1	31.0
4	81	0.1	48.3	37.1
			40.0	34.9
			45.0	32.5
5	81	0.25	33.8	32.6
			31.4	36.1
			45.8	48.0
6	81	0.40	46.4	35.3
			48.6	46.9
			41.0	53.4
7	86	0.10	39.3	26.3
			39.8	29.3
			34.6	47.0
8	86	0.25	32.9	44.1
			33.4	29.6
			35.1	28.9
9	86	0.40	30.8	37.0
			42.1	38.6